

Spectral Analysis of multichromatic thermographic measurement principles

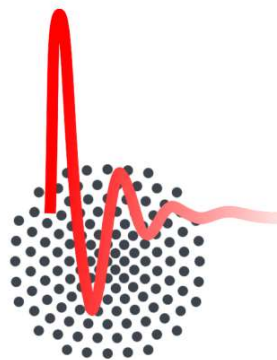
Master Thesis written by:

Luca Ressel



**Deutsches Zentrum
für Luft- und Raumfahrt**
German Aerospace Center

Institute of Solar Research



1.Physikalisches Institut

Universität Stuttgart

Main Reporter:

Prof. Martin Dressel

Co-reporter:

Prof. Siegfried Schmauder

Supervisor:

Simon Caron

27 April 2021

Table of Contents

List of Figures	3
List of Tables	6
Nomenclature Table	7
Abbreviation Table	7
1. Introduction	9
1.1 Word Energy Overview	9
1.2 Photovoltaics (PV)	11
1.3 Concentrated Solar Power (CSP)	12
1.4 TubeMon Project	16
2. State of the Art	17
2.1 Electromagnetic Spectrum	17
2.2 Radiometric Quantities	18
2.3 Geometrical Optics for Infrared Radiation	20
2.4 Historical Background	21
2.5 Planck's Law	22
2.6 Wien's displacement Law	23
2.7 Stefan Boltzmann's Law	24
2.8 Emissivity	25
2.9 Kirchhoff's Law of Radiation	26
2.10 Infrared Thermography	27
2.11 Infrared System	28
2.11 IR Methods	30
2.12 Radiometric Chain	32
3. Methodology	35
3.1 Acknowledgment of the Software used	35
3.2 Model Introduction	35
3.3 Database (Layer 0)	37
3.4 First Layer	49
3.5 Second Layer	50
3.6 Third Layer	59
3.7 Fourth Layer	59
4. Simulation Results	71
4.1 Simulations Target	71

4.2 Early Test Runs	71
4.3 Error Analysis	73
4.4 Filter Calibration	78
4.5 Optimizer Strategy	79
4.6 SWIR Analysis	79
4.7 MWIR Analysis	83
4.8 LWIR Analysis	87
5. Conclusion	91
References	92

List of Figures

Figure 1 - Electricity Generation by countries from 1985 to 2018 [1]	9
Figure 2 - Energy consumption by source from 1985 to 2019. It measures the total energy demand of a country. It covers consumption of the energy sector itself, losses during transformation (for example, from oil or gas into electricity) and distribution of energy, and the final consumption by end users. It excludes energy carriers used for non-energy purposes (such as petroleum not used not for combustion but for producing plastics). [1]	10
Figure 3 - 1st generation PV cell working mechanism [8].	11
Figure 4 - CSP Project around the world mapped [9].	12
Figure 5 - Average annual direct normal irradiation in Europe map from 2004 to 2010 . The common threshold for CSP is about 1800 kWh/m ² /year [10].	13
Figure 6 – Parabolic trough CSP power plants [11].	13
Figure 7 - Linear fresnel CSP power plant [11].	14
Figure 8 - Parabolic dish CSP power plant [11].	14
Figure 9 - Solar power tower CSP power plant [11].	15
Figure 10 - Electromagnetic Spectrum [16].	17
Figure 11 - Radiant power emitted from a given surface [15].	18
Figure 12 - Project area from an emitting surface [15].	19
Figure 13 - Illustration of the inverse square law [17].	19
Figure 14 - Law of reflection and refraction (Snell's law) [15].	20
Figure 15 - IR Spectrum generated from a collimated beam of electromagnetic radiation using a not absorbing prism [15].	20
Figure 16 - Planck blackbody function designed with MatLab® software by using as input the previous Planck's equation (Eq.8), it needs to be mentioned that a set of 10 different temperatures was chosen ranging from 400 K to 1300 K . a) Graph show as usual plot function to underline the various peaks. b) Graph shown with loglog function to highlights lower temperatures otherwise not visible.	22
Figure 17 - Wien's displacement law	23
Figure 18 - Stefan-Boltzmann law's considering a blackbody at 1300K.	24
Figure 19 - Emissivity comparison [15].	25
Figure 20 - Transition from a smooth surface to rough one and the change in reflectivity that that this implies [15].	27
Figure 21 - Dependence of the portion of reflected IR radiation on the angle of incidence in a transition from air to silicon [15].	27
Figure 22 - Schematic representation of a microbolometer [22].	28
Figure 23 - Fabrication technique for a membrane suspended microbolometer with highlight in the different in the process for either a planar or sandwich structure [23].	29
Figure 24 - IR detector materials possibilities [24].	30
Figure 25 - Spectral filer options [15].	31
Figure 26 - Illustration of the radiometric chain taken into analysis, for the purpose of this work.	32
Figure 27 - Filtered Signal Scheme and contribution of Detector and Camera [25].	34
Figure 28 - Function synoptical map	36
Figure 29 - Solar spectral irradiance database graphical visualization [28].	37
Figure 30 - Earth Atmosphere stratification diagram [31].	38
Figure 31 - Geometrical specification of the MODTRAN atmospheric sensor [29].	40
Figure 32 - Atmospheric Transmittance Dataset. a) it shows the MWIR and LWIR database taken from ModTran Online Software. b) it shows the SWIR database taken from code SMARTS files. Note: in order to highlight the correlation between the two graphs b) is basically displayed as a zoom from the a) graph but still it is based on a different data source.	41
Figure 33 - Mirror Reflectance dataset graph.	42
Figure 34 - Material data for two different samples: Pyromark 2500 and Haynes both cured at 750°C for 1000 hours.	44

Figure 35 - CQDIP working principles, in the upper part the colloidal nanoparticles are displayed as illustration while in the bottom part a schematic representation explains the quantum wells principles behind [42].	44
Figure 36 - HgCdTe photodetector geometry [43].	45
Figure 37 - Detector Database graph divided by range and source. a) SWIR dataset provided by SWIR Vision Systems. b) LWIR FLIR A655sc and MIWIR FLIR SC5500 dataset provided by FLIR System.	45
Figure 38 - WebPlot Digitizer template used to extract filter's transmittance vs wavelength. On the left side: image upload and axes selection (done manually). In the center: PDF image of the graph into analysis and point selection on the curve. On the right side: point adjustment and data extraction [45].	47
Figure 39 - Visual representation of the WebPlot Digitizer vs Gaussian model comparison for the 9480 NB filter. a) Overlap of the two filters curve obtained with the two methods. b) Offset calculation within the two curves shown in a).	48
Figure 40 - Example of a structure used in the code, the name of the structure is ref and the data contained as fields are represented by the variables in the previous list.	49
Figure 41- opts. Example for the loading atm data function	50
Figure 42 - Planck Law Live script.	51
Figure 43 - Load Solar Irradiance data Live script	52
Figure 44 - Load Atmospheric Data script	53
Figure 45 - Data pre-loading script	53
Figure 46 - Load Atmospheric Data Field script.	54
Figure 47 - Load Mirror Data script.	55
Figure 48 - Load Material Data script	56
Figure 49 - Load Filter Data script	57
Figure 50 - Load Detector Data script	58
Figure 51 - Reciprocal Planck Function script.	58
Figure 52 - Signal Analysis monochromatic script.	60
Figure 53 - Signal Analysis band script	62
Figure 54 - Model Analysis script	63
Figure 55 – Contour Map script.	65
Figure 56 – Calibration script	66
Figure 57 - Cost Function script.	68
Figure 58 - Optimizer script.	69
Figure 59 - Graphs obtained after a simulation runs done with the Signal Analysis monochromatic function on Scenario 8. a) Calculation of the three terms. b) total signal contribution in percentage (0-1) over the total signal	72
Figure 60 - Atmospheric transmittance with CO, CO ₂ , O ₃ and H ₂ O absorption bands highlighted. [48]	73
Figure 61 - Contour maps for comparison of the different performances between Pyromark 2500 in summer and winter using a band in the range of 8-14 μ m.	75
Figure 62 - Contour maps for comparison of the different performances between Pyromark 2500 and Haynes 230 in summer and winter using a narrow band in the range of 8-14 μ m.	76
Figure 63 - Contour maps for comparison of the different performances between Pyromark 2500 in summer and winter using a narrow band in the range of 8-14 μ m Scenario 7.	77
Figure 64 - Contour maps for comparison of the different performances between Pyromark 2500 in summer and winter using a narrow band in the range of 8-14 μ m.	77
Figure 65 - Filter Calibration results obtained with a constant HW=0.6.	78
Figure 66 - Filter Calibration results obtained with a constant CWL=10.	78
Figure 67 - $\epsilon\tau$ product filter comparison for SWIR range calculated for Pyromark cured at 750°C, for summer condition with a cx=200 and a Tbb=800°C.	80
Figure 68 - RMSE final value and $\epsilon\tau$ product comparison for two different scenarios outcomes with CWL expressed in μ m. a) scenario 7 combi 3; RMSE: 6,70e-06; Absolute temperature error: 3,08K; $\epsilon\tau$ error	

0,0141 and 0,0093. b) Scenario 8 combi 2 ; RMSE: 1,11e-08; Absolute temperature error: diverge; $\epsilon\tau$ error 0,5919 and 0,5646	82
Figure 69 - $\epsilon\tau$ product filter comparison for MWIR range calculated for Pyromark cured at 750°C , for summer condition with a cx=200 and Tbb=800°C.....	83
Figure 70 - RMSE final value and $\epsilon\tau$ product comparison for the same filter combination but with different models used. CWL is expressed in μm . The sub division of graphs is as follow: a) combi 11a results from the linear model. RMSE: 0,2025; Absolute temperature error: 35,12K; $\epsilon\tau$ 0,0893 0,0863 0,0828 and 0,0804. b) combi 11b tested using the quadratic model. RMSE: 0,2018; Absolute temperature error: 19,69K; $\epsilon\tau$ 0,0482 0,0467 0,0447 and 0,0435	85
Figure 71 - RMSE final value and $\epsilon\tau$ product comparison for the same filter combination tested for the same materials as Pyromark 2500 in the same condition of concentration factor. However the underline different is the season. CWL is expressed in μm . The sub division of graphs is as follow: a) combi 9 scenario 2; RMSE:0,018; Absolute temperature error 0,52K; $\epsilon\tau$ error: 0,0285 0,0285 and 0,0279 b) combi9 scenario 4; ;RMSE: 0,045; Absolute temperature error 4,64K; $\epsilon\tau$ error: 0,1060 0,1061 and 0,1079.....	87
Figure 72 - $\epsilon\tau$ product filter comparison for LWIR range. FC stands for filters chosen and within this box there are the four filters used for further evaluation, in order from the lower to higher CWL: 8645, 8900, 9127 and 9480.	88
Figure 73 - RMSE final value and $\epsilon\tau$ product comparison for two different filter combinations using two different methods. Both tested for the same materials as Pyromark 2500 in the same scenario1. CWL is expressed in μm . The division of graphs is as follow: a) combi5 ; RMSE: 1,1e-04; Absolute temperature error 11,58K; $\epsilon\tau$ error: 0,0166 and 0,0158. b) combi7 , RMSE: 0,893; Absolute temperature error 5,75K; $\epsilon\tau$ error: 0,0072 0,0095 and 0,0063.	90

List of Tables

Table 1 - Classification of various IR windows according to their wavelength.....	17
Table 2 - Chronology of Radiation Laws.....	21
Table 3 - Atmosphere gases composition [30].	38
Table 4 - MODTRAN® data entry for each season [29].	39
Table 5 - Specifications for the dataset regarding the atmosphere present in the field [33]......	41
Table 6 - Nominal Composition of Haynes 230, percentage expressed in weight for weight ratio [37].	42
Table 7 - Mixture Composition of Pyromark 2500, percentage expressed in weight for weight ratio [38].	43
Table 8 - Filter Database sorting by wavelength from SWIR to LWIR. CWL stands for central wavelength. HW stands for half width. τ_{peak} stands for tau peak can be a value between [0....1] and it's the highest value of tau that the filter reaches, it coincides with the peak of the function [44].	46
Table 9 - Flowchart design according to the ISO 5807 [46]......	51
Table 10 - Cost function models	67
Table 11 - Test scenarios for early signal tests.....	71
Table 12 - Absolute temperature errors expressed in K results for the different scenarios in various wavelength range. The values were obtained by the error calculation feature intrinsic of the function (Fig.53).	73
Table 13 - Set up for error magnitude analysis for the bands listed in Table 12.....	74
Table 14 - Camera setups for the three different ranges	79
Table 15 - SWIR combi1 Optimizer Analysis result.	80
Table 16 - SWIR Combi2 Optimizer Analysis result.	81
Table 17 - SWIR Combi3 Optimizer Analysis result.....	81
Table 18 - Filter permutations for the MWIR range with model chosen accordingly.	83
Table 19 - MWIR filters combination screening. Scenario 1 neglecting term 3 (atmospheric emission Eq.19) was the choice of boundary condition for these test runs.....	84
Table 20 - MWIR Combi4 Optimizer Analysis result.	85
Table 21 - MWIR Combi9 Optimizer Analysis result.	86
Table 22 - MWIR Combi10 Optimizer Analysis result.	86
Table 23 - LWIR filters permutation and model chosen	88
Table 24 - LWIR filters combination screening. Scenario 1 neglecting term 3 (noise factor) was the choice of boundary condition for these test runs.	89
Table 25 - LWIR Combi5 Optimizer Analysis result.....	89
Table 26 - LWIR Combi7 Optimizer Analysis result.....	89
Table 27 - Final Overview	91

Nomenclature Table

<i>Symbol</i>	<i>Definition</i>	<i>Units</i>
α	Absorptivity	[-]
S	Camera signal	[W m ⁻³]
C_x	Concentration factor	[-]
R	Detector signal contribution	[-]
ε	Emissivity	[-]
M	Excitance	[W/m ²]
F_k	Filter signal contribution	[-]
c_1	First radiation constant	[W m ⁻²]
C	Heat capacity	[J/K]
E	Irradiance	[W/m ²]
ρ_{spec}	Mirror reflectance	[-]
E	Photon energy	[W]
h	Planck constant	[J·s]
L	Radiance	[W·sr ⁻¹ ·m ⁻²]
Φ	Radiant flux	[W]
I	Radiant intensity	[W/sr]
P	Radiant power	[W]
c_2	Second radiation constant	[m.K]
SI	Solar irradiance	[W m ⁻³]
E_λ	Spectral irradiance	[W m ⁻³]
c	Speed of light	[m/s]
G	Thermal conductance	[W·K ⁻¹]
τ	Transmission coefficient	[-]
λ	Wavelength	[μm]

Abbreviation Table

<i>Symbol</i>	<i>Meaning</i>
<i>CWL</i>	Central Wavelength
<i>FPA</i>	Focal Plane Array
<i>HW</i>	Half Width
<i>IR</i>	Infrared
<i>IRR</i>	Intensity of Radiation Ratio
<i>LWIR</i>	Long wavelength infrared
<i>MWIR</i>	Mid wavelength infrared
<i>RMSE</i>	Root Mean Square Error
<i>SWIR</i>	Short wavelength infrared

1. Introduction

Energy Scenario

1.1 Word Energy Overview

In the last decades, starting from the early 1990s, there has been a growth in the world's population electricity generation as shown in Fig.1. In particular, in order to satisfy their economic growth and energy needs, some countries belonging to the category of emerging economies had generated higher electricity production compared to the ones of the developed countries. For example this is the case for China, which went from 2500 TWh generated in 2005 to more than 7166 TWh in 2018 [1].

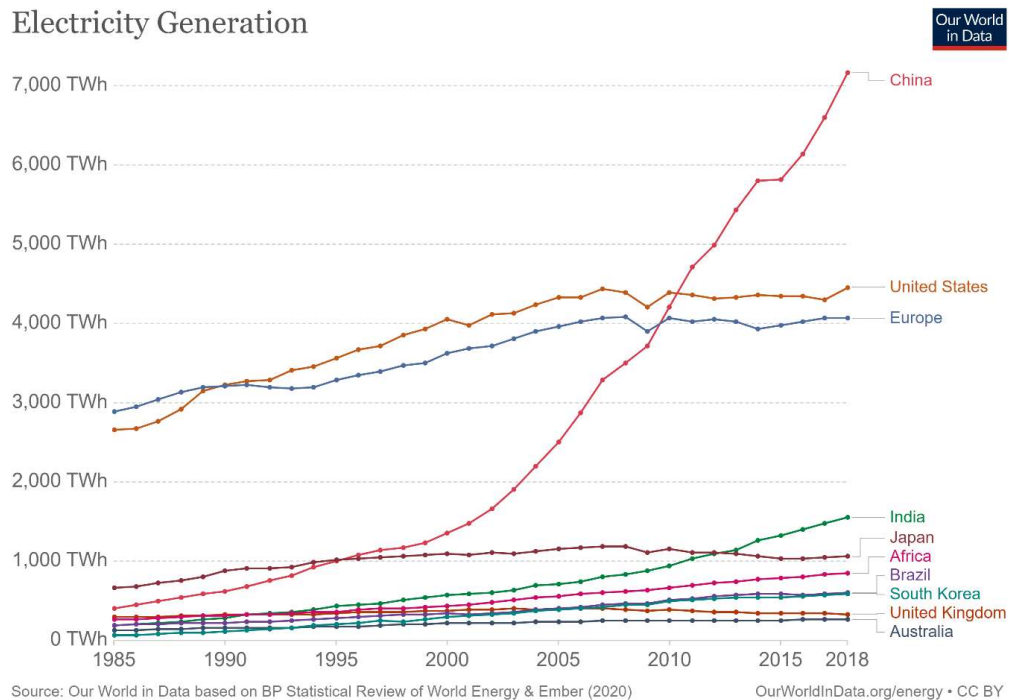


Figure 1 - Electricity Generation by countries from 1985 to 2018 [1]

At the actual rate, this development is leading to the depletion of fossil resources. If we take a look at Fig.2, which displays the distribution of primary energy consumption by energy source, a dominant fraction is still generated by fossil fuels such as oil and coal, on top in term of amount in 2019, respectively with 53619 TWh and 43849 TWh. This rush of energy caused by human activities has caused a serious environment impact by changing the Earth radiative balance, i.e. climate change. Over the last century, the burning of fossil fuels such as coal and oil has increased the concentration of atmospheric carbon dioxide CO_2 , methane CH_4 and nitrous oxide N_2O . Particularly relevant is the production of carbon dioxide which prevents infrared radiation from escaping into space and this leads to a further increase in the already existing greenhouse effect [2]. The industrial activities that our modern civilization depends upon have raised the atmospheric carbon dioxide levels from 280 ppm to 414 ppm in the last 150 years, there's a better than 95 percent probability that human produced greenhouse gases have caused much of the observed increase in Earth's temperatures over the past 50 years [3].

Primary energy consumption by source, World

Primary energy is shown based on the 'substitution' method which takes account of inefficiencies in energy production from fossil fuels.

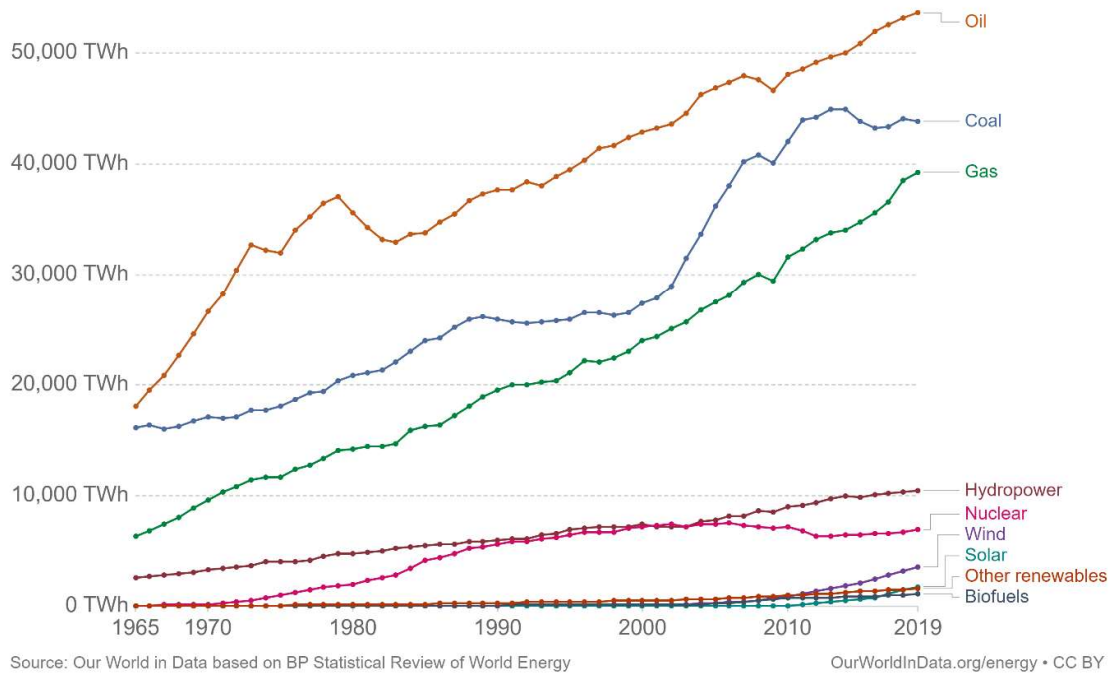


Figure 2 - Energy consumption by source from 1985 to 2019. It measures the total energy demand of a country. It covers consumption of the energy sector itself, losses during transformation (for example, from oil or gas into electricity) and distribution of energy, and the final consumption by end users. It excludes energy carriers used for non-energy purposes (such as petroleum not used for combustion but for producing plastics). [1]

This trend, which is leading to a climate crisis, was taken into consideration during the COP 21, from 30 November to 11 December 2015, where nations around the world set emission targets to limit the temperature increase to 1.5 °C above pre-industrial levels, officialised by the Paris Agreement. This is a landmark in the multilateral climate change process because it is a binding agreement that brings all signing nations into a common cause to undertake ambitious efforts to combat climate change and adapt to its effects [4]. This agreement sees 196 different countries come together to take decisive action and eventually in the last years this translated into several countries announcement of going carbon neutral in the next decades: in the case of China for example by 2060, but also Japan, South Korea, Germany and the Netherlands are following this commitment. Even though considering at the same time how the role of heavy industry in these countries domestic portfolio is affecting their emission levels, it is a big step forwards to a greener economy and a real opportunity for the renewable energy sector [5]. In this scenario, there are possibilities of investing in research related to new renewable energy sources, the ones listed below are among the most advanced techniques:

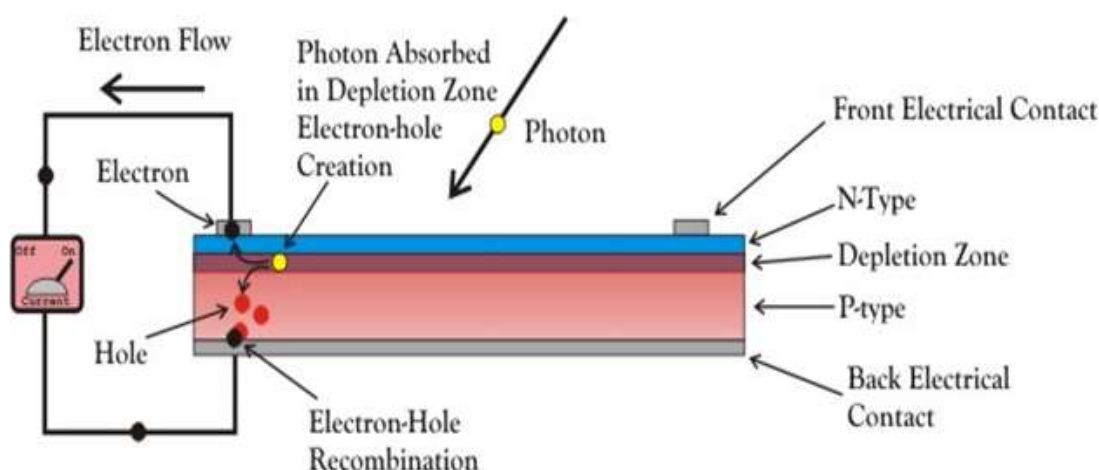
- Onshore and offshore wind
- Ocean and hydropower
- Biomass and biofuel
- Solar power

The latter, which represents the research field in which this thesis is based on, has an enormous potential, as reported from the MIT Department of Physics [6]. In fact, a total of 173,000 TW of solar energy reaches Earth continuously with power that is completely renewable. This vast amount of energy is in theory sufficient to meet all of humanity's energy needs, therefore the focus in the research filed is now shifted in the scientific and engineering challenges that the implementation of such technology will require on large scale operations.

Solar power plants are present in approximately 10% of the world's deserts surface. Considering overall efficiency at around 2 percent this translates in about 1.5 percent of the planet's total land area being able to generate about 15 TW of power. According to estimations of global energy demand this volume will match the projected growth in worldwide energy demand for the next half century [6]. The general intent of harvesting this energy can be divided in mainly two options, either it is possible to collect solar radiation through photovoltaics (PV) or through concentrated solar power technologies (CSP). The main differences and working principles will be explain in the next paragraphs.

1.2 Photovoltaics (PV)

PV technologies are based on the photovoltaic effect, discovered in 1839 by Alexandre-Edmond Becquerel, which is the generation of voltage or electricity in materials that are exposed to light. However, it is thanks to the p-n junction discovery by Russel Ohl in 1939 that modern photovoltaics cells gained momentum [7]. The p-n junction is the interface between two different semiconductor types produced by doping, one is referred as p-type and it is made by the introduction of electron rich ions, while the other one is the n-type and it is made by the introduction of electron deficient ions. The overall process of how PV works can be summarized in seven major steps, explained as such:



1. Absorption of light with suitable energy
2. Excitation of electrons
3. Formation of exciton (synonym for electron-hole pair)
4. Transport of exciton to the depletion zone
5. Possible charge recombination
6. Exciton split: separation of charges
7. Charges collection at the electrodes

Figure 3 - 1st generation PV cell working mechanism [8].

The doping is particularly effective for increasing the charge carrier density (photocurrent) and changing the chemical potential (photovoltage), two parameters that mostly affect the efficiency of the cell. Also, it is important to notice that the absorption need to match the band gap otherwise the energy will not create an exciton but only heat up the system. Ultimately the example taken into consideration for simplicity is the 1st generation solar cell, nowadays state of the art reaches the 3rd generation with polymer solar cells or multi-junction solar cells (perovskite solar cells).

1.3 Concentrated Solar Power (CSP)

CSP technologies are based on the concept of using mirrors to reflect and concentrate the energy from the sunlight to a receiver, i.e. the optical solar radiation will be converted into heat. The heat can then be used to create steam to drive a turbine to produce electrical power or be used in conventional industrial processes [9]. CSP plants compared to traditional PVs have the advantage to be able to integrate thermal energy storage systems to generate electricity during cloudy periods, for hours after sunset or before sunrise. CSP projects are present in 23 countries around the world as the 2020 data update show in Fig.4. From this graph, it is also noticeable the progress that this system will have in the years to come, this is the case of Chile (South America), where most of the MW are from plants that are under development and they will be operational in the near future. If we take a look at the number of the total 1210MW, 90% of it is under development, in the next decades considering the economic growth that this region of the world will have the potential will be translated into a more sustainable and cheaper access to energy.

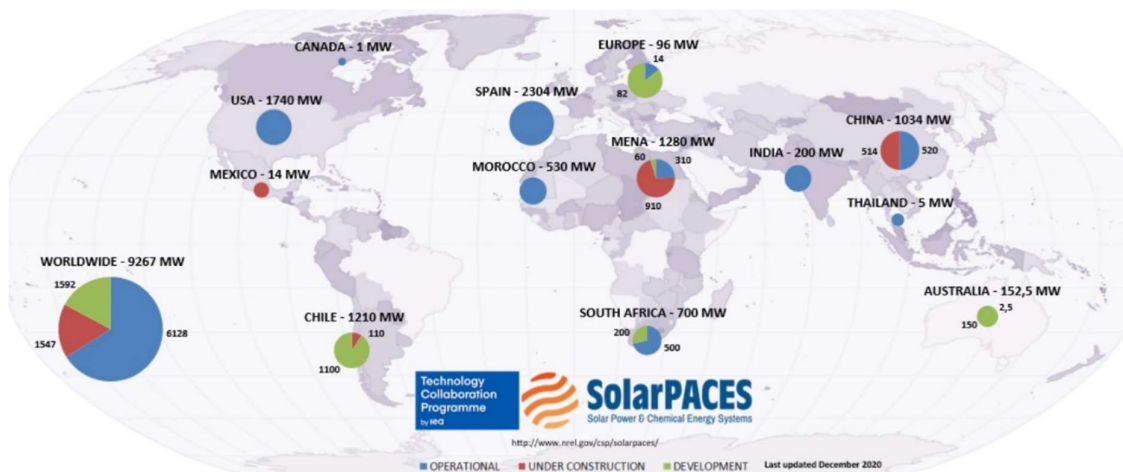
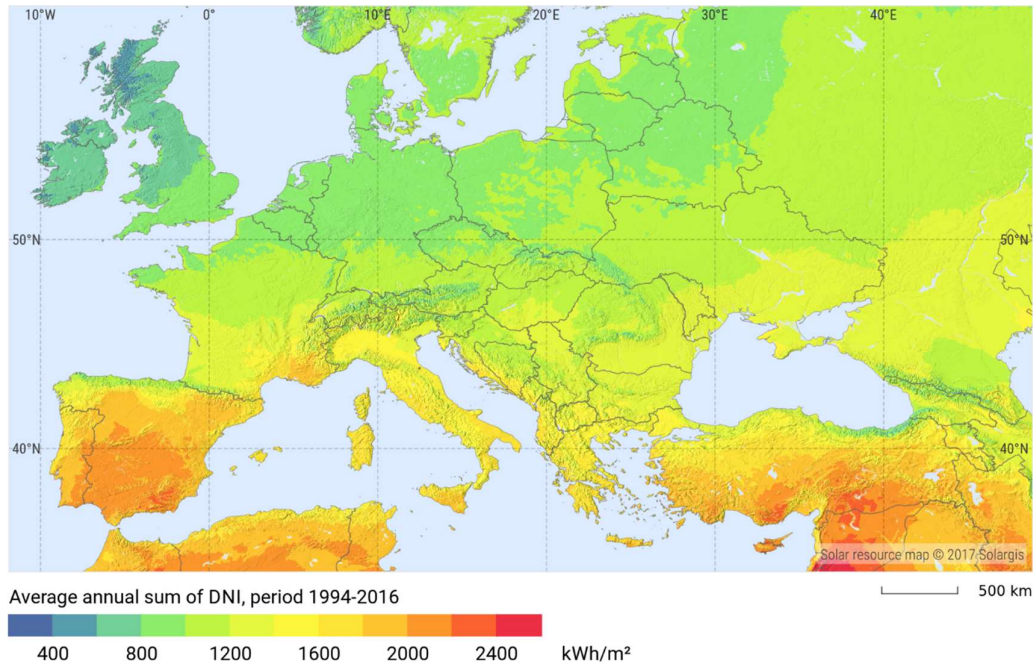


Figure 4 - CSP Project around the world mapped [9].

Considering that this is a technology that depends significantly on environmental conditions in order to harvest sufficient amount of energy and thrive economically, it is understandable why the projects have been built in regions where either there is a desert or the irradiation condition are favorable, typically above 1800 kWh/m²/year for direct normal irradiance. For example in the US the major projects are located in the Colorado or Nevada deserts, also the biggest CSP project to date in terms of MW generated is the Noor Solar Project based in Ouarzazate, Morocco in the Sahara desert, which produces 510MW. Regarding Europe, the same example is valid. In fact, as shown in Fig.5, the different of average annual direct normal irradiance (DNI) in kWh/m² presents in Spain leads to the country outstanding operational 2304MW capability compared to the 96MW of the rest of the continent (Fig. 4).

DIRECT NORMAL IRRADIATION EUROPE

SOLARGIS



This map is licensed by Solargis under the Creative Commons Attribution license (CC BY-SA 4.0). You are encouraged to use content of the map to benefit yourself and others in creative ways. For more information, please visit <http://solargis.com/download>.

Figure 5 - Average annual direct normal irradiation in Europe map from 2004 to 2010 . The common threshold for CSP is about 1800 kWh/m²/year [10].

There are mainly four types of CSP technologies, divided into two subcategories: linear focus and point focus, with different variations and geometries. They are all listed as follow [9].

- Parabolic Trough Systems

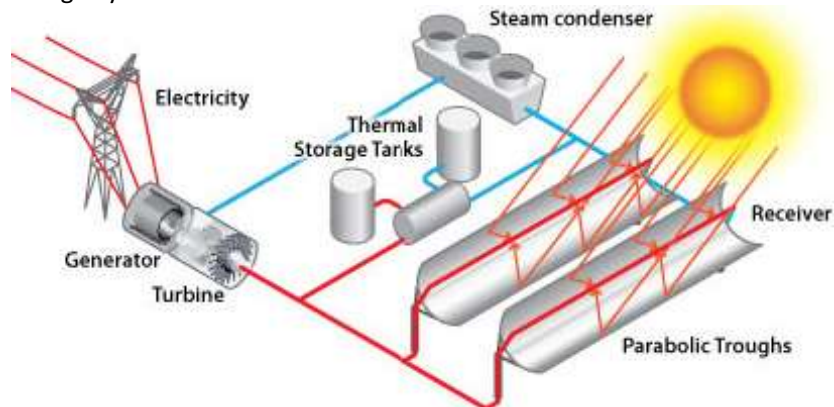


Figure 6 – Parabolic trough CSP power plants [11].

The main geometry of a parabolic trough CSP system (Fig.6) is characterized by a heat absorber tube, which is functioning as the receiver in this case, located about at the focus of the parabola above the parabolically curved mirror. The energy from the sunlight is focused by the mirrors on the receiver pipe, within the pipe a fluid is flowing, which is usually thermal oil. Its temperature thanks to the heat transfer mechanism raises from 293°C to 393°C. The heat produced is then used in the thermal power block to generate electricity in a conventional steam generator. A power plant field is usually designed with multiple parabolic trough-shaped

mirrors in parallel rows aligned to enable these single axis mirrors to track the sun from east to west during the day to ensure that direct normal irradiation is continuously focused on the receiver pipes.

- Linear Fresnel Systems

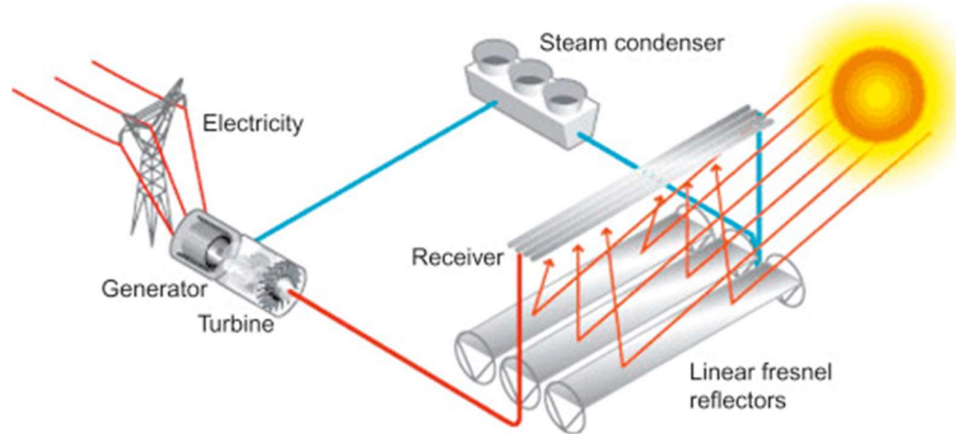


Figure 7 - Linear fresnel CSP power plant [11].

The linear Fresnel design is shown in Fig.7 , which is indeed similar to the geometry of a parabolic trough CSP system, with a different that in this variations the mirrors are flat and located on the ground while the pipe, into which they reflect the sunlight, is located above them. As the parabolic trough a power plant it is made by many mirrors aligned one next to the other, generally they have a north south orientation to maximize the sun energy throughout the year. In this configuration, mirrors are tracking all together in group while the receiver is fix.

- Parabolic Dish System

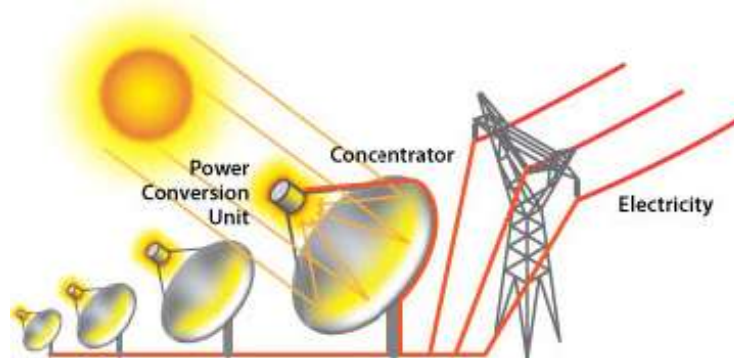


Figure 8 - Parabolic dish CSP power plant [11].

The parabolic dish design is characterized by a collector with a parabolic shape that reflects the sunlight on a receiver mounted at the focal plane (Fig.8). This receiver is different compared to the ones seen before because a Stirling heat engine is installed directly on it to harvest heat on situ, for this reason dish can reach extremely high temperatures (1500°C) and holds promise for use in solar reactors for making solar fuels, which require this high temperature levels, typically above 1000 °C. These concentrators are usually mounted on a structure with a two-axis azimuth-elevation tracking system to track the sun trajectory.

- Solar Power Tower

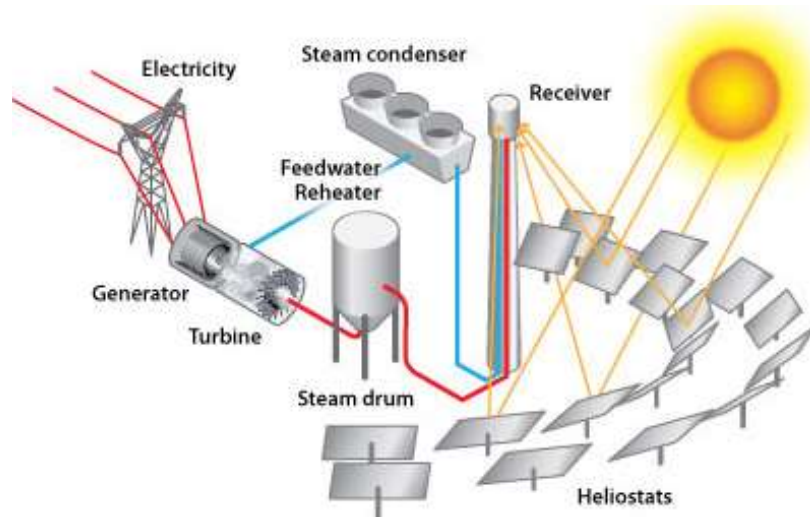


Figure 9 - Solar power tower CSP power plant [11].

As the parabolic dish, the solar power tower or central receiver system (CRS) belongs to the focal point category, but with few differences in term of design. For example, it utilizes two-axis tracking mirrors, called heliostats, to focus sunlight onto a receiver at the top of a tower (Fig.9). Inside the receiver, there is a fluid for the heat transfer process, the temperature in this case can reach up to 600°C for molten salts, while for particles receiver it can goes up to 1000°C. The generated heat is then used in a conventional turbine generator design to produce electricity. The earliest power towers project utilized steam as the heat transfer fluid, but nowadays state of the art power plants utilize molten salt as a process fluid. The main advantage lays on their superior heat transfer and energy storage capabilities. In the last years, researchers started to investigate various possibilities for new heat transfer or energy storage materials, this in case of success would translate into a strong potential by obtaining higher temperature with resulting efficiency gains that will lead to an overall lower levelized electricity cost to operate this power plants.

1.4 TubeMon Project

The TubeMon project, in which this work is embedded, is based on this later technology scenario, indeed its objective is to improve the control of a solar tower power plant, from which it takes the name as Tube Monitoring. This translates into the development of an innovative infrared (IR) camera to monitor both the temperature and emissivity of an absorber tube. This project includes three partner institutions, i.e. the DLR Institute of Solar Research [12], CSP Services [13] and BrightSource Industries [14]. The project has been divided into four work packages, summarized as follows:

- WP1: Flux density and absorptance measurements
- WP2: Temperature and emissivity measurements
- WP3: Demonstration at commercial plant
- WP4: Optimized control based on measurements

DLR in this case carries on the study of the Solar Flux at its research center in Jülich, while it proceeds on with the understanding of the technical aspects of the IR thermographic system in its facility in Almeria, Spain, such as filter choice, components architecture, model, optimization and calibration. This thesis is linked to the work package 2 (WP2) and focuses on the feasibility of multispectral thermography, applied to CSP. Based as a theoretical starter point for further progression in this field and mostly development on a MatLab simulation tool, this thesis sets specific targets within this wider project such as the understanding of which spectral band is relevant for this kind of measurements (SWIR, MWIR or LWIR), also how many filters should be required (2,3 or more) and ultimately the fine tuning of the method such as the selection of optical bandpass filters. In the next chapters, these points will be evaluated and analyzed further.

The main structure of this work is highlighted by the following scheme:

- Chapter 2: State of the Art
A basic understanding about the physics behind the IR measurement technique
- Chapter 3: Methodology / Modelling approach
Focused mostly on the building up process and the analysis model used in this work
- Chapter 4: Simulation Results
Based on the output obtained by the various optimization runs
- Chapter 5: Conclusion and Outlook
What's next and what we extract from this work

2. State of the Art

Infrared physics principles

2.1 Electromagnetic Spectrum

According to fundamental physical principles, every object at any given temperature above 0 K emits electromagnetic radiation, in the form of discrete photons (or quanta) traveling at the speed of light, which energy can be expressed in Eq.1 with λ referring to the wavelength.

$$E = hc/\lambda \quad \text{Eq.1}$$

The electromagnetic spectrum spreads from gamma rays to microwaves, as shown in Fig.10. Thermographic IR measurements are based on a particular spectral window that lays between visible light and microwave radiation. Infrared radiation (IR) can be split in three wavelength subranges, i.e. Short (SW), Mid (MW) and Long (LW) wavelengths as displayed in Table 1, even though further sub-windows are identified in astronomy [15].

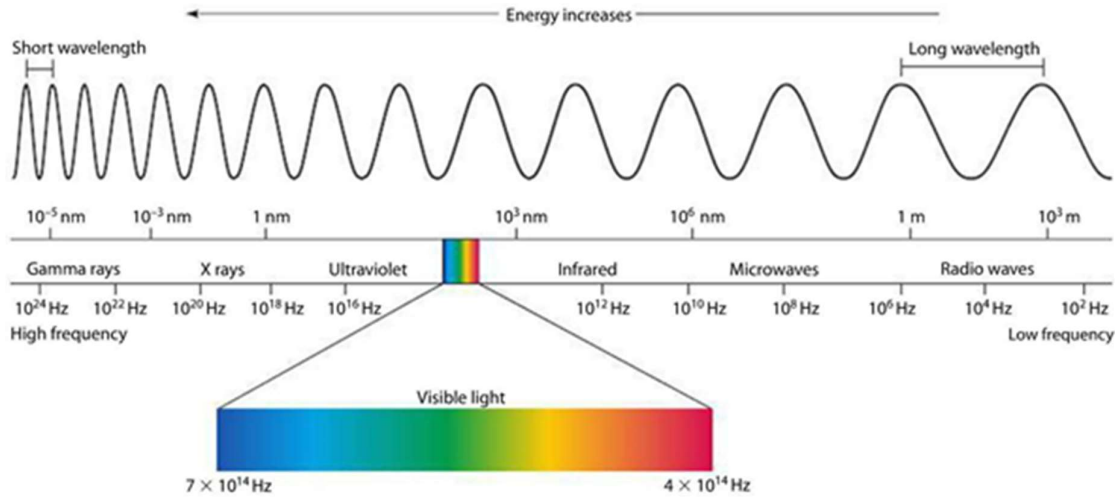


Figure 10 - Electromagnetic Spectrum [16].

Table 1 - Classification of various IR windows according to their wavelength

IR camera wavelength ranges	Wavelength [μm]
Short Wavelength (SWIR)	0.9 to 2
Medium Wavelength (MWIR)	2 to 5
Long Wavelength (LWIR)	8 to 14

In IR imaging, usually the three bands mentioned above are selected according to the detector choice, the optics, the materials into analysis and the environmental conditions such as atmospheric transmittance for example. In order to obtain a proper IR measurement result, the targeted object has to emit in one or more of the specific ranges described above, which will be detected by the camera. The function describing the maximum radiation that a body can emit is temperature dependent, this is the reason why emitted radiation is defined as thermal radiation. A perfect emitter in this sense is a blackbody, the latter can be defined by the following characteristics:

- A blackbody absorbs and emits all incident radiation, from any direction of space
- Spectral absorptivity or emissivity are not wavelength dependent
- At a given temperature, no others body can emit more radiation than a blackbody

2.2 Radiometric Quantities

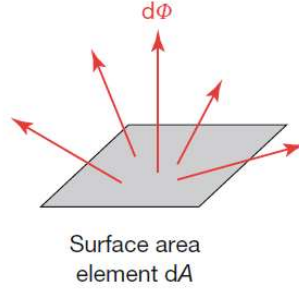


Figure 11 - Radiant power emitted from a given surface [15].

In order to understand under which conditions the radiation is travelling from the object where it has been generated through the environment, we can take a closer look at Fig.11, where an element dA of the radiating surface of an object is displayed. The total amount of energy flux $d\Phi$ [W] from this surface element dA into the hemisphere is called radiant power or energy. It can be measured only when all the radiation from the hemisphere is completely collected by the detector. In other terms, we can define the excitance M [W/m²] as the radiant power related to the emitting surface area, as defined in Eq.2:

$$M = \frac{d\Phi}{dA} \quad \text{Eq.2}$$

M is defined by the total radiant power within the hemisphere, divided by the surface area containing in this case all the contributions for the different wavelengths. On the other hand, one can consider the total radiant power from a hemisphere to a given surface dA and this definition will lead to the irradiance E [W/m²], defined in Eq.3:

$$E = \frac{d\Phi}{dA} \quad \text{Eq.3}$$

Even though the equations may look the same, one needs to consider that these are two different cases. In fact one corresponds to the energy flux emitted and the other to the energy flux received by a particular surface area dA . For the sake of clarity, the wavelength dependence was omitted at this stage, however real measurements are wavelength dependent.

In the further paragraphs Φ , M and E will be referred to as spectral radiant power, spectral excitance and spectral irradiance. So far, all the radiant power generated from the surface and emitted in all directions was considered, this leads to the fact that previous equations were not capable of explaining the flux behaviour according to the direction taken into consideration. The radiant intensity I [W/sr] is the radiant power that is emitted from a point source of a radiating object into a solid angle element $d\Omega$ characterized by (δ, φ) , it is explained in Eq.4.

$$I = \frac{d\Phi}{d\Omega} \quad \text{Eq.4}$$

Radiant intensity is related to the most often used quantity in radiometry, the radiance L and it is defined as the amount of radiant power per unit of projected source area and per unit solid angle, as expressed in Eq.5a:

$$L = \frac{d^2\Phi}{\cos(\delta) d\Omega dA} \quad \text{Eq.5a}$$

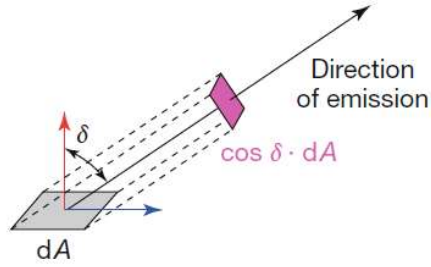
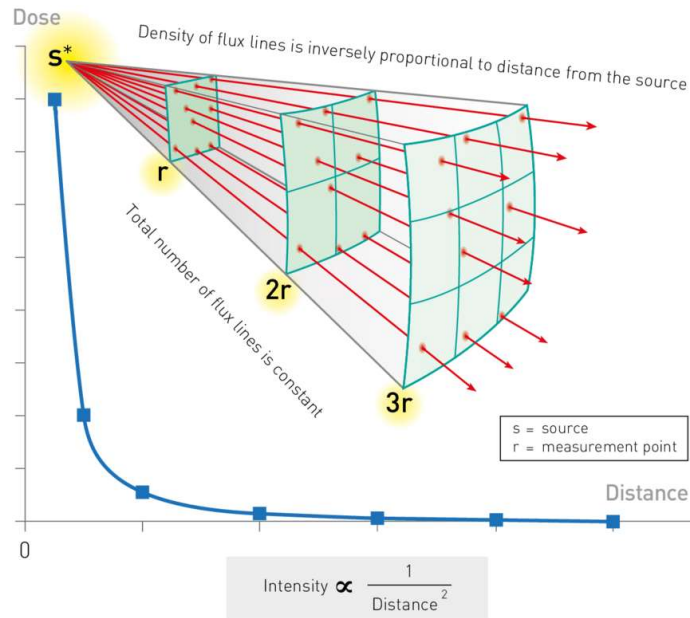


Figure 12 - Project area from an emitting surface [15].

The use of the geometrical factor $\cos(\delta)$ can be explained by referring to Fig.12. In fact, any emitting surface area dA is observed to be smaller for any direction that is not perpendicular to the surface, only the projection $\cos(\delta) dA$ can be seen from the emitting surface. It is important to underline the main difference between these last two quantities (I and L), in fact while the intensity of radiation decreases as the square of distance from the source, radiance is invariant with distance. This can be explained by the inverse square law, in Fig.13 is illustrated a simplified example. Taking into consideration the intensity of radiation, while the area increasing with the distance the dose of radiation does not, so as the distance will increase the same amount of radiation will be spread on an increasingly wider area and thus will reduce its intensity [15].

$$d^2\Phi = \frac{L \cos(\delta) dA_1 dA'_2}{r'^2} \quad \text{Eq.5b}$$

The equation written above (Eq.5b), considering to express radiometric quantities in terms of constant angle such as $d\Omega = dA'_2/r'^2$, shows that the quadratically decreasing radiance L/r^2 in equation cancels out with the quadratically increasing area dA_1 resulting in the same energy flux $d^2\Phi$.



* This is a simplified model assuming a point-source of radiation.
NORM contamination is usually found across a large area.

Figure 13 - Illustration of the inverse square law [17].

2.3 Geometrical Optics for Infrared Radiation

In order to understand the properties of IR propagation, it can be easily described in terms of geometrical optics, because this description is valid if the wavelength of the light is much smaller than the size of the objects or structures on which the light is incident. Taking a closer look at Fig.14 it is shown how at the boundary between the two materials part of the incident radiation is reflected and part of it is transmitted as refracted IR radiation.

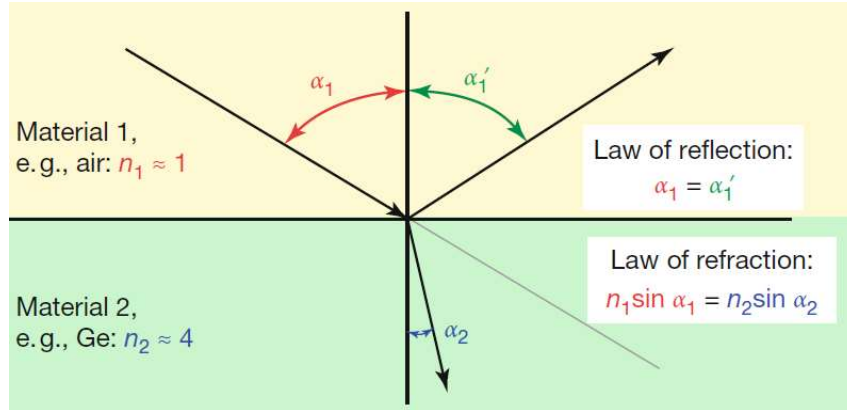


Figure 14 - Law of reflection and refraction (Snell's law) [15].

$$\alpha'_1 = \alpha_1 \quad \text{Eq.6}$$

Eq.6 is called the law of reflection and it features the variable α_1 , which is the angle of incidence and it can be defined as the orientation between the incident radiation and surface normal of the boundary between two materials, while α'_1 is the corresponding angle between the reflected ray and the surface normal.

$$n_1 \sin \alpha_1 = n_2 \sin \alpha_2 \quad \text{Eq.7}$$

Eq.7 is called law of refraction or Snell's law and it is considered the basis for lens optics. Typical optical materials show a normal dispersion, in other words it means that the index of refraction decreases with increasing wavelength. This phenomenon can be explained if we take into consideration the radiation incident on a prism, see Fig.15.

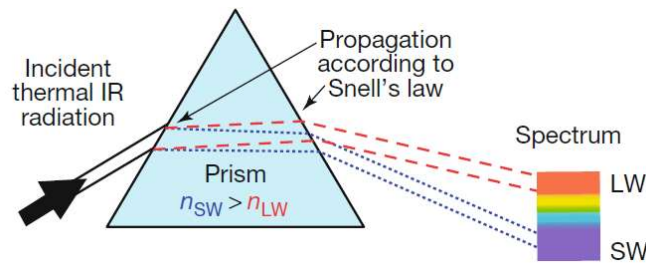


Figure 15 - IR Spectrum generated from a collimated beam of electromagnetic radiation using a not absorbing prism [15].

The angles of refracted light within the prism are determined from the law of refraction. If the index of refraction decreases with increasing wavelength, the radiation with longer wavelength is refracted less than the short wavelength radiation. The same holds for the second boundary of the prism. As a result, the incident electromagnetic radiation is spread out into a spectrum behind the prism [15].

2.4 Historical Background

Even though the order that this chapter will follow to explain the various thermodynamic radiation laws will start by defining the Planck's law as the first step necessary to derive the other laws, it was done for simplicity both graphically and numerically. In fairness the chronological order of this set of laws is in reverse as it is shown in Table 2. In fact, the fundamental mechanisms underlying radiation heat exchange was first successfully explained by Josef Stefan in 1879 when he proposed the correlation model about the dependence of radiative heat exchange on the temperature to the fourth power (T^4), which later was proved by Ludwig Boltzmann. Later on, Wilhem Wien, who was studying the fundamental nature of electromagnetic radiation and its relation to energy, proposed a relation stating that the wavelength at which the maximum amount of radiation was emitted occurred when the product of the wavelength and the temperature was equal to a constant, this became known as Wien's Displacement Law. At the end of the 19th century Rayleigh and Jeans approximated the blackbody radiation spectrum in asymptotical cases, but was only in 1901 that Max Planck finalized his formula by making one major assumption, that indeed light is emitted in a discrete form not continuously, which would lay the foundation of quantum physics and the derivation of a universal physical constant (Planck's constant h) [18].

Table 2 - Chronology of Radiation Laws

Equation	Mathematics	Year of publication
Planck law	$E_{\lambda, BB}(\lambda, T_{BB})$	1901
Wien Displacement	<i>derivative of $E_{\lambda, BB}(\lambda, T_{BB})$ w.r. t T_{BB}</i>	1893
Stefan Boltzmann law	<i>integral of $E_{\lambda, BB}(\lambda, T_{BB})$ w.r. t λ</i>	1879
Rayleigh-Jeans	$E_{\lambda, BB}(\lambda, T_{BB})$ thermodynamic arguments	1900
Wien's approximation	$E_{\lambda, BB}(\lambda, T_{BB})$ fitting experimental data	1896

2.5 Planck's Law

In radiometry, a blackbody is considered a perfect emitter and absorber, in this sense it is used as a calibration reference for quantitative measurements. The relation between blackbody spectral irradiance, wavelength and temperature is expressed in Eq.8.

$$E_{\lambda, BB}(\lambda, T_{BB}) = \frac{2 \cdot \pi \cdot h \cdot c_0^2}{\lambda^5} \cdot \frac{1}{e^{\left(\frac{h \cdot c_0}{\lambda \cdot k \cdot T_{BB}}\right)} - 1} = \frac{c_1}{\lambda^5} \cdot \frac{1}{e^{\left(\frac{c_2}{\lambda \cdot T_{BB}}\right)} - 1} \quad \text{Eq.8}$$

where:

- $E_{\lambda, BB}$ is the blackbody spectral irradiance expressed in [W m⁻³] per unit surface [m⁻²] and wavelength [m⁻¹]
- λ is the wavelength, commonly expressed in [nm] (1e-9) or [μm] (1e-6) and converted to m for the above equation
- T_{BB} is the blackbody temperature expressed in Kelvins [K] -> T[K]=T[°C]+273.15

it is possible to understand Eq.8 without c1/c2, however these are commonly used as such:

- $c_1 = 2 \cdot \pi \cdot h \cdot c_0^2$ or 3.741771852*1e-16 [W m⁻²] is the first radiation constant
- $c_2 = \frac{h \cdot c_0}{k}$ or 1.438776877*1e-2 [m K] is the second radiation constant

A representation of this function is displayed in Fig.16.

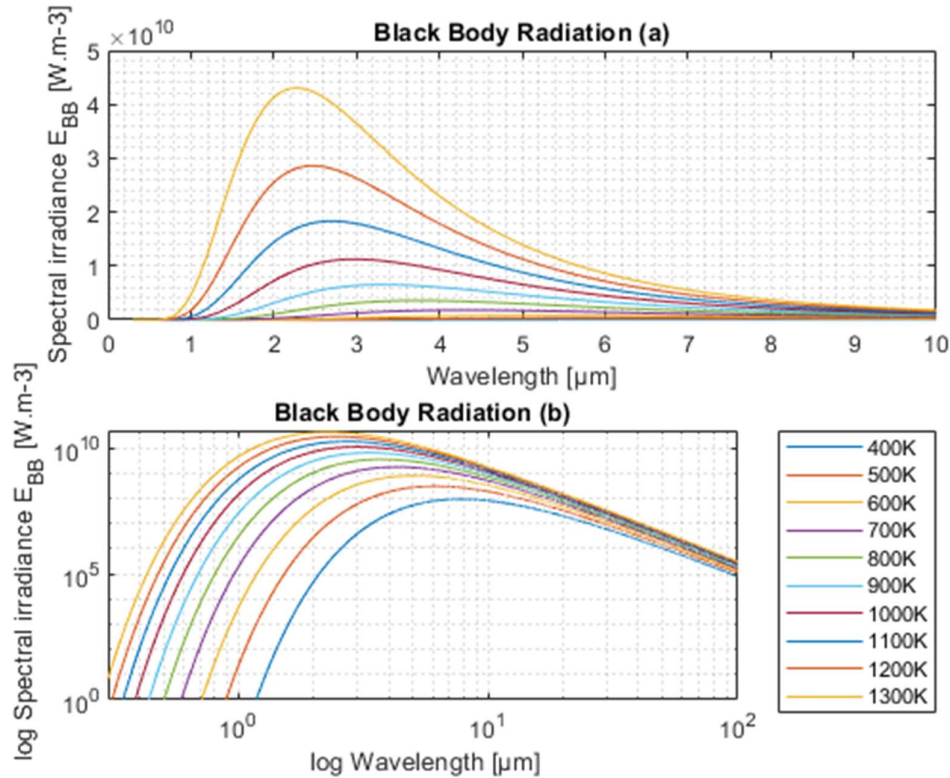


Figure 16 - Planck blackbody function designed with MatLab® software by using as input the previous Planck's equation (Eq.8), it needs to be mentioned that a set of 10 different temperatures was chosen ranging from 400 K to 1300 K. a) Graph show as usual plot function to underline the various peaks. b) Graph shown with loglog function to highlights lower temperatures otherwise not visible

2.6 Wien's displacement Law

In this case is possible to see how, maintaining all the variables explained in the list above constant except for the temperature, the shape of the curve changes accordingly. In particular, the higher is the temperature, the higher will be the value of the peak. It is possible to observe that not only the peak maximum is changing in function of the temperature also its abscissa is shifting toward shorter wavelengths, see Fig.17.

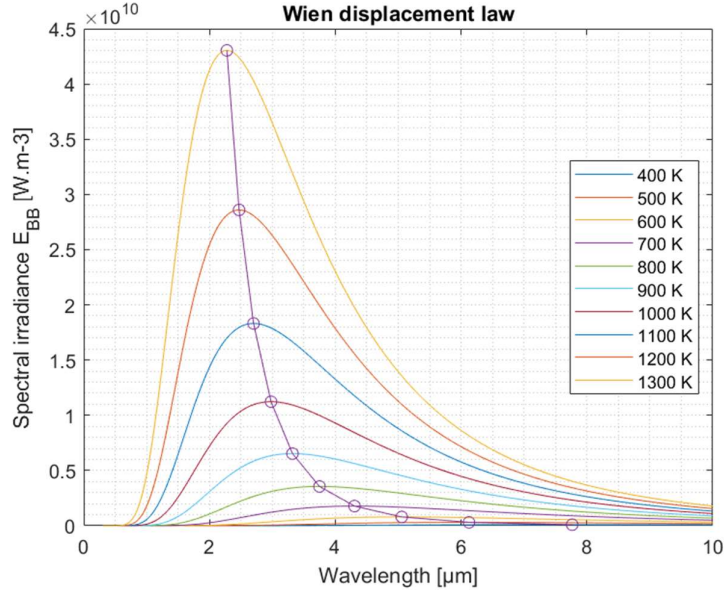


Figure 17 - Wien's displacement law

This relation is called Wien's displacement law and it can be obtained by setting the first derivative of the Planck radiation formula equal to zero, as expressed in Eq.9. The full calculation is displayed in the digital appendix of this work.

$$\frac{d}{d\lambda} = \left[\frac{1}{\lambda^5} \frac{1}{e^{\frac{c_2}{\lambda T}} - 1} \right] = 0 \text{ with } c_2 = \frac{hc_0}{k} \quad \text{Eq.9}$$

The end result of the calculation is the following formula (Eq.10):

$$\lambda_{peak} T = 2,989 \times 10^{-3} [m K] \quad \text{Eq.10}$$

2.7 Stefan Boltzmann's Law

Another information about the characteristic of the object that can be extracted from (Eq.8) is the spectral emissive power P , this latter corresponds to the area underneath the spectral irradiance curve, which as we have demonstrated before depends exclusively on the temperature of the blackbody. In physics, Stefan-Boltzmann's law is used usually to calculate total radiated power of stars from their known surface area and surface temperature [15], in the following picture (Fig.18) it is shown graphically.

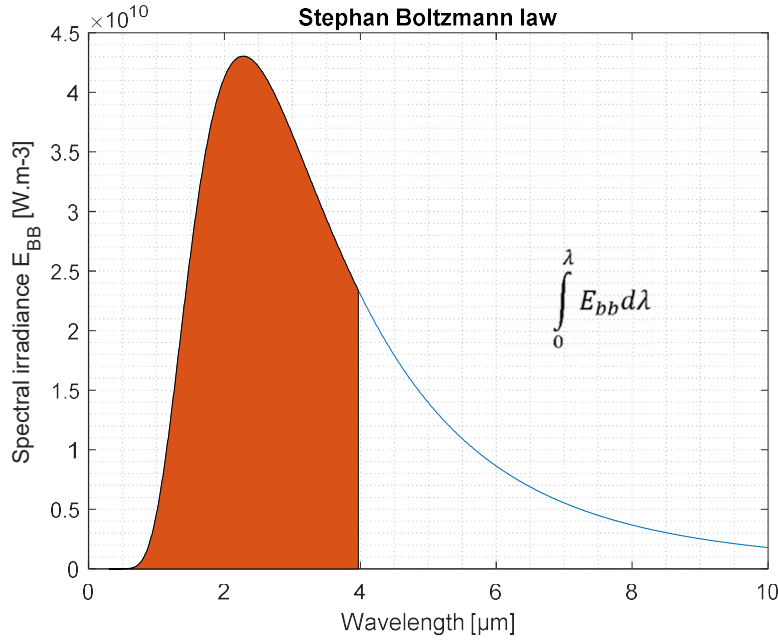


Figure 18 - Stefan-Boltzmann law's considering a blackbody at 1300K

The full derivation of this law is shown in the digital appendix for a better understanding of the various steps, as follow only the output is displayed (Eq.11):

$$\frac{P}{A} = \sigma \cdot T^4 \quad \text{Eq.11}$$

This result shows how the total energy radiated by a blackbody is proportional to the fourth power of the blackbody temperature. It is important to notice that the spectral emissive power is only a function of temperature but not of wavelength. Nonetheless, the temperature exponent is wavelength dependent, the fourth power corresponding to the full electromagnetic spectrum.

2.8 Emissivity

So far, in order to explain the various laws that govern infrared physics, the focus was set on blackbodies. However, in a real measurement scene, a blackbody is used most often only as a reference calibration source, taking into consideration that by the definition no other object at given temperature can emit more thermal energy than a blackbody. The ratio of the energy emitted by the blackbody and the body taken into analysis at that specific temperature can be identified as a new property, which is called emissivity. The latter is a property specific for any materials and it can be defined with the following equation Eq.12:

$$\varepsilon(\lambda, T, \delta, \varphi) = \frac{E(\lambda, T, \delta, \varphi)}{E_{BB}(\lambda, T)} \quad \text{Eq.12}$$

As it is written, in this case the emissivity of the measurement object depends on a series of parameters such as wavelength λ , temperature T and the view angle. In this sense it can be expressed by the azimuthal angle (φ) and the zenith angle (δ). It is important to specify this characteristic because while a blackbody is a perfect isotropic emitter, real objects are not and therefore their emissivity is dependent also on the point of view of the measurement, also another characteristic is that by definition emissivity is restricted in the interval [0:1] [15].

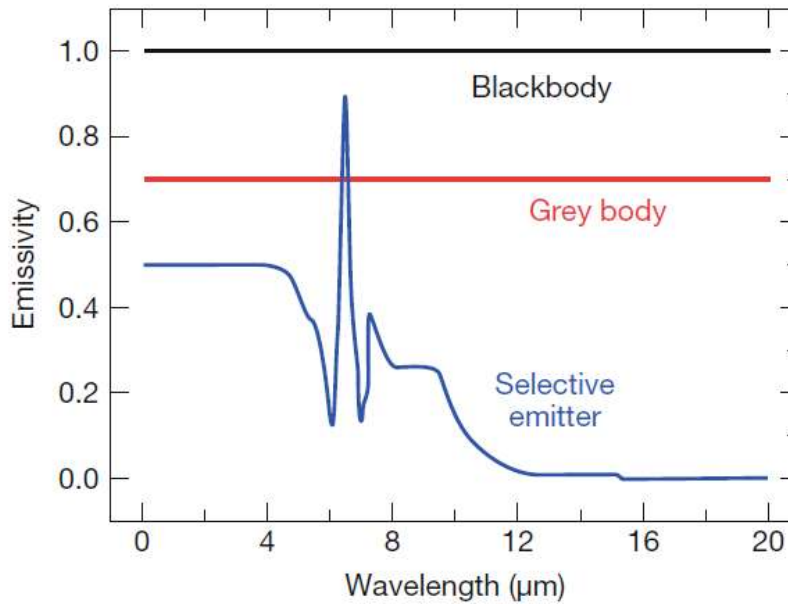


Figure 19 - Emissivity comparison [15].

It is possible to categorize from this equation different behaviors, as illustrated in Fig.19 there are three main categories. The first one is the blackbody, that has already been described in this paragraph. The second one is commonly known as the graybody, which emissivity is independent of the wavelength ($\varepsilon = \text{constant}, \forall \lambda$). The last one is the selective emitter, which emissivity is dependent of the wavelength and usually the most common behavior for real objects.

2.9 Kirchhoff's Law of Radiation

Knowing the material emissivity at a given temperature it is possible to guess also its absorptivity [15]. In fact as the Kirchhoff law of thermal radiation states, for an arbitrary body emitting and absorbing thermal radiation in thermodynamic equilibrium, the emissivity is equal to the absorptivity. It can be summarized in the following equation (Eq.13).

$$\varepsilon = \alpha \quad \text{Eq.13}$$

where ε is as mentioned before the emissivity while the absorptivity is defined as α . According to energy conservation any radiation (ϕ_0) incident on any object can be divided into three major contributions. In particular it can be reflected (ϕ_R), whether it is directed according to the law of reflection or diffusely scattered from rough surfaces, transmitted (ϕ_T) through the object or absorbed (ϕ_A) within the object. The equation that describes it can be found as follows (Eq.14):

$$\phi_0 = \phi_R + \phi_T + \phi_A \quad \text{Eq.14}$$

This equation (Eq.14) can be rearranged in order to calculate the emissivity from the previous mentioned contributions, in this case the total radiation is supposed to be equal to 1 so it can be written like:

$$\varepsilon = 1 - \rho - \tau \quad \text{Eq.15}$$

where ρ and τ are respectively the fraction of the incident radiation which is reflected and the one that is transmitted. From this equation one can infer that the emissivity depends on a series of parameters. One half consists in parameters intrinsic in the object such as:

- material
- the surface micro-structure
- the observation direction.

Other parameters depend mostly on other variations more likely to be external of the object, in this case it is possible to indicate a few of them such:

- temperature
- wavelength
- macroscopic geometry.

Regarding the part of radiation that gets reflected the parameter that most affects this phenomenon is the roughness of the surface (R), see Fig.20. This example illustrates the transition from specular reflection, to diffuse reflection caused by the increased roughness of the body surface [15]. Another intrinsic parameter listed before that can affect the measurement is the direction of the observation, in Fig.21. Reflected radiation is made of two different components, the first one is polarized parallel (R_π) to the plane and the second one is polarized perpendicular (R_σ) to the plane of incidence. The parallel component first decreases from the same starting value at $\alpha = 0^\circ$ then it reaches a specific angle, called the Brewster angle that is the point with zero reflectivity, and after it steeply rises to the maximum value of 1.0. In general, the Brewster angle α_{Br} is defined as such (Eq.16).

$$\tan(\alpha_{Br}) = \frac{\sin(\alpha_{Br})}{\cos(\alpha_{Br})} = \frac{n_B}{n_A} \quad \text{Eq.16}$$

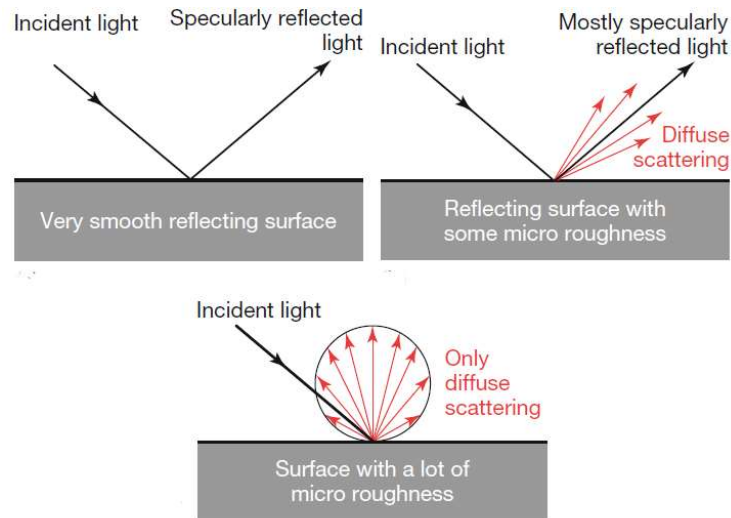


Figure 20 - Transition from a smooth surface to rough one and the change in reflectivity that that this implies [15].

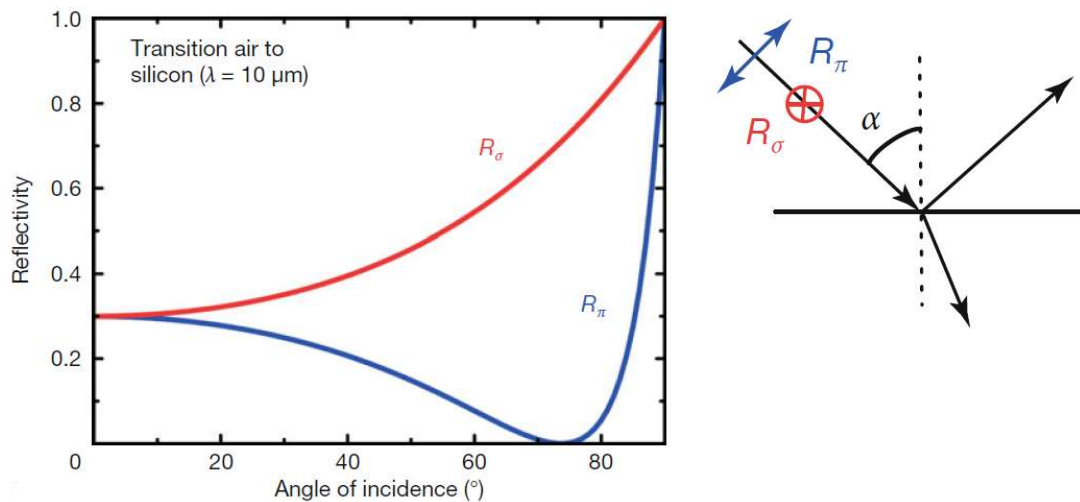


Figure 21 - Dependence of the portion of reflected IR radiation on the angle of incidence in a transition from air to silicon [15].

2.10 Infrared Thermography

In recent years, the attention of researchers has been focused on the IR thermography due to its great potential as a remote sensing, non-destructive, real time and in-situ inspection method. However, many limitations affect this technique. The main issue is due to the a priori knowledge of the material emissivity, given the strong dependence of the surface radiation on the emissivity. In applications where the surface emissivity of the material changes considerably with the temperature, such as ablation and erosion or oxidation effects, this technique fail [19]. After been affected by the atmosphere or surrounding interference the final measurement depends on the IR system employed, which is characterized by its own spectral response and spectral band of detection [20]. The aim of this thesis is to evaluate a possible IR measurement technique which could be deployed to analyzed various material type using a spectral response in the SWIR, MWIR or LWIR in order to obtain information about both emissivity and temperature for tube receiver solar power tower plants.

2.11 Infrared System

After the discussion in the previous paragraphs about the physics behind the IR measurement technique, the next theme that need to be addressed is how an IR system can read and decode this information. The component designed for this task is the detector, there are mainly two different categories of it, one is the photon detector while the other one is the thermal detector [21]. The photon detectors are a single step transduction (for instance semiconductor materials because of the photovoltaic effect) where the absorption of photons from the IR radiation leads to change in the concentration or mobility of the free charge carriers in the detector element [15]. On the other hand thermal detectors are two steps transducers, in fact the absorbed radiation generates a temperature change in the material, which then generates an electrical resistance change in a temperature dependent apparatus, this is the specific case for the bolometer, widely used in LWIR measuring system [22]. An example of the latter is visualized in the following schematic picture (Fig.22).

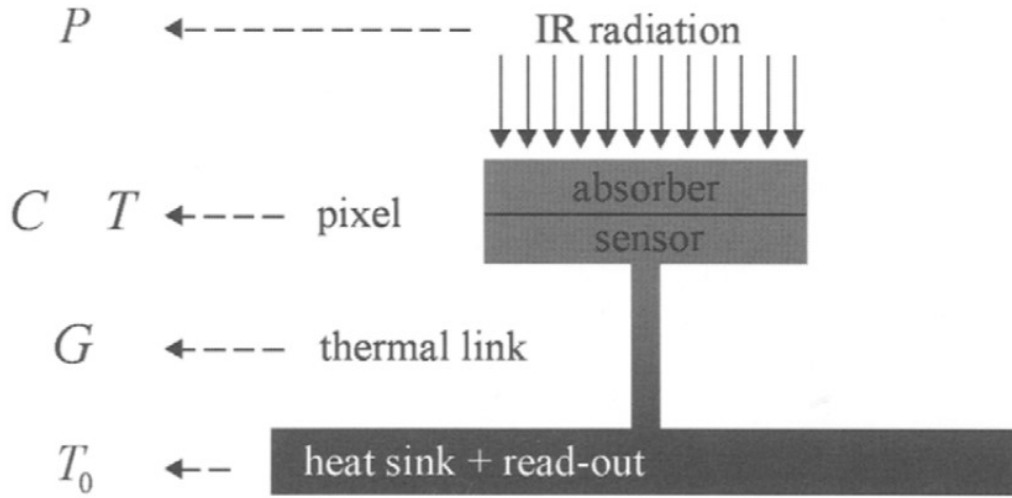


Figure 22 - Schematic representation of a microbolometer [22].

Where:

- P represents the radiation power [W]
- C the heat capacity of the pixel [J/K]
- T the temperature of the pixel [K]
- G the thermal conductance of the support [$\text{W}\cdot\text{K}^{-1}$]
- T_0 the temperature of the heat sink [K]

As explained previously, the IR radiation gets absorbed by the pixel, which is heated up, and this creates a remarkable change in resistance caused by a thermal imbalance generated by the fact that the pixel warms up faster than the heat sink, also due to the low thermal conductance G of the support. The basic equation that explain the phenomenon on which this system is based is explained as follows (Eq.17), with t being the time of the response.

$$\alpha P = C \frac{dT}{dt} + G(T - T_0) \quad \text{Eq.17}$$

Considering adiabatic boundary conditions, in which the isolation is secure so there are no temperature loss or unwanted exchange of it with the surroundings, the temperature increase of the bolometer is proportional to the absorbed power and inversely proportional to the thermal conductivity. This means that high thermal isolation leads to more heating that results in a better output signal. This is also why the heat capacity C of the pixel determines the response rate, faster the

pixel can be heated up faster it will reach the maximum temperature difference with the heat sink. There are mainly two different geometry designs of microbolometer base on this concept. The first one represents a self-suspended bolometer, in this case like it was shown in the schematic picture before (Fig.22) the pixel is supported by a resistive sensor that provides at the same time structural mechanical strength and the thermal link necessary for the analysis. In the second concept the main design different is due to the fact that the pixel is supported by a membrane. As illustrated in Fig.23, which shows the fabrication process of such bolometer, there are two possible configurations for the membrane design, in fact the bolometer can have either a planar or a sandwich structure.

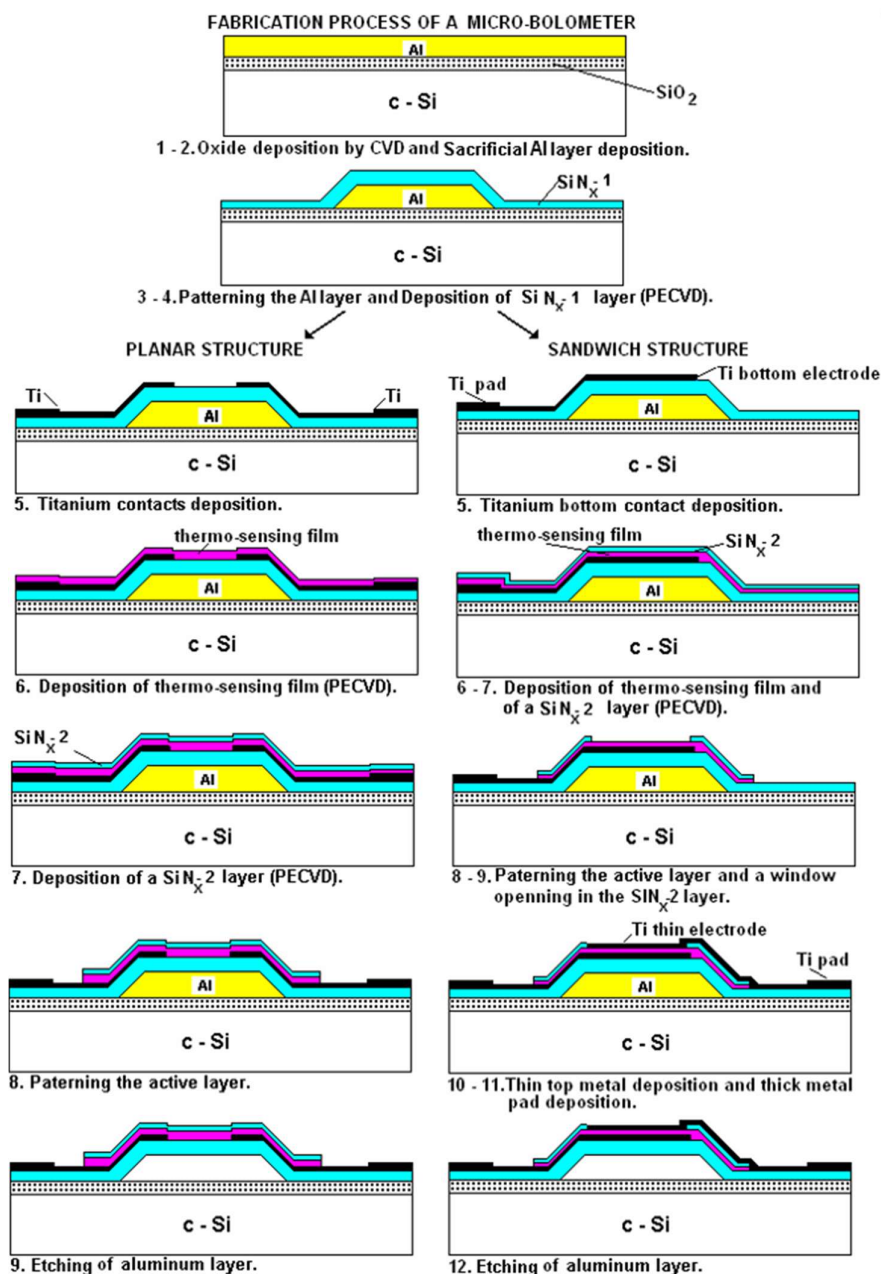


Figure 23 - Fabrication technique for a membrane suspended microbolometer with highlight in the different in the process for either a planar or sandwich structure [23].

The membrane will provide the mechanical support but not the electric contact, that will still be generated within the thermal link, this converts in a worse isolation for the microbolometers but give a possibility in using certain materials that otherwise would not be possible. In fact due to the process

that material need to undergo to obtain this particular structure Ti-metal, α -Si and poly-SiGe or VOx bolometers can be found in literature or on the market [22]. Since microbolometers are used especially for LWIR measurements, more examples of materials used in detectors for the other two wavelength ranges are reported in the following pictures (Fig.24).

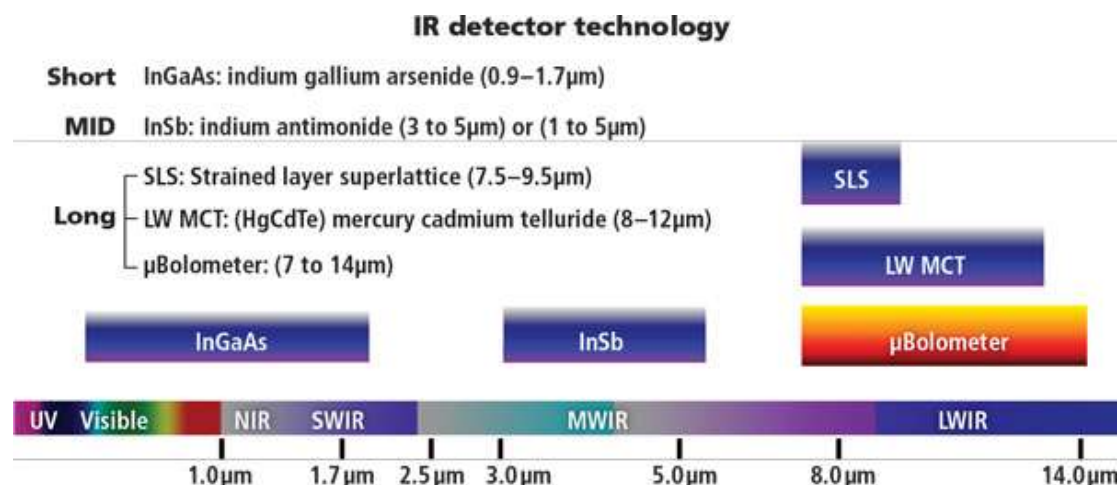


Figure 24 - IR detector materials possibilities [24].

2.11 IR Methods

In the first two sections of this chapter, IR imaging basics were explained and the way to transform the radiation into a readable information data, however using only the detector to receive and process the information from the target object is not sufficient. In this paragraph some of the most common advance techniques in IR measurements system will be analyzed. First of all, in order to tune precisely the camera response on the target radiation range the most effective approach is to use filter, there are four major classes of spectral filter, as reported in the following list:

- SP: short-pass
- LP: long-pass
- BP: bandpass
- NBP: narrow bandpass

The comparison of the various categories is shown in the following graph (Fig.25). Shortpass filters let pass radiation above a certain wavelength (cut-off), while longpass filters let pass radiation below a certain wavelength. Bandpass filters on the other hand are targeting a specific range of wavelength with the normal BP filters covering a bigger spectral response than theirs more specifically tuned counterpart NBP that cover just a narrow wavelength range, this generates a highly precise spectral analysis [15]. In this thesis we focused our attention manly on this latest class of filter as it will be explained in the next chapters.

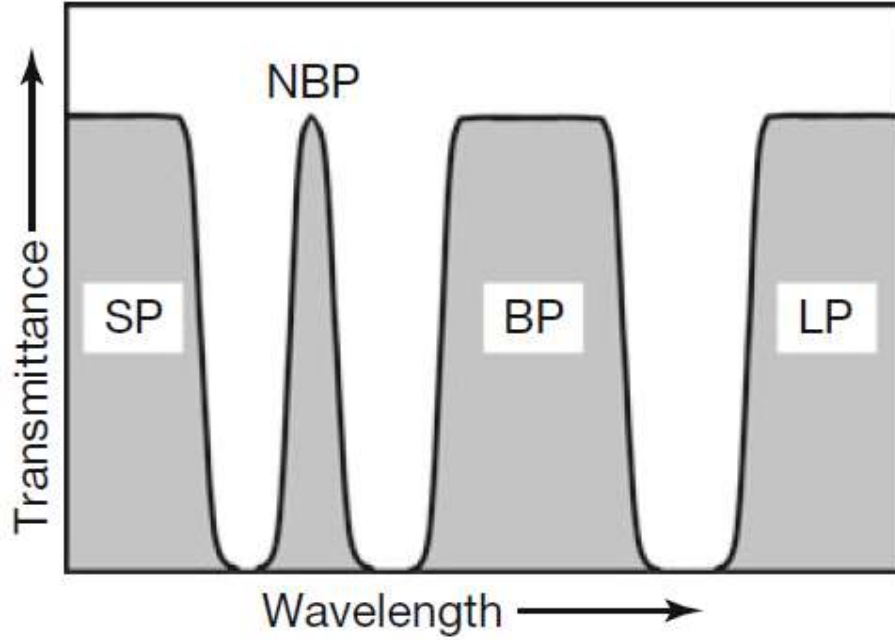


Figure 25 - Spectral filter options [15].

The type of filter mostly used for this kind of application is the interference or dichroic filter, in fact while it reflects the band or bands of interested and it transmits the other, it maintains a nearly zero coefficient of absorption for the chosen wavelength range . This latter point is crucial for the detector response error, in fact if the filter would absorb any of the incident radiation, its temperature would increase resulting in an additional radiation from the filter that will compromise the measurement.

There are mainly two different possibilities in term of filter configuration. The first spectral profile is called monochromatic analysis and it is focused on a specific central wavelength specification of the filter. On the other hand, It can be performed by equipping the Infrared camera of two band pass or narrow band pass filters in order to consider the emissivity parameter as a constant value, this methodology is called dual or two color technique [19]. The latter thermography allows the calculation of the ratio of two monochromatic radiations evaluated from two spectral band filters with central wavelengths close to each other. The object temperature is determined by the ratio of the measured intensity radiation, obtaining the Intensity Radiation Ratio (IRR) value, as shown in the following equation (Eq.18a):

$$IRR = \frac{\varepsilon_{\lambda_i} E_{n,\lambda_i}(T_{obj})}{\varepsilon_{\lambda_j} E_{n,\lambda_j}(T_{obj})} \quad Eq.18a$$

Where E_{n,λ_i} is the monochromatic intensity of radiation calculated with the Planck equation (Eq.8). If the two BP filters are chosen close enough to each other the gray body assumption can be considered valid and as a consequence the two emissivity can be neglected and the result equation would be as follow Eq.18b:

$$IRR = \frac{E_{n,\lambda_i}(T_{obj})}{E_{n,\lambda_j}(T_{obj})} \quad Eq.18b$$

In order to apply properly the dual color technique analysis, avoiding errors in the measurement, there are two aspects that have to be taken into consideration to obtain an accurate result, such as:

- reflected radiation of the external environment
- behavior influence of a non-gray body object

As for other techniques, there are additional standard parameters that play a key role in the successful result of the measurement for example:

- the spectral sensitivity
- spectral behavior of the filter
- signal to noise ratio
- filter calibration.

The accuracy of the mathematical model of the dual color technique depends on the environment and the possibility of implementing into the model all sort of radiations coming towards the camera. described further in the next paragraph.

2.12 Radiometric Chain

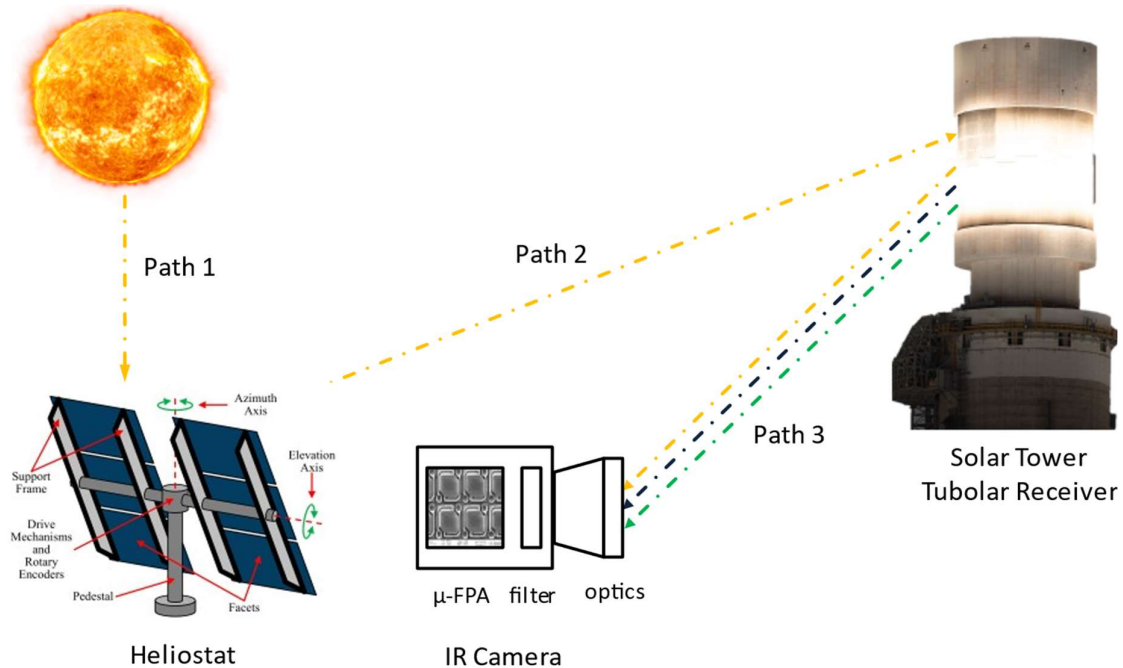


Figure 26 - Illustration of the radiometric chain taken into analysis, for the purpose of this work.

The radiometric chain described in the picture above (Fig.26) describes the three atmospheric paths to which the radiation is subjected before reaching the camera. The most important aspect to address is the fact that the camera receives radiation from every surrounding object and not only from the focused object, these radiations are also attenuated in a certain degree from the atmosphere present along the various paths, therefore the resulting effects need to be implement in the model as expressed in the following equation Eq.19, it is written in integral form so it is referred as a band signal, in case of a monochromatic analysis it will be written removing integral symbols, for a specific wavelength λ .

$$\begin{aligned}
S_{filter_k}(T_{bb}) = & \int_{\lambda_{start}}^{\lambda_{stop}} \varepsilon(\lambda, T_{bb}) \cdot \tau_3(\lambda) \cdot F_k(\lambda) \cdot R(\lambda) \cdot E_{bb}(\lambda, T_{bb}) d\lambda \\
& + C_x \int_{\lambda_{start}}^{\lambda_{stop}} [1 - \varepsilon(\lambda, T_{bb})] \cdot \tau_3(\lambda) \cdot \tau_2(\lambda) \cdot \tau_1(\lambda) \cdot \rho_{spec}(\lambda) \cdot F_k(\lambda) \cdot R(\lambda) \cdot SI(\lambda, AM) d\lambda \\
& + \int_{\lambda_{start}}^{\lambda_{stop}} [1 - \tau_3(\lambda)] \cdot F_k(\lambda) \cdot R(\lambda) \cdot E_{bb}(\lambda, T_{atm}) d\lambda \\
& + \int_{\lambda_{start}}^{\lambda_{stop}} [1 - F_k(\lambda)] \cdot R(\lambda) \cdot E_{bb}(\lambda, T_{chip}) d\lambda
\end{aligned} \tag{Eq. 19}$$

Where:

- $\varepsilon(\lambda, T_{bb})$ is the emissivity coefficient of the black body
- $\tau_3(\lambda)$ is transmission coefficient of path3 (from the body to the camera)
- $\tau_2(\lambda)$ is the transmission coefficient of path2 (from the mirrors to the body)
- $\tau_1(\lambda)$ is the transmission coefficient of path1 (from the sun to the mirrors)
- $F_k(\lambda)$ is the filter signal contribution
- $R(\lambda)$ is the detector signal contribution
- $E_{bb}(\lambda, T_{bb})$ is the spectral black body emissive power
- $E_{bb}(\lambda, T_{atm})$ is the spectral atmospheric emissive power
- $E_{bb}(\lambda, T_{chip})$ is the spectral emissive power of the camera detector chip
- C_x is the concentration factor
- $\rho_{spec}(\lambda)$ is the mirror reflectance
- $SI(\lambda, AM)$ is the solar irradiance
- $S_{filter_k}(T_{bb})$ is the filtered signal received by camera

The Eq.19 can be divided into three different contributions, as highlighted in Fig.26 with the three different colors of the resulting effects on the signal received by the camera. In the following list these three contributions are explained in greater details:

- Band signal for a blackbody (term1: green dotted line on Fig. 26)

$$\begin{aligned}
S_{band\ bb} = & \int_{\lambda_{start}}^{\lambda_{stop}} \varepsilon(\lambda, T_{bb}) \cdot \tau_3(\lambda) \cdot F_k(\lambda) \cdot R(\lambda) \cdot E_{bb}(\lambda, T_{bb}) d\lambda + \\
& \int_{\lambda_{start}}^{\lambda_{stop}} [1 - F_k(\lambda)] \cdot R(\lambda) \cdot E_{bb}(\lambda, T_{chip}) d\lambda
\end{aligned}$$

The second part of this first term can be explained by Fig.27, in the scheme that follows it is possible to see the influence of both the camera chip and the filter on the signal. In fact, after the radiation from the body of analysis (ϕ_s) reaches the optics of the camera, as described in Fig.27, it will be transmitted by the filter (ϕ_T) but at the same time also the filter will emit a certain amount of radiation (ϕ_E). These two contributions will sum up with the radiation emitted by the chip itself and then reflected (ϕ_R) from the back of the filter onto the detector.

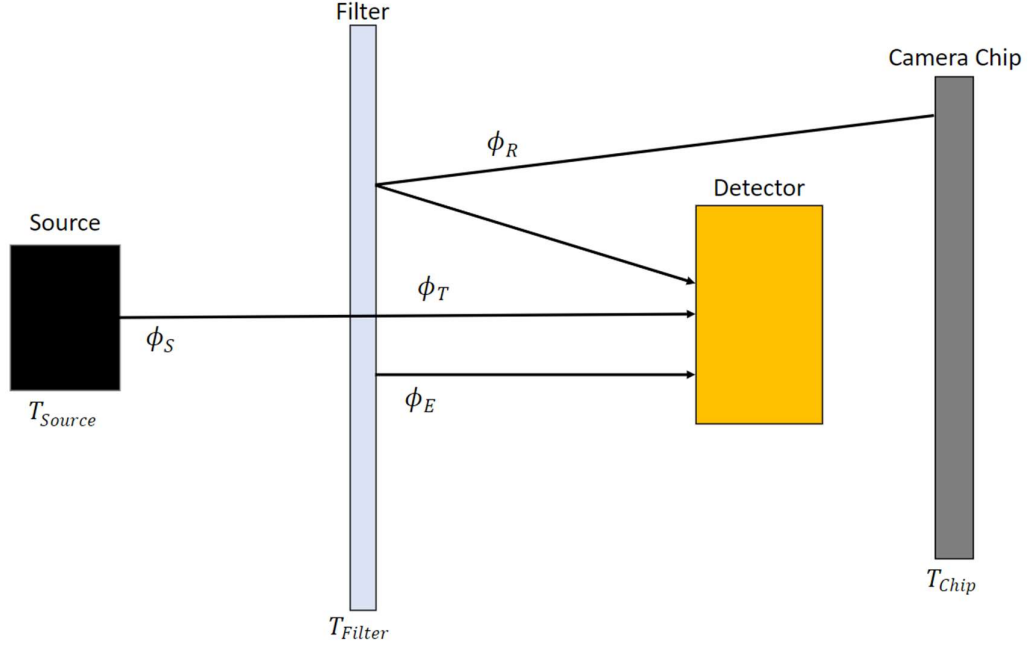


Figure 27 - Filtered Signal Scheme and contribution of Detector and Camera [25].

- Radiation from the sun (term2: orange dotted line on Fig.26)

$$S_{sun} = C_x \int_{\lambda_{start}}^{\lambda_{stop}} [1 - \varepsilon(\lambda, T_{bb})] \cdot \tau_3(\lambda) \cdot \tau_2(\lambda) \cdot \tau_1(\lambda) \cdot \rho_{spec}(\lambda) \cdot F_k(\lambda) \cdot R(\lambda) \cdot SI(\lambda, AM) d\lambda$$

This term highlights how the radiation from the sun gets affected by the transmittance of the atmosphere through the three different paths. It also includes the influence of the mirrors and the camera response.

- Noise from the surroundings (term3: blue dotted line on Fig.26)

$$S_{noise} = \int_{\lambda_{start}}^{\lambda_{stop}} [1 - \tau_3(\lambda)] \cdot F_k(\lambda) \cdot R(\lambda) \cdot E_{bb}(\lambda, T_{atm}) d\lambda$$

The equation expresses clearly how the noise affecting the final signal is generated by the atmospheric influence in the third path, this aspect will be covered in greater details in the next chapter about the simulation model.

The last configuration to be discussed regarding the possible filter choice is about their central wavelength, in fact while the filters wavelengths λ_i and λ_j should be chosen as close as possible to consider valid the grey body assumption on the other hand if the two wavelengths are too similar the signal will be negatively affected since the signal ratio derivative decreases with the decrease of λ_i and λ_j differences [19].

3. Methodology

Coding process

3.1 Acknowledgment of the Software used

The core of this work is built on a series of simulations using MatLab®, which is a programming language developed by MathWorks based on matrix and arrays. The main operating characteristics of this software cover basic functions, data structures, with the possibility of input/output feature, object-oriented programming and numerical computing. Its name derives from the abbreviation of Matrix Laboratory. The main source of documentation, that represents the backbone for all the functionality highlighted before, is the MatLab® mathematical function library, which is a vast collection of computational algorithms ranging from elementary functions like sum, sine and cosine to more sophisticated functions like matrix inverse or Fourier transforms [26]. It is important to add that the way we followed to generate the code was done by the use of structures, in the MatLab® Documentation is explained as follow [27]:

A structure array is a data type that groups related data using data containers called fields. Each field can contain any type of data. Access data in a field using dot notation of the form structName.fieldName.

These variables were used in the first place to create a structure that represents every scenario analyzed during this work. The use of this kind of structures was essential because they let us compute a wide range of possibilities with a modular code design.

3.2 Model Introduction

The success of a simulation is based on creating an accurate model of the real object into consideration. In order to do so, it is necessary to understand the boundary conditions of the real analysis and the implementation of variables, which can be fine-tuned to achieve the focus of the analysis. As shown in (Fig.26), the radiometric chain is characterized by a layering of interactions that the original radiation from the sun undergoes along the pathways, for this reason in this work we decide to recreate this layered configuration into the radiometric model, that has been created through a series of structures and functions in MatLab®. The main architecture is illustrated in (Fig.28).

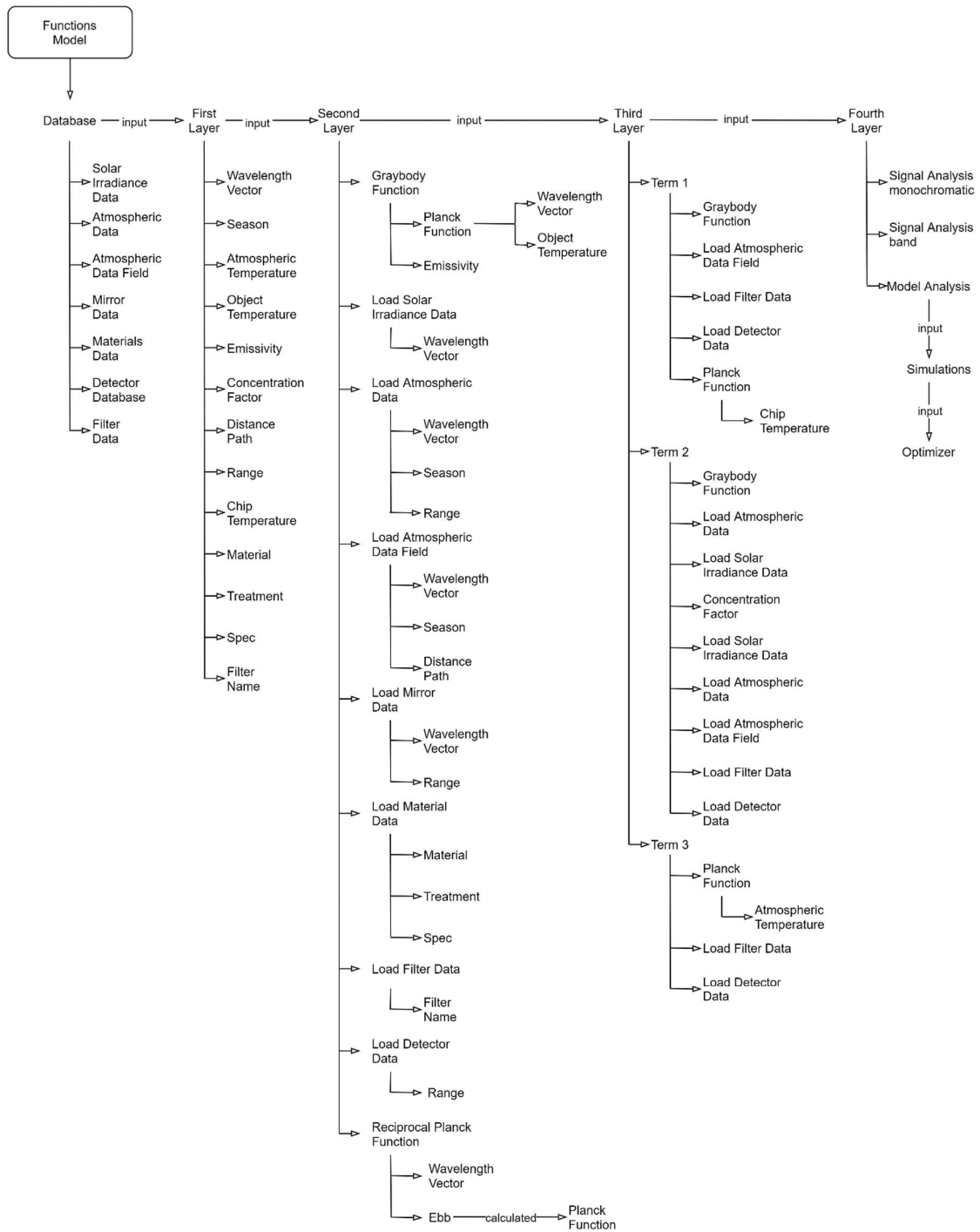


Figure 28 - Function synoptical map

3.3 Database (Layer 0)

The synoptical map in Fig.28 explains how our layering of functions is divided into four different levels. The first step in the building up of the various sections is the creation of a general Database core divided into seven different sub databases, that have been collected as follow.

1) Solar Spectral Irradiance: ASTM E490 standard [28].

In the year 2000 the American Society for Testing and Materials (ASTM) developed an Air Mass (AM0) reference spectrum referred as the ASTM E-490, designed for use by the aerospace community. The ASTM E-490 standard is based on data from satellites, space shuttle missions, high-altitude aircraft, rocket soundings, ground-based solar telescopes and modeled spectral irradiance. The model was made in accordance to the value of the solar constant accepted by the space community, which is 1366.1 W/m^2 [28]. The following graph (Fig.29) represents the visualization of the ASTM E490 standard dataset.

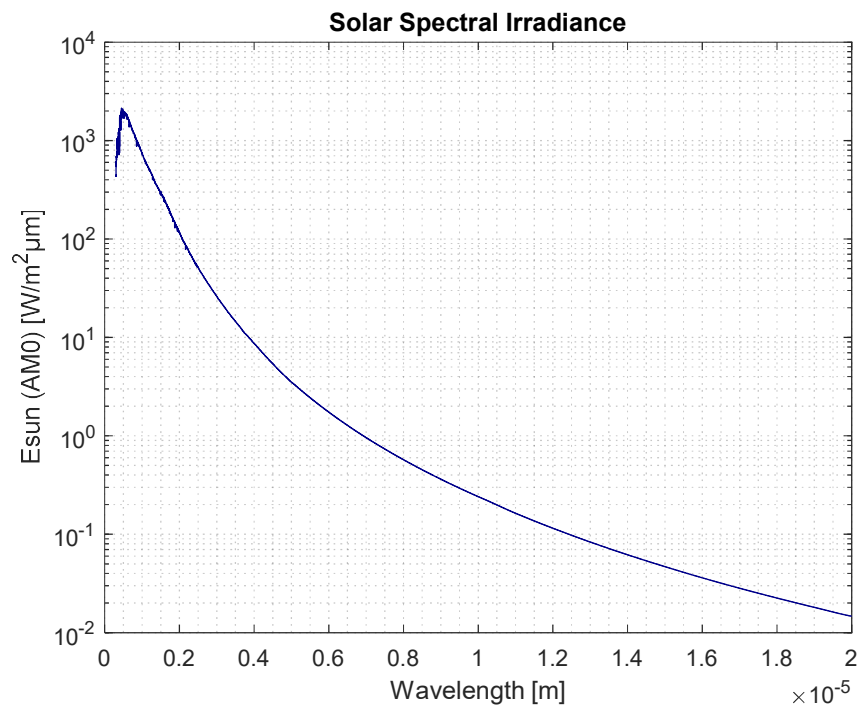


Figure 29 - Solar spectral irradiance database graphical visualization [28].

2) Atmospheric Data: ModTran Online Software and SMARTS Files [29].

Before going into the details of the atmosphere database it is reasonable to explain first that the atmosphere is a mixture of various gases, which composition is summarized in Table 3.

Table 3 - Atmosphere gases composition [30].

Gas		Volume
Name	Symbol	%
Nitrogen	N ₂	78.084
Oxygen	O ₂	20.946
Argon	Ar	0.9340
Carbon dioxide	CO ₂	0.041500
Neon	Ne	0.001818
Helium	He	0.000524
Methane	CH ₄	0.000187
Krypton	Kr	0.000114

Due to the changes in both pressure and temperature the atmosphere is characterized by a stratification of multiple layers, which structure is illustrated in Fig.30.

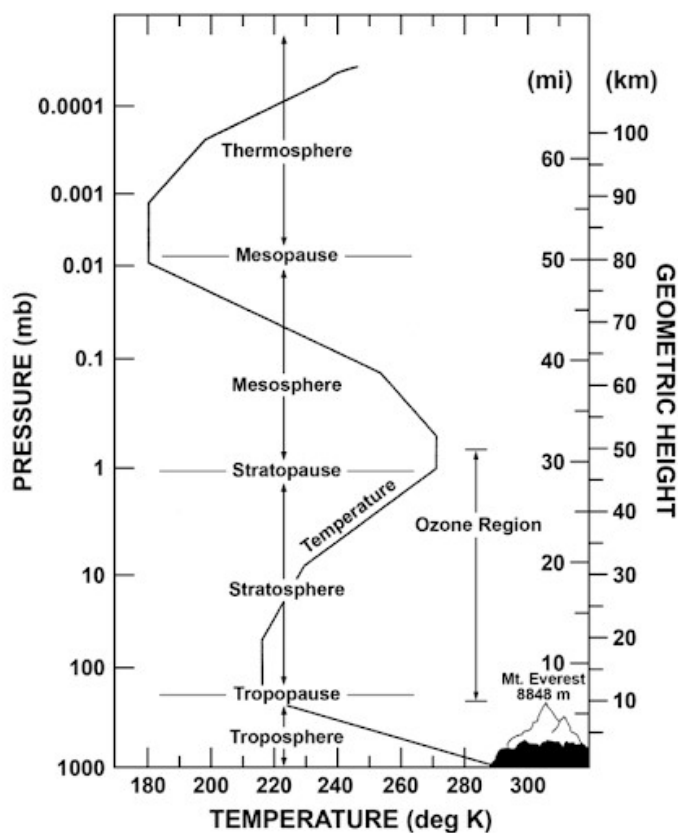


Figure 30 - Earth Atmosphere stratification diagram [31].

The different layers within Earth's atmosphere can be described as follow:

- The *Troposphere*, which starts at the Earth's surface and extends to a height of 8 to 14.5 kilometers. It is the densest part of the atmosphere.
- The *Stratosphere* lays just above the troposphere and extends up to a height of 50 kilometers. This layer includes the ozone layer, which absorbs and scatters the solar ultraviolet radiation and also the IR radiation in the LWIR range around 9.5 μm .
- The *Mesosphere* begins above the stratosphere and extends up to a height of 85 kilometers. Meteors usually burn up in this layer.
- The Thermosphere is situated above the mesosphere and it extends up to a height of 100 kilometers. Aurora events are observed in this layer [32].

In this context a model that can contain the majority of this atmosphere characteristics was generated. The MODTRAN® software, which stands for MODerate resolution atmospheric TRANsmission, is a computer code that was developed by a collaboration between Spectral Sciences Research Development Organization (SSI) and the Air Force Research Laboratory (AFRL). The code is embedded in many operational and research sensor as in data processing systems, particularly those involving the removal of atmospheric effects, commonly referred to as atmospheric correction. The core of the MODTRAN RT is an atmospheric narrow band model algorithm. The atmosphere is modeled via constituent vertical profiles, both molecular and particulate, defined either using built-in models, by user-specified radiosonde or climatology data. The band model provides resolution as fine as 0.2 cm^{-1} from its 0.1 cm^{-1} band model. MODTRAN solves the radiative transfer equation including the effects of molecular, particulate absorption/emission and scattering, surface reflections and emission, solar illumination and spherical refraction. In the following Table 4 an example of specifications for each Atmospheric Model for both seasons (Summer and Winter, Mid Latitude) is shown [29].

Table 4 - MODTRAN® data entry for each season [29].

Atmospheric Models		
	MidLatitude Summer	MidLatitude Winter
<i>water vapor colum [atm-cm]</i>	3635.9	1059.7
<i>Ozone (O₃) [atm-cm]</i>	0.33176	0.37681
<i>CO₂ [ppmv]</i>	400	400
<i>CO [ppmv]</i>	0.15	0.15
<i>CH₄ [ppmv]</i>	1.8	1.8
<i>Ground Temperature [K]</i>	294.2	272.2
<i>Aerosol Model</i>	Rural	Rural
<i>Sensor Altitude [km]</i>	99	99
<i>Sensor Zenith [°]</i>	180	180
<i>Minimal Resolution [μm]</i>	0.098	0.098
<i>Data extraction</i>	WebPlotDigitizer	WebPlotDigitizer

It is also important to add the geometrical configuration of the sensor, in fact as shown in Fig.31 it lays with a zenith angle of 180 degree and it is positioned at 99 km, which as described before is within the Thermosphere layer (Karman line). This is crucial for our analysis, in order to understand and implement the correct atmospheric variables.

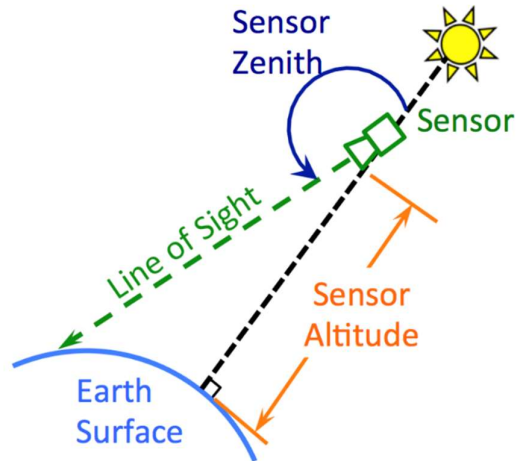
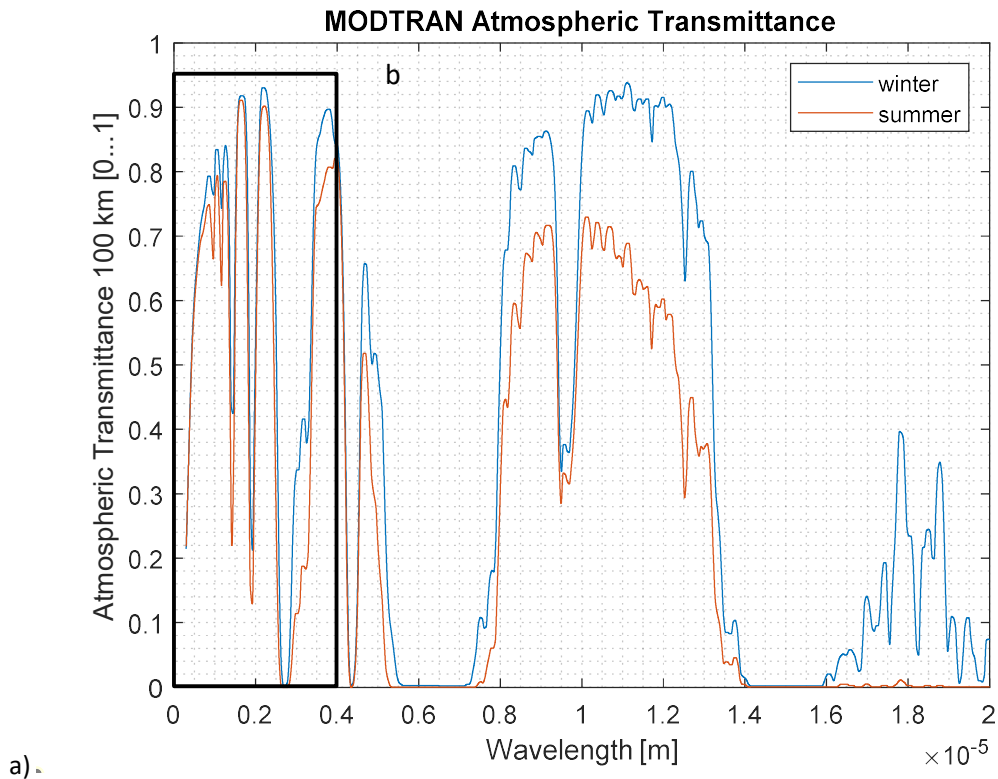
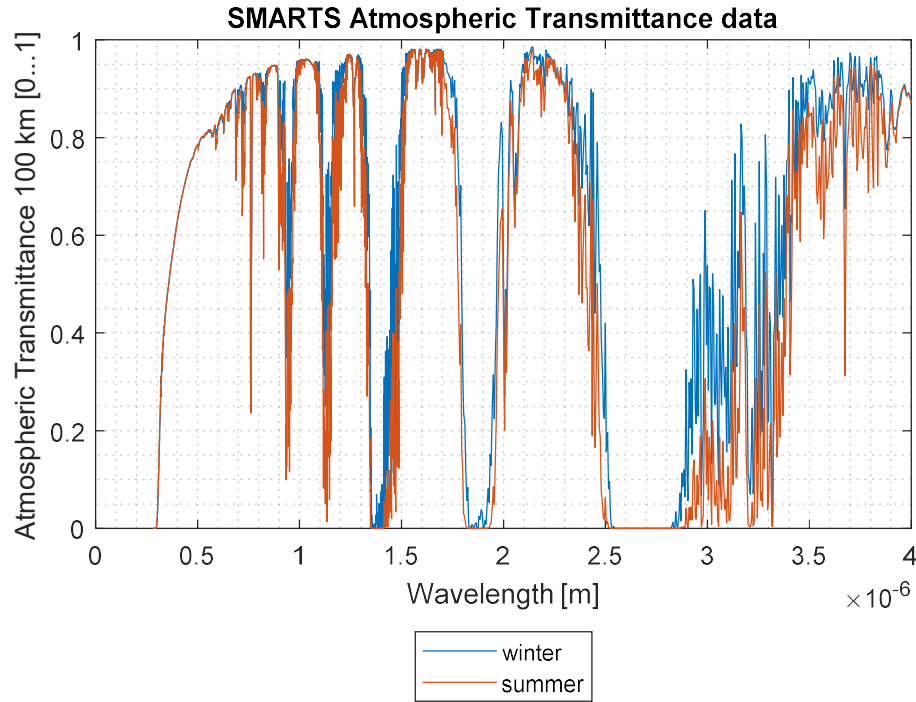


Figure 31 - Geometrical specification of the MODTRAN atmospheric sensor [29].

While the MODTRAN Online Software was used to generate the LWIR and MWIR Atmosphere Database the SMARTS Files were used to generated the SWIR Database, from 0.3 to 2.5 μm . SMARTS 2.9.2, which stands for Simple Model of the Atmospheric Radiative Transfer of Sunshine, is used to generate ASTM terrestrial reference spectra for ASTM Standard G-173-03 Standard Tables for Reference Solar Spectral Irradiances at AM1.5. This standard specifies the input parameters for computing reference spectra or a close approximation of historical reference spectra from 1987 to 2003 [28]. In the following diagram (Fig.32) the two databases are displayed. The first thing to notice is indeed the finer resolution that the SMARTS 2.9.2 has on the spectral range from 0.4-4 μm .





b)

Figure 32 - Atmospheric Transmittance Dataset. a) it shows the MWIR and LWIR database taken from ModTran Online Software. b) it shows the SWIR database taken from code SMARTS files. Note: in order to highlight the correlation between the two graphs b) is basically displayed as a zoom from the a) graph but still it is based on a different data source

3) Atmospheric Data Field: SpectralCalc Online Software [33].

SpectralCalc.com is a tool developed by GATS, which is a small aerospace company that provides instrument development, flight operations, retrieval algorithms and data processing/management systems for NASA atmospheric remote sensing missions [32]. In the following Table 5 the boundary conditions of this dataset are displayed.

Table 5 - Specifications for the dataset regarding the atmosphere present in the field [33].

Atmospheric Data Field Specification	
Observer height	0 km
Path length	Variable (1-500m)
Path direction	Horizontal
Line List	HITRAN2016
Model Atmosphere	MidLatSummer / MidLatWinter
Gases	H ₂ O, CO ₂ , O ₃ ; all isotopologues

A clarification note needs to be added, *Atmospheric Data Field* is referred to path2 and path3, while for path1 *Atmospheric Data* was used. Given the high amount of atmospheric transmittance data, additional graphs are available in the digital appendix of this thesis.

4) Mirror Reflectance: laboratory measurements

Measurement provided by CNRS-PROMES laboratory in France [34] for a mirror at Themis power plant for the MWIR and the LWIR ranges while for the SWIR range the measurement was made by OMT Solutions BV based in the Netherlands [35]. In the following graph (Fig.33), typical mirror reflectance data is shown.

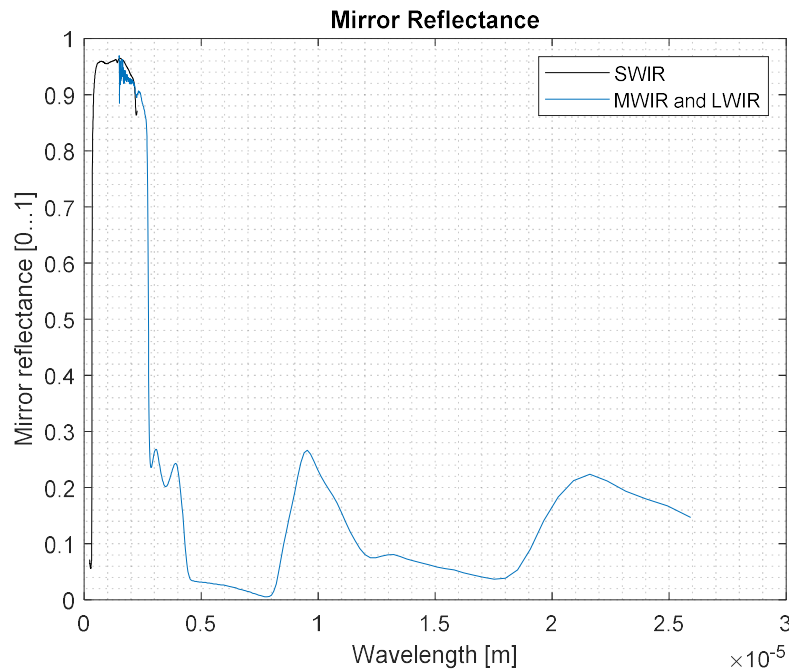


Figure 33 - Mirror Reflectance dataset graph

5) Materials Data: [36].

The materials chosen as coating for the receiver were mainly from two different categories, the first one was the Haynes 230 superalloy. It is a nickel-chromium-tungsten-molybdenum alloy that combines excellent high temperature strength with outstanding resistance to oxidizing environments up to 1149°C. In the following Table 6 is shown the nominal composition [37].

Table 6 - Nominal Composition of Haynes 230, percentage expressed in weight for weight ratio [37].

Name	Symbol	%
Nickel	Ni	57
Chromium	Cr	22
Tungsten	W	14
Molybdenum	Mo	2
Iron	Fe	3
Cobalt	Co	5
Manganese	Mn	0.5
Silicon	Si	0.4
Niobium	Nb	0.5
Aluminum	Al	0.3
Titanium	Ti	0.1
Carbon	C	0.1
Lanthanum	La	0.002
Boron	B	0.015

On the other hand, Pyromark 2500 is a silicone-based coating that is specifically formulated for metal surfaces that will be exposed to high temperatures (1370 °C as the manufacturer claims). The formulation used in the production process can be found in the following Table 7 [38].

Table 7 - Mixture Composition of Pyromark 2500, percentage expressed in weight for weight ratio [38].

Name	%
tert-Butylbenzene	15.41 - 21.57
Xylene	16.46
1,4-diethylbenzene	3.08 - 9.25
Ethylbenzene	5.02
Toluene	3.16
1,2,3-trimethylbenzene	1.54 - 3.08
Indan	0.31 - 1.54
1,2,3,5-tetramethylbenzene	0.31 - 1.54
m-diethylbenzene	0.31 - 1.54
Naphthalene	0.03 - 0.31
Zinc Octoate	0.14

The optical characterization for these materials were carried at the joint CIEMAT-DLR OPAC laboratory on the Plataforma Solar de Almeria in Spain [39]. For every material, four different samples were prepared with one of them kept as a reference (pristine). The three other samples were then respectively exposed to 700, 750 and 800 °C for 1000 hours. These samples did undergo the same optical characterization before and after testing, the latter was done to precisely measure the spectral hemispherical reflectance (SHR). It was measured at room temperature, for a wavelength range between 0.28 and 16 µm, at a near normal incidence angle with two spectrophotometers. The first measurement was conducted with the Perkin Elmer Lambda1050 spectrophotometer from 0.28 to 2.5 µm in steps of 5 nm with an incidence angle of 8°. This SHR measurement was extended from 2.5 to 16 µm in steps of 4 nm with a Fourier Transform Infrared (FTIR) spectrophotometer (Perkin Elmer Frontier FT-IR), the incidence angle in this case was 12° [36]. For this second round of analysis, the SHR measurement was firstly used to calculate the sample weighted SHR using the following equation (Eq. 20):

$$\rho_{SHR\ sample}(\lambda) = \frac{R_{sample}(\lambda)}{R_{baseline}(\lambda)} \rho_{baseline}(\lambda) \quad Eq. 20$$

Where

- λ is the wavelength expressed in nm or µm
- $\rho_{SHR\ sample}$ [%] is the sample weighted SHR
- $R_{sample}(\lambda)$ [%] is the SHR measurement data obtained for the sample
- $R_{baseline}(\lambda)$ [%] is the SHR measurement data obtained for the selected baseline
- $\rho_{baseline}(\lambda)$ [%] is the reference SHR for the selected baseline, calibrated by an external laboratory

The so calculated sample weighted SHR was then used to calculate the thermal emissivity of the samples. The equation used it the following equation (Eq.21):

$$\varepsilon_{th} = \frac{\int_{\lambda_1}^{\lambda_2} [1 - \rho_{SHR\ sample}(\lambda)] E_{bb}(\lambda, T) d\lambda}{\int_{\lambda_1}^{\lambda_2} E_{bb}(\lambda, T) d\lambda} \quad Eq. 21$$

Where ε_{th} is the thermal emissivity while all the other variables are already known from previous equation (Eq. 12 and Eq. 19). Example of spectral data are shown for a 750°C cured samples in Fig.34 while the rest of the spectral data for aged samples and pristine ones is shown in the appendix.

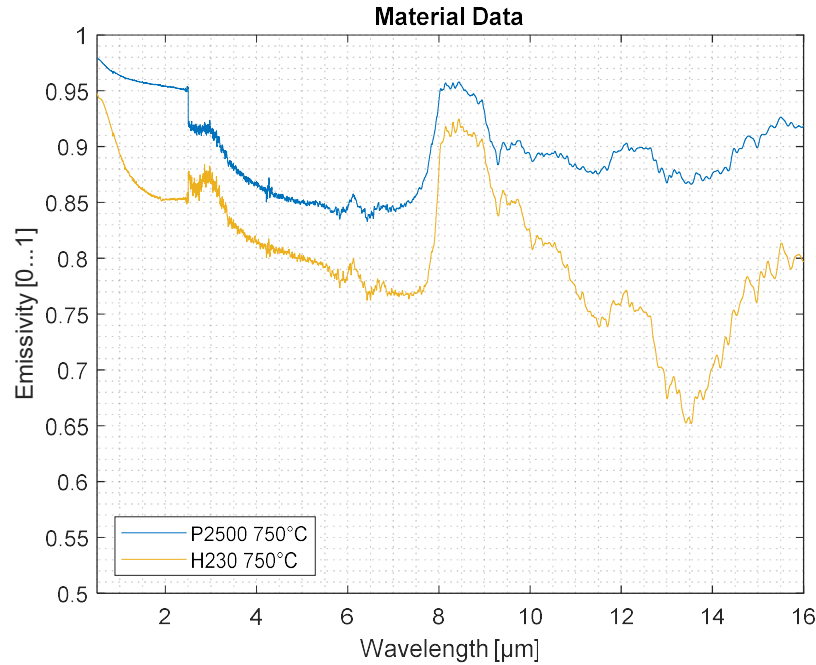


Figure 34 - Material data for two different samples: Pyromark 2500 and Haynes both cured at 750°C for 1000 hours.

6) Detector Data: obtained by e-mail exchanges with SWIR Vision Systems [40] and FLIR [41]. In the case of SWIR Vision Systems, they provide us the data relative to the Acuros® CQD® 640 GigE eSWIR Camera. In this respect the photodetector is based on the colloidal quantum dot infrared photodetector technology (CQDIP). CQDs are semiconductor nanoparticles suspended in the solution phase. Thanks to their typical strong confinement two states are present into the quantum wells: a ground state and an excited state [42]. Fig.35 shows the working principles of this kind of photodetectors.

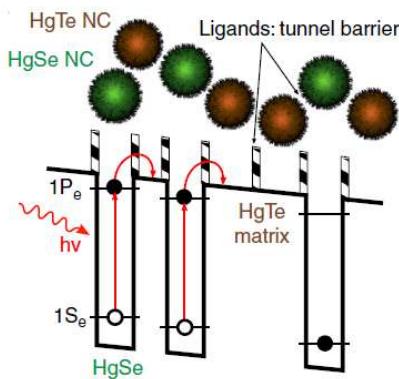


Figure 35 - CQDIP working principles, in the upper part the colloidal nanoparticles are displayed as illustration while in the bottom part a schematic representation explains the quantum wells principles behind [42].

FLIR provided us two different datasets for MWIR and LWIR, based on the Detector Response of two different high performance thermal imaging cameras in their portfolio, the FLIR A655sc and the FLIR SC5500 respectively. While for the LWIR range the detector used was indeed a microbolometer, which was largely described in the previous chapter, for the MWIR a photodetector based on mercury

cadmium telluride (HgCdTe)/ InSb was used. HgCdTe is a ternary semiconductor compound that exhibits a wavelength cutoff proportional to the alloy composition. The actual detector is composed of a thin layer (10 to 20 μm) of HgCdTe with contact pads defining the active area. Photons with energy greater than the semiconductor band-gap energy excite electrons into the conduction band, which will result in an increase of the material conductivity [43]. The detector geometry is displayed in the following illustration (Fig.36)

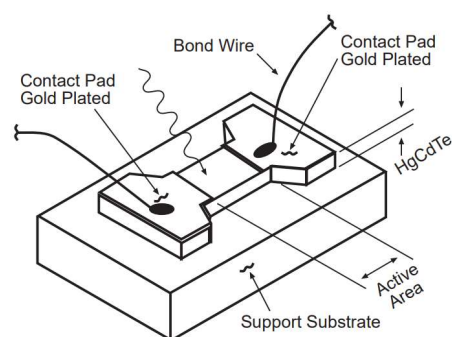


Figure 36 - HgCdTe photodetector geometry [43].

The following graphs (Fig.37) combines the three different detectors response data.

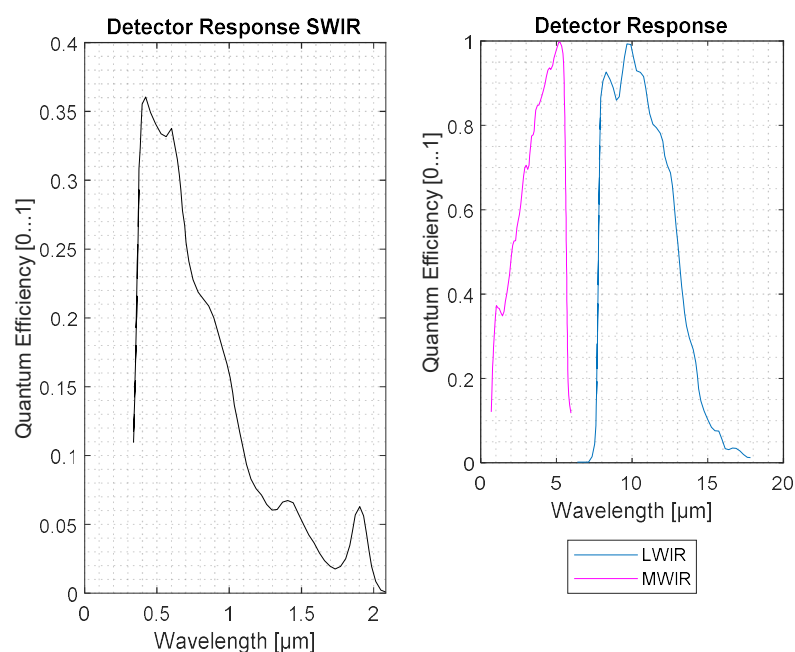


Figure 37 - Detector Database graph divided by range and source. a) SWIR dataset provided by SWIR Vision Systems. b) LWIR FLIR A655sc and MWIR FLIR SC5500 dataset provided by FLIR System

7) Filter Database: Spectrogon [44].

This dataset was given to us by Spectrogon AB, which is a manufacturer and developer of optical filters. The following Table 8 shown the filters provided by the company with the relative technical data.

Table 8 - Filter Database sorting by wavelength from SWIR to LWIR. CWL stands for central wavelength. HW stands for half width. τ_{peak} stands for tau peak can be a value between [0....1] and it's the highest value of tau that the filter reaches, it coincides with the peak of the function [44].

Range	Name	CWL [μm]	HW [0....1]	τ_{peak} [0....1]
SWIR	1370	1.370	0.009	0.6753
	1386	1.390	0.010	0.7152
	1394	1.393	0.010	0.7245
	1850	1.848	0.010	0.7524
	1912	1.910	0.011	0.7378
	1928	1.930	0.011	0.7110
MWIR	4510	4.515	0.190	0.9093
	4560	4.567	0.130	0.8294
	4630-180	4.621	0.171	0.8298
	4630-220	4.620	0.220	0.9005
	4665	4.647	0.212	0.8739
	4672	4.672	0.132	0.8443
	4725	4.723	0.133	0.8367
LWIR	8248	8.290	0.446	0.8848
	8645	8.630	0.544	0.9004
	8900	8.864	0.478	0.8859
	9127	9.132	0.491	0.9087
	9480	9.508	0.583	0.9169
	10400	10.448	0.681	0.8823
	10500	10.564	0.786	0.9144
	10760	10.773	0.700	0.9061
	11030	11.003	0.679	0.8786
	11660	11.646	0.723	0.8866
	12227	12.235	0.938	0.8922
	12840	12.839	0.819	0.8340

A remark needs to be added for the MWIR range, in fact there are two filter with the same CWL: 4630-180 and 4630-220. The notation to differentiate the pair is based on the second number which is referred to the HW of both filters. In addition to the data reported above, Spectrogon provided us only the graphic diagrams of the filter transmittance (τ) as a function of the wavelength (λ) without any other specific values. In order to implement properly the filter database we had two options, the first one was to use a Gaussian model based on the following function (Eq.22) to calculate the filter curve $F_{gauss}(\lambda)$

$$F_{gauss}(\lambda) = e^{-\left(\frac{\lambda - CWL}{\sqrt{2}HW}\right)^2} \quad \text{Eq.22}$$

This equation would allow us to recreate the filter characteristics using the CWL and HW given by the filter datasheet. On the other hand, the second option would require the use of an external software to extrapolate the x vs y values from the graphs. The strategy then was to use the WebPlot Digitizer

online website [45] in order to upload the picture of the graph and from it correlate the x and y points as it is shown in the template below (Fig.38).

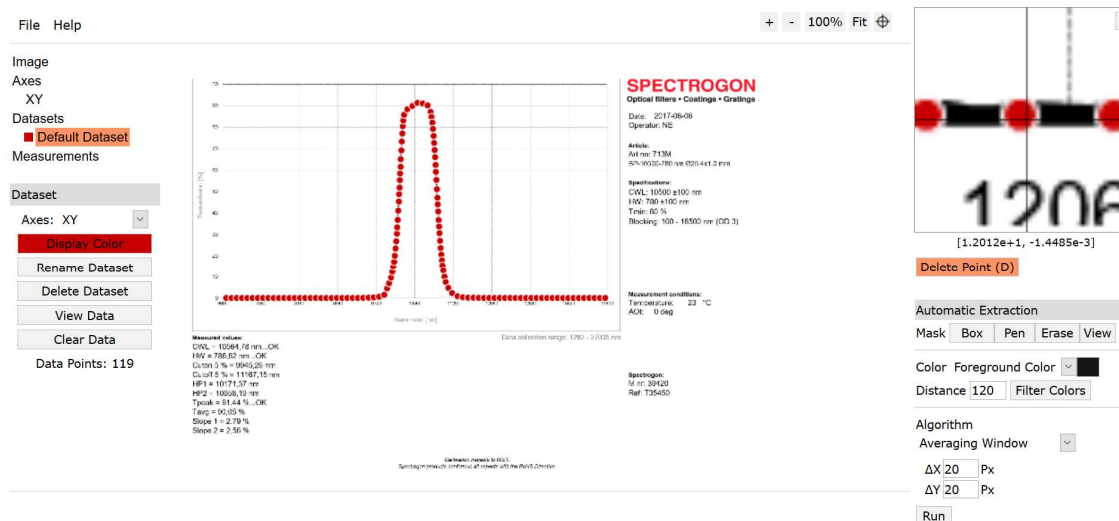


Figure 38 - WebPlot Digitizer template used to extract filter's transmittance vs wavelength. On the left side: image upload and axes selection (done manually). In the center: PDF image of the graph into analysis and point selection on the curve. On the right side: point adjustment and data extraction [45].

The parameters on the right side of the pictures dictate the extraction method of the x and y values, in this case we use the color highlight to separate the graphs line from the background then we used the mask box, which is a tool that is able to recognize with an algorithm a specific color, to obtain the red dots which are the x y pair values. We corrected the noise manually by removing the excess dots and then we export the values obtained in a .csv file in order to be readable in MatLab®. To evaluate if the filter curves could have been better approximate with Gaussian function or with the WebPlot Digitizer solution we compare the two curves obtained from the interpolation of the data and from the generation of the Gaussian curve respectively, then we calculate the offset between them. We run this test for all the filter mentioned in Table 8, which are available for consultation in the digital appendix of this work. In the following pictures it is possible to observe an example of the output of this analysis, in specific for the 9480 NB filter (Fig.39).

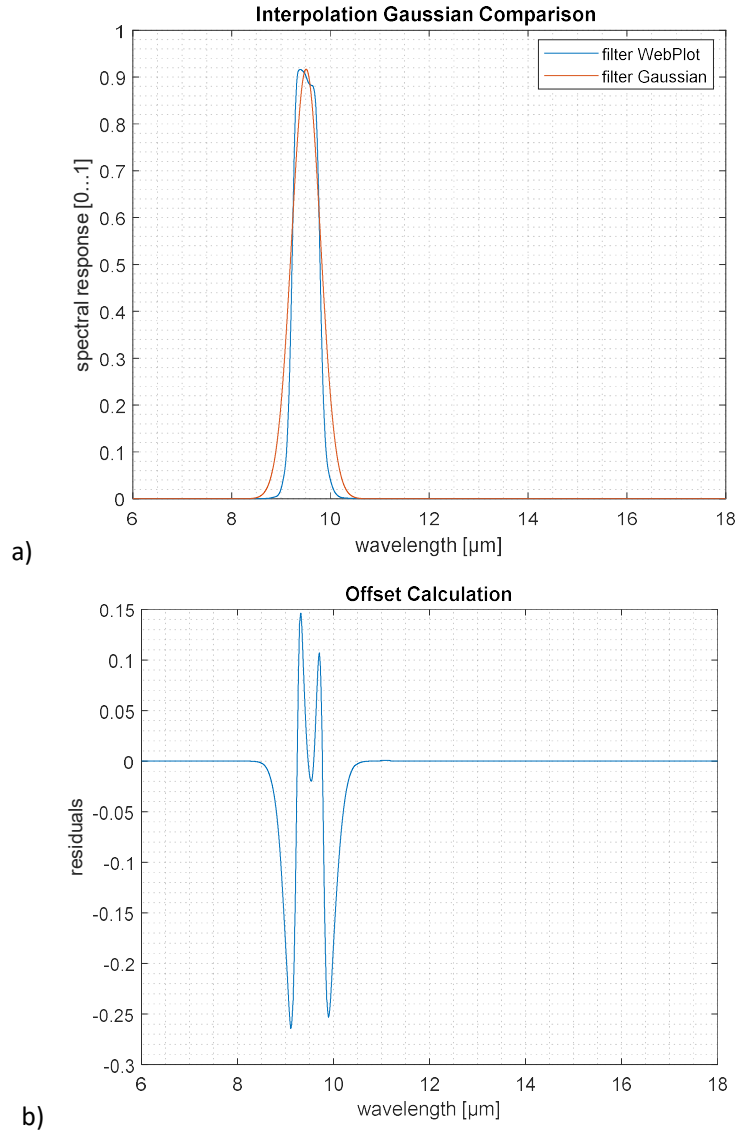


Figure 39 - Visual representation of the WebPlot Digitizer vs Gaussian model comparison for the 9480 NB filter. a) Overlap of the two filters curve obtained with the two methods. b) Offset calculation within the two curves shown in a).

From the graphs above it is visible how the gaussian curves is not matching the shape of the interpolated curve, not only in the lower part of the curve but especially near to peak. This is due to the high fluctuation of the real filter data in this region and the fact that the filter curve usually does not have a symmetrical contour, which the gaussian does. Considering the outcome in terms of errors, we decide that for our error standards the solution with higher accuracy is indeed the interpolation using the WebPlot Digitizer data extraction, however a higher detailed explanation about the filter calibration will be discussed in the next chapter.

3.4 First Layer

Going back to the Functions model map (Fig.28) the first level encloses the basic variables used as an input for most of the functions, the following list summarize them:

- Wavelength Vector [μm]
- Season either "Summer" or "Winter" according to the database
- Atmospheric Temperature [K]
- Object Temperature [K]
- Emissivity [0...1]
- Concentration Factor
- Distance Path [m]
- Range "SWIR", "MWIR" or "LWIR"
- Chip Temperature [K] is the temperature of the detector chosen
- Material selected as "Pyromark" or "Haynes"
- Treatment "yes" or "no" if the sample has been cured or if it is pristine
- Spec is the specification of the treatment, for the cured sample is the temperature
- Filter Name and related to this also the filter specification such CWL, HW and tau peak

These sets of variables are embedded into the code in terms of fields defining the structure into analysis, as anticipated before at the beginning of this chapter. An example of a structure of this kind is represent in the following picture (Fig.40), which illustrates a possible winter scenario in the SWIR range over a wavelength vector from 1 μm to 2 μm and a blackbody at 200°C.

```
% Define the inputs
% wavelength vector define in [ $\mu\text{m}$ ]
ref.wvl_start_um=1; % start
ref.wvl_stop_um=2; % stop
% temperature in [C]
ref.Tbb=200; % object temperature
ref.Tatm=0.95; % atmosphere
temperature
% concentration factor
ref.cx_vec=1000;
% noise condition factor
ref.xi=1;
% define the season
ref.season= "winter"

% material data
ref.material="Haynes";
ref.treatment="yes";
ref.spec=750;
% detector data
ref.Tchip=30;
ref.range="SWIR";
% distance for atmosphere data set
ref.d2=500; % distance path2
ref.d3=50; % distance path3
% filter data
ref.CWL = 1.84798;
ref.HW = 0.01082;
ref.tau_peak = 0.7524;
ref.Filter= 1850;
```

Figure 40 - Example of a structure used in the code, the name of the structure is ref and the data contained as fields are represented by the variables in the previous list.

The structure specific for a particular scenario was then used as an input to code a Second Layer, which functions will be explained in details in the following paragraphs, the functions were created accordingly with the MatLab® Documentation [27] that states:

function [y1,...,yN] = myfun(x1,...,xM) declares a function named myfun that accepts inputs x1,...,xM and returns outputs y1,...,yN. This declaration statement must be the first executable line of the function.

3.5 Second Layer

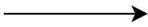




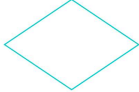
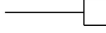
Before entering into a detailed explanation of the individual layout of each function, it is necessary to clarify a common MatLab® feature for all the loading functions. This aspect is the Spread Sheet import options or for abbreviation known as opts. In the following pictures is shown the example for the loading atm data function (Fig.41) [27].

```
% Season as data extract from excel tables can be either "winter" or "summer"
opts = delimitedTextImportOptions("NumVariables", 2);
% Specify range and delimiter
opts.DataLines = [1, Inf];
opts.Delimiter = ";";
% Specify column names and types
opts.VariableNames = ["wvl_um", "tau_percent"];
opts.VariableTypes = ["double", "double"];
% Specify file level properties
opts.ExtraColumnsRule = "ignore";
opts.EmptyLineRule = "read";
% Specify variable properties
opts = setvaropts(opts, ["wvl_um", "tau_percent"], "TrimNonNumeric", true);
opts = setvaropts(opts, ["wvl_um", "tau_percent"], "DecimalSeparator", ",");
opts = setvaropts(opts, ["wvl_um", "tau_percent"], "ThousandsSeparator", ".");
```

Figure 41- opts. Example for the loading atm data function

This command is used to import tabular data into MatLab®, in specific it locates a table in a file and returns its import options. With this tool it is also possible to modify the options object, for example adding additional parameters and used with the readtable command gives the possibility to control which data MatLab® imports [27]. Another common feature for this set of function is the 'pchip' interpolation, which stand for Piecewise Cubic Hermite Interpolating Polynomial (PCHIP), which is a standard MatLab® tool that allows the user to interpolate data with a high level of accuracy. The last point to be explained is the graphic scheme used in the flowchart, see Table 9 for the relative legend.

Table 9 - Flowchart design according to the ISO 5807 [46].

Shape	Name
	Flowline
	Input
	Output
	Process
	Predefined Process
	Decision
	Comment

Planck Law Function

This function uses as input the wavelength vector in μm and the blackbody temperature expressed in $^{\circ}\text{C}$, it gives back as output the blackbody Spectral Emittance $E_{\lambda, BB}(\lambda, T_{BB})$. The constants present in the Planck Law (Eq. 8) are already integrated into the code as the unit conversion. There is also a mesh grid step present in the code, this is done for the purpose of generating simultaneously more temperature related curves by using as input no more one specific temperature but instead a temperature vector, the following picture illustrates the function code (Fig.42).

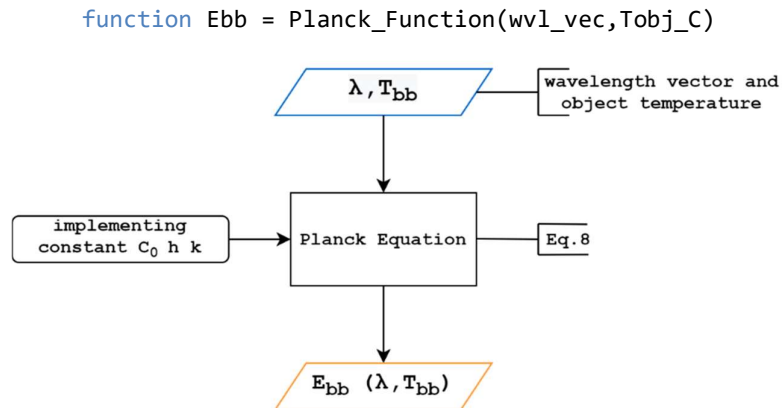


Figure 42 - Planck Law Live script

Gray Body Function

This function is based on the Planck Function script seen before with a few additional lines of code that integrated the emissivity of the material as new input into the calculation), in fact in this case the final output will be the Spectral Emittance of a gray body $E_{\lambda, BB}(\lambda, T_{BB}, \epsilon)$.

Load Solar Irradiance Data Function

This function, as the ones that will follow, is a loading function, in the sense that its main purpose is to load and interpolate a selected database. The input is the wavelength vector expressed in μm while the output is solar irradiance based on the ASTM E490 standard database described earlier in this chapter. The loading characteristic of this function is shown in Fig.43. The main purpose of this code is to properly read and import the data stored in an Excel sheet table into the MatLab® database. Once the table is imported into the program the function interpolates the data in order to be use into the model.

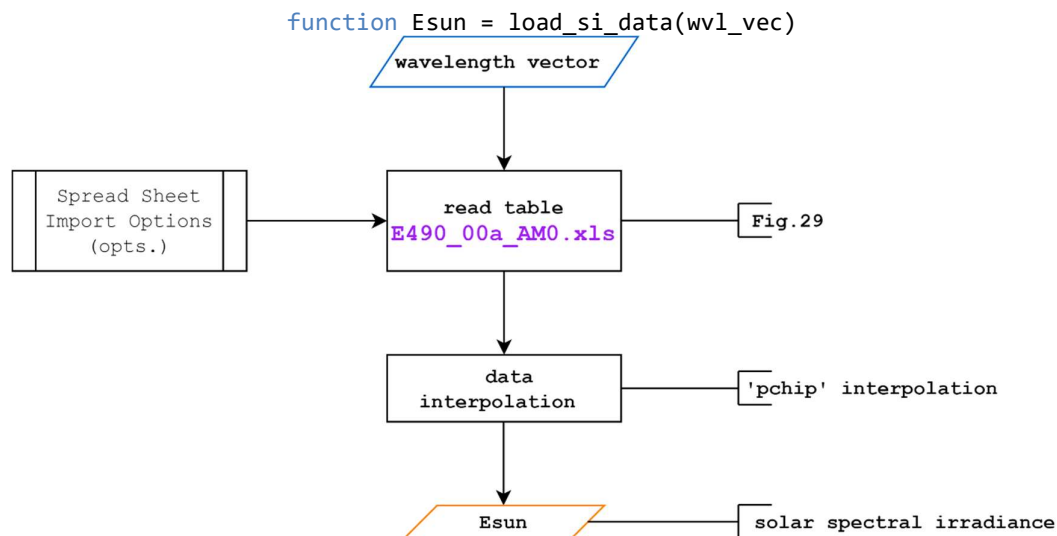


Figure 43 - Load Solar Irradiance data Live script

Load Atmospheric Data Function

Using the wavelength vector expressed in μm , the season and the range as an input this function output is the τ relative to the atmospheric transmittance. It is in the same categories of the function before with few similarities with it, however there is a considerable part of the code unique to this function due to the nature of its database. In fact, as it is illustrated in the following picture (Fig.44) the opts feature is used to read the Excel sheet properly then from this point onwards the code is set to give a selection choice to the user. In specific there is an if switch case scenario. The first level using the if elseif function is the selection of the season with either summer or winter. The second level is the choice of the range chosen, using a switch case function it is possible to chose the three different range SWIR,MWIR and LWIR.

```
function tau = load_atm_data(wvl_vec,Season,range)
```

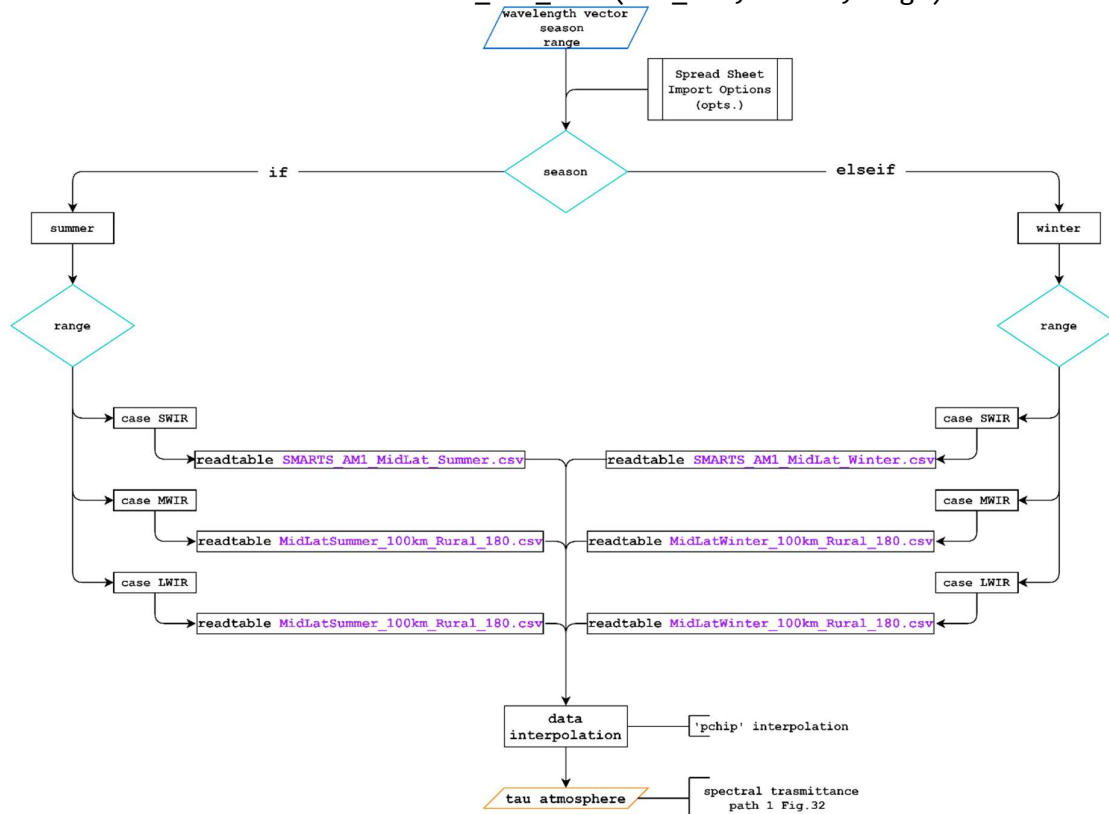


Figure 44 - Load Atmospheric Data script

Load Atmospheric Data Field Function

This function has as input the wavelength vector in μm , the season, the path distance in m and the atmospheric data. It will generate as output the τ referred to the atmosphere in the field. The data as input mentioned before is an external loading functionality set due to the dimension of the database in question, see Fig.45. The purpose for it is to have low computational time while running the functions. If it was embedded into the code of a loading atmospheric function it would have slow down the all process, while with a set up like this it will take maximum up to 10sec to have the database fully loaded into the system once.

```

1. % Load high resolution atmospheric database once (10 sec)
2. data.Winter=load('D:MidLatWinter_horz_light_version.mat');
3. data.Summer=load('D:MidLatSummer_horz_light_version.mat');

```

Figure 45 - Data pre-loading script

The “Load Atmospheric Data Field” function, as shown in the picture below (Fig.46), is based on the if switch case scenario as well. In this particular occurrence however, once the season is chosen the next entry is the distance path, in accordance to where the camera is positioned on the field. The code is able to upload various possible configuraton from 1 to 500m, the entry values are fixed and for everyone of them the corrisponding dataset will be upload and then interpolated to made the data useable for the simulation analysis.

```
function tau = load_atm_data_field(wvl_vec,Season,dist,data)
```

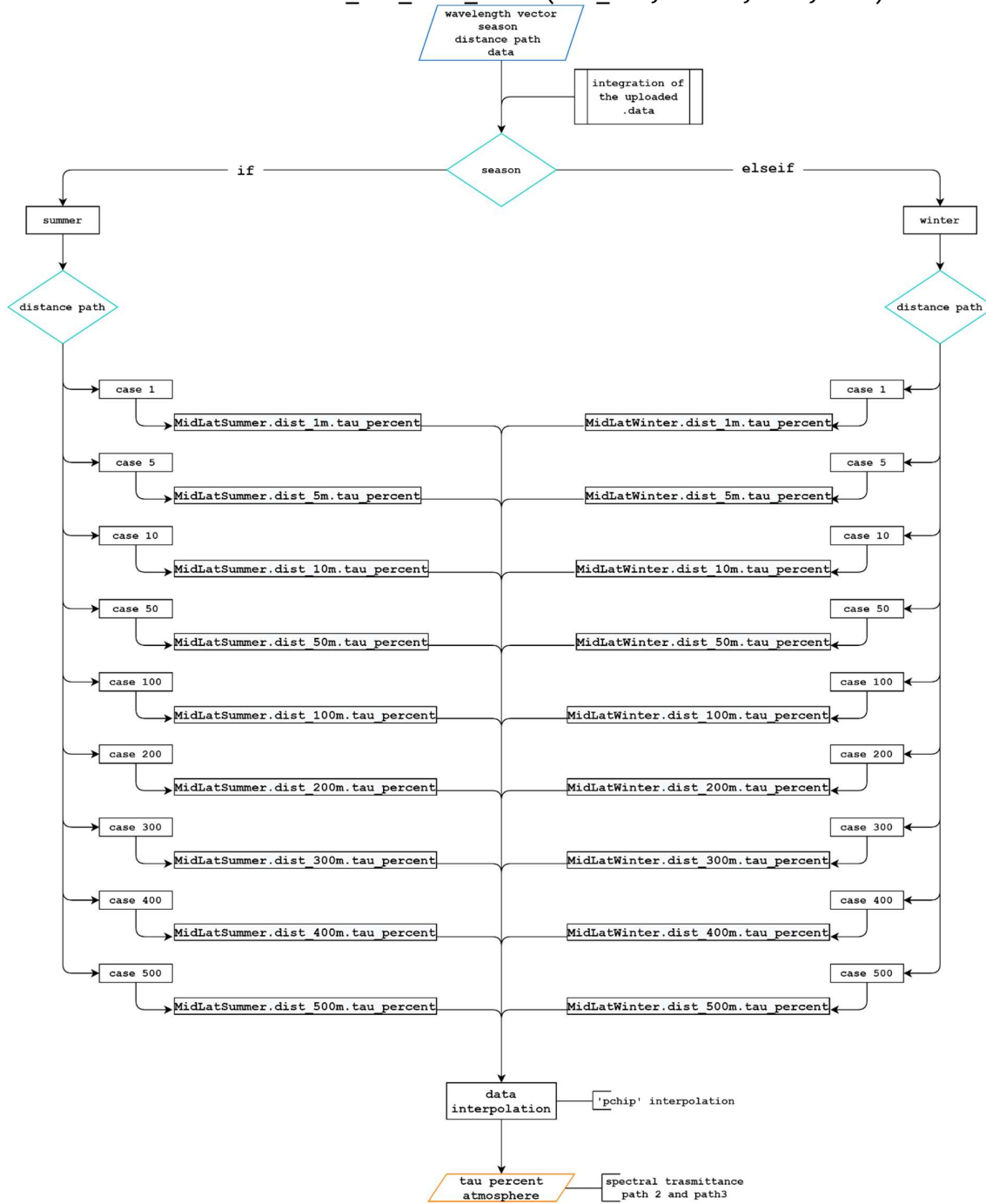


Figure 46 - Load Atmospheric Data Field script

Load Mirror Data Function

This function uses the wavelength vector expressed in μm and the range as input to giving back to the user the mirror reflectance interpolated data, see Fig.33. The code of this function as the ones before is also structured with the `opts` (Fig.41). to load correctly the Excel sheets with the dataset and a `switch case` to be able to chose the different range under examination, in the following picture the script is highlighted (Fig.47).

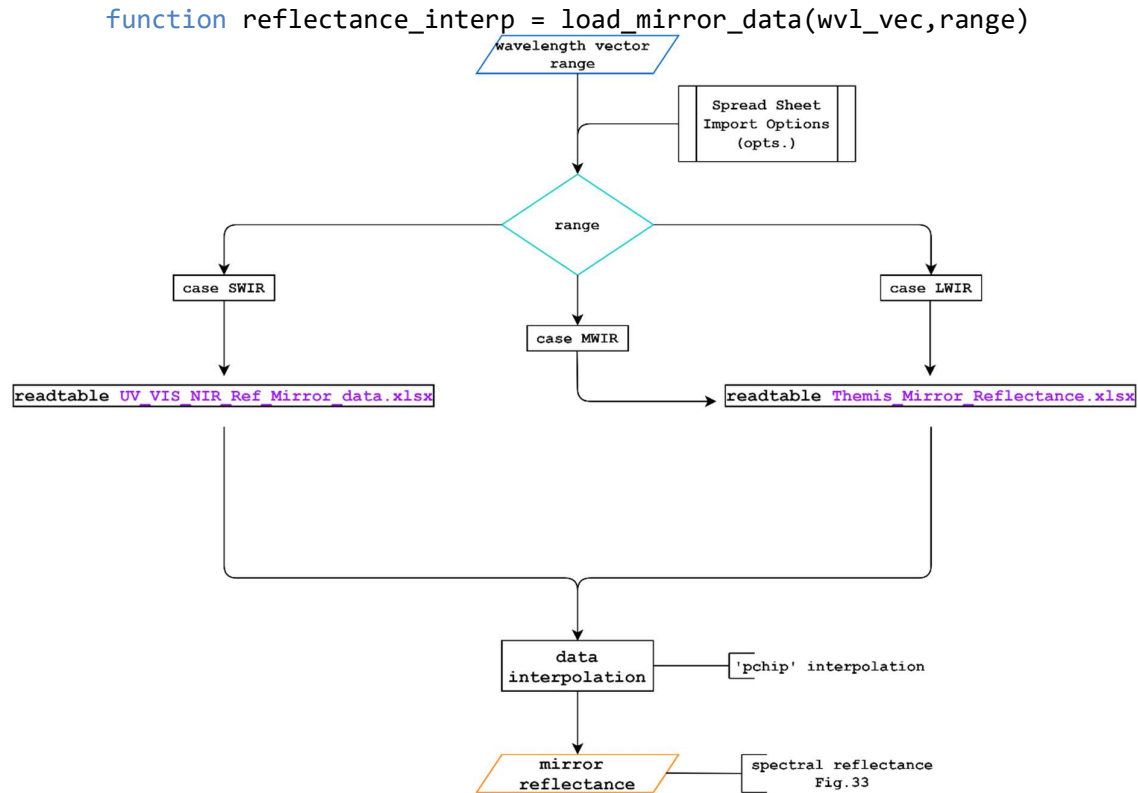


Figure 47 - Load Mirror Data script

Load Material Data Function

This function has high structure similarities with the ones before with the `opts`. to decode the Excel sheets and the `if switch case` scenario, however the latter uses a specific input layering. In fact, for the correct upload of the material emissivity, which is the function output, the first entry is the material chosen either “Pyromark” or “Haynes” that will be process by the `if` function. Then for the `switch case` the two different options are “yes” or “no” in case the material underwent a treatment or not and afterwards either the temperature of the treatment or the specification for the pristine material chosen as A, B, C or D. This latter is due to four different datasets available for the pristine materials. The following picture illustrates this function (Fig.48).

Load Filter Data Function

The loading function for the filters uses the name of the filter (Table 8) as input and it gives back as output the x axe data as wavelength (λ) and the y axe as tau data (τ). This function has also a `switch case` scenario architecture and in this one in particular the name of the filter will direct the function to load a specific Excel sheet, making it easier to process and integrate into the next functions layer. The picture below shows the function script (Fig.49).

```
function material_data = load_material_data(input)
```

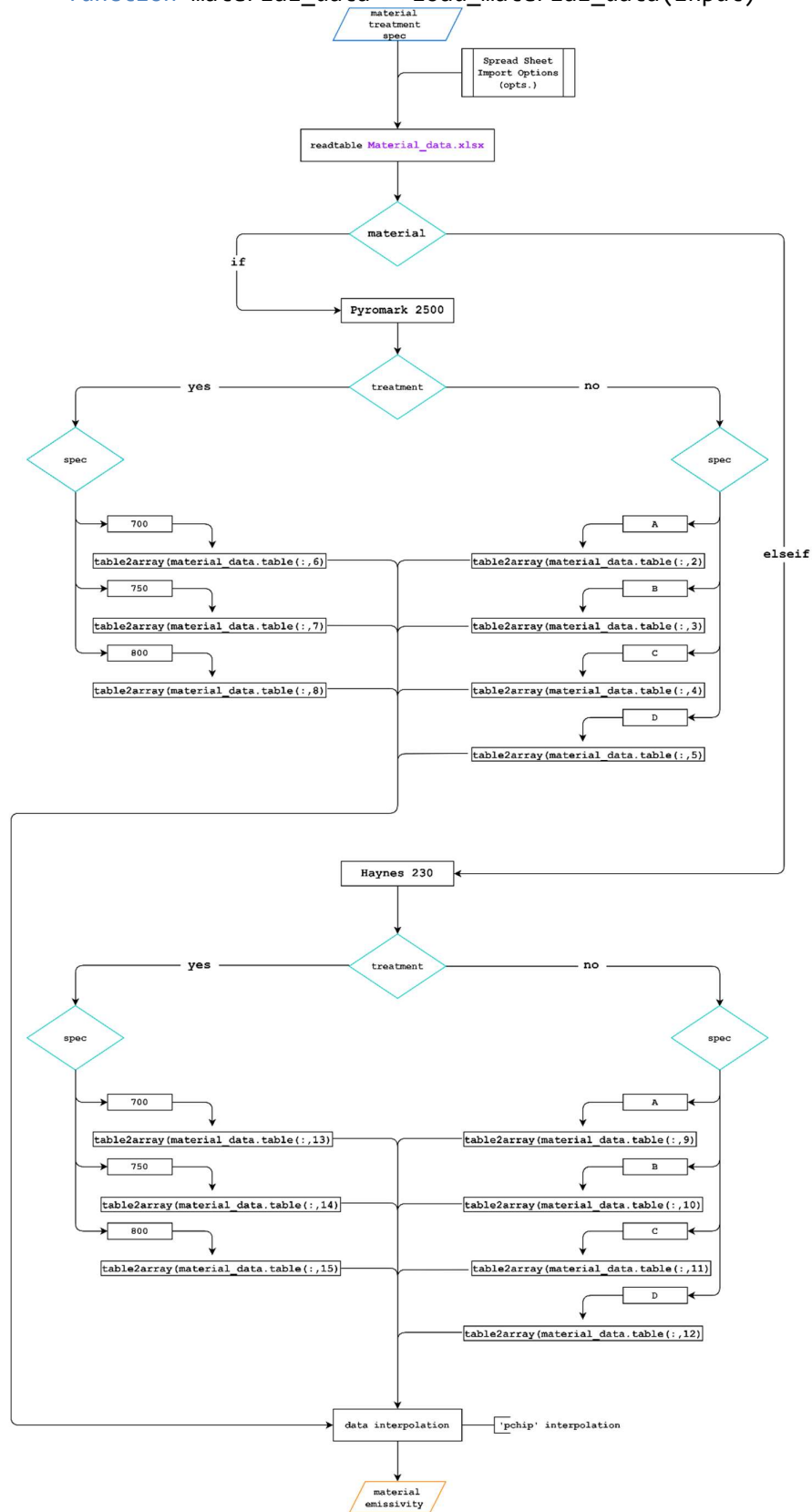


Figure 48 - Load Material Data script

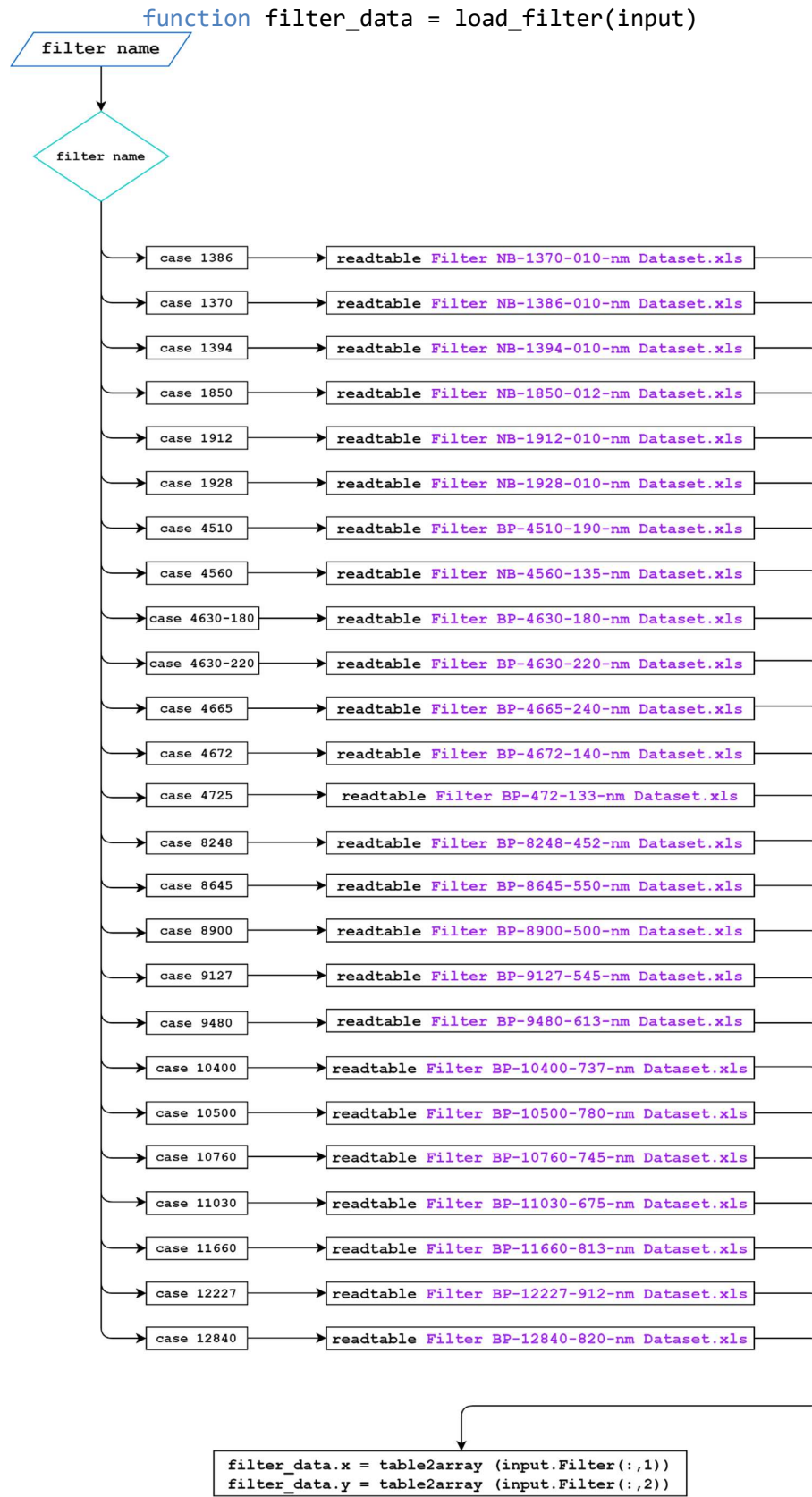


Figure 49 - Load Filter Data script

Load Detector Data Function

This function is the last one in the set of the loading function and it is the one responsible for the detector dataset. Using as input the analysis range, the outcome is the detector response (see Fig.37). The switch case scenario in this function is used to select the range chosen (Fig.50).

```
function [detector_wvl, detector_response] = load_detector_data(range)
```

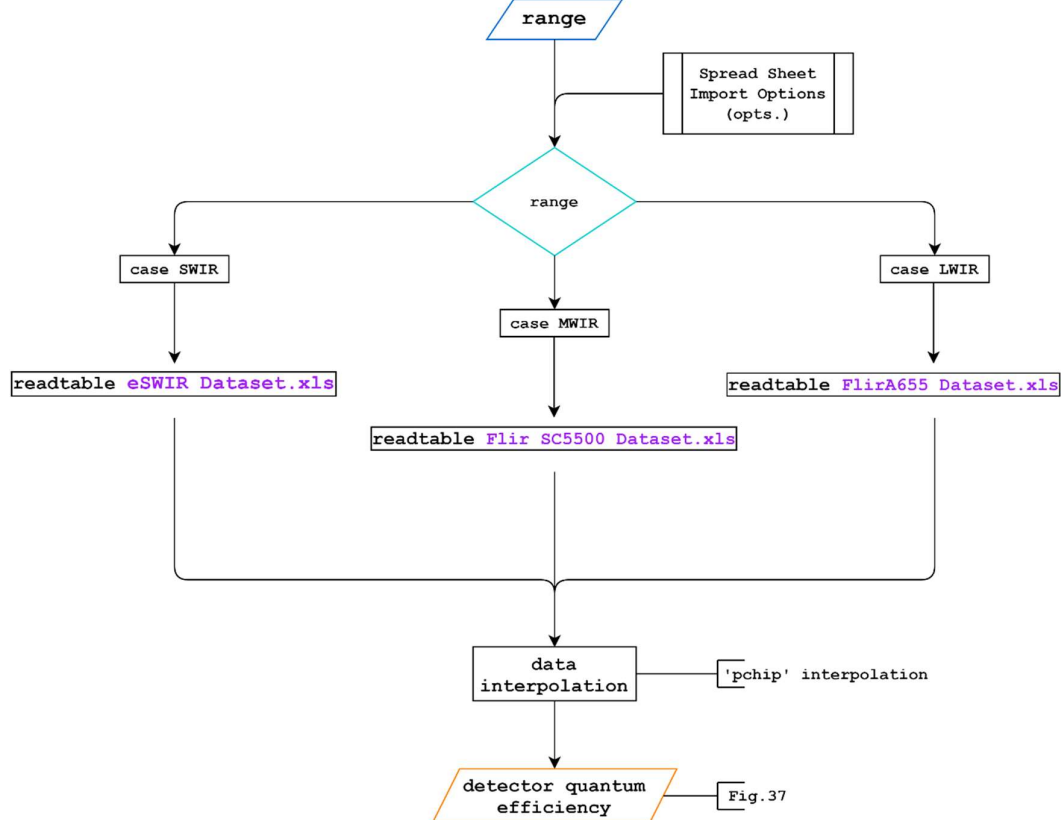


Figure 50 - Load Detector Data script

Reciprocal Planck Function

This function is basically the inverse of the Planck Function analyzed before with just a reverse input structure, so in this case the function will operate the calculations based on the Spectral Emittance of the body in consideration $E_{\lambda, BB}(\lambda, T_{BB})$ and the wavelength vector expressed in μm as input and it gives back the temperature of the body as outcome (Fig.51), in case this function is used to reverse calculate the temperature it means that the operating condition are monochromatic.

```
function T = Reciprocal_Planck_Function(Ebb,wvl_vec)
```

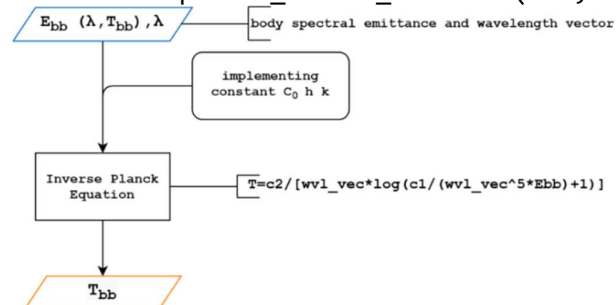


Figure 51 - Reciprocal Planck Function script

3.6 Third Layer

Even though there is no specific function for this layer, because the various terms are generated within the code of the functions of the 4th layer, this step is crucial because it combines all the loaded data from the 2nd layer into a combination of radiometric quantities. It is based entirely on the Eq. 19 and it is the digital reproduction of the radiometric chain shown in Fig.26 and Eq.19. The three different terms are the main feature of this layer, in specific they can be described as such:

- term 1: it represents the object radiation, the backbone for this term is the Planck function but there could be also correction regarding the filtering, detector response or materials emissivity parameters according to the scenario into analysis.
- term 2: it is the computation of the radiation from the sun which is influenced from various elements along the three paths such the mirrors, the atmosphere, the object itself but also the filter and detector. For these reasons, the function is based on the Planck function with corrections added on from the different databases. For this term, the conditions for the integration of the different variables also changed upon the scenario examined, for example in case of operating in solar blind conditions [47] term1 is predominant so this term can be considered equal to zero.
- term 3: it calculates the noise generated from the surrounding environment, like the other two based on the Planck function but with a major different from the previous terms, in this case the Planck function is integrated using the atmosphere temperature as input to better represent its contribution to the signal.

3.7 Fourth Layer

Signal Analysis Monochromatic Function

Once all the data set are loaded and the various functions have been debugged, the fourth layer combines the three different terms and it simulates the signal received by the camera. One of the functions that characterized the third layers is called Signal Analysis monochromatic, which script is shown as follows (Fig.52).

```
function [output] = Signal_Analysis_monochromatic(input,data)
```

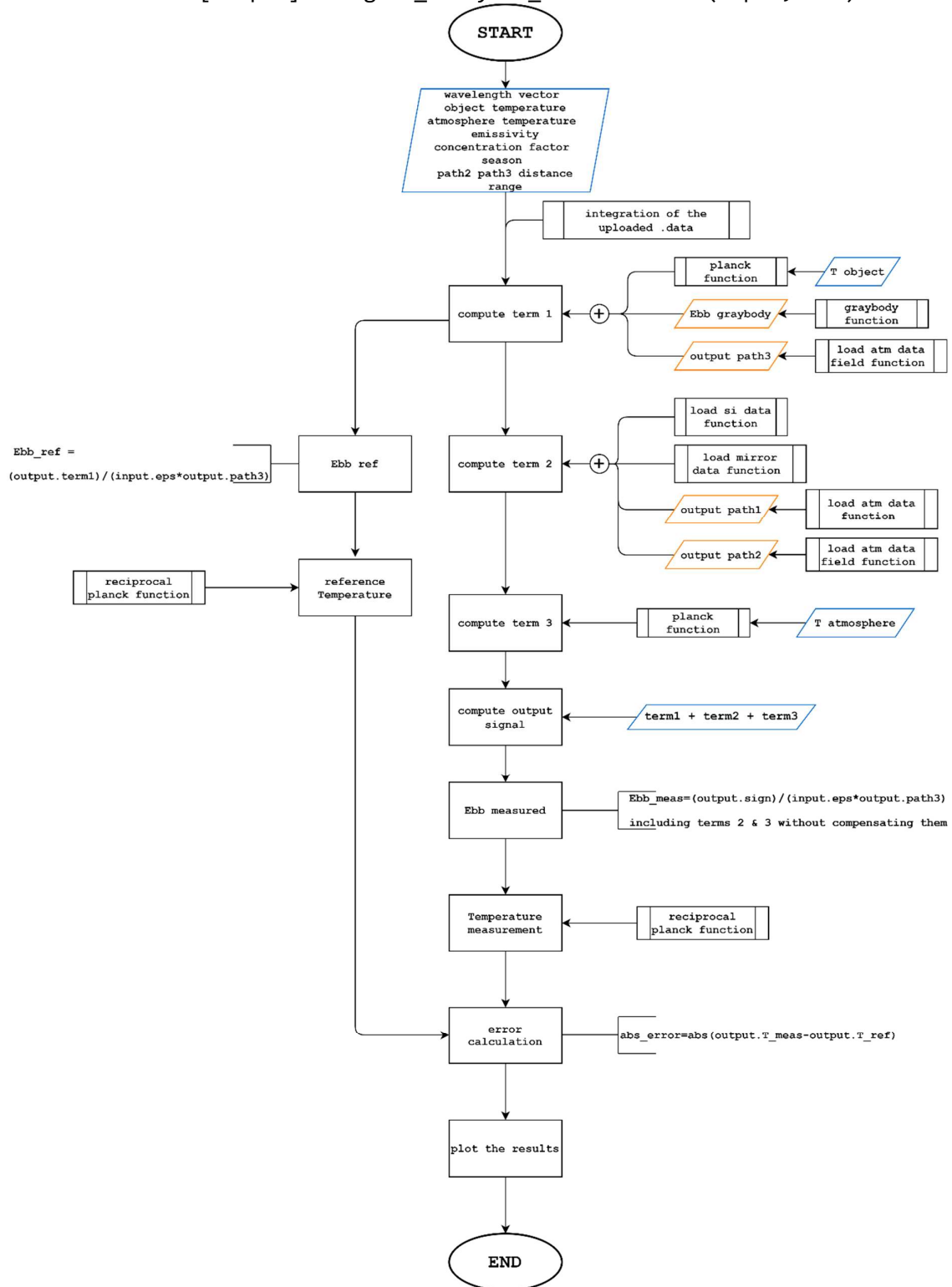


Figure 52 - Signal Analysis monochromatic script

This function was the first step in the direction of the complete model, it is however an early stage prototype that allowed us first to evaluate properly the contribution between the different terms of interested as an overview for further analysis. In the code there are no contributions of any specific materials, detector or filters and neither the range chosen.

Term 1 is defined by the gray body emittance and the interference of the atmosphere in the third path combined. Term 2 is calculated by first the loading and interpolation of the solar irradiance, the mirrors and the two atmospheric datasets, then secondly the correlation of the concentration factor and the graybody emissivity. Then term 3 is derived by the atmospheric transmittance of path 3 and the Planck function calculated using the atmospheric temperature as input.

After these calculations, the function evaluates the temperature based on the Planck Function, which will be used as a reference temperature in order to calculate the corresponding temperature error. The latter has been based on the different between the temperature detected, that is the one generated by the simulated signal, and the one from the Reciprocal Planck Function.

Signal Analysis Band Function

After the code was debugged it was then the time to update the current function, here we switch from a monochromatic analysis to a band analysis, for doing do it was necessary to change the lines of the codes regarding the temperature calculation. In fact, in the Signal Analysis band function the temperature is no longer dependent on a single wavelength, calculated using the Reciprocal Planck function, but instead on the band and for this reason as it is shown afterwards (Fig.53) the integral has been implemented into the calculation.

Model Analysis Function

The following step in the direction of a fully integrated simulation of the signal was the creation of the Model Analysis function (Fig.54). With this latter we implemented into the code the effect not only of the filter and the detector but also a more accurate representation of the material into analysis. In order to do so, there were few equations that needed to be integrated in the process steps to calculate properly the reference signal. These set of equations used to calculate the reference values for the band emittance $\bar{\epsilon}(T_{bb})$, the atmospheric band transmittance $\bar{\tau}_3$ and the band $\bar{\epsilon}\bar{\tau}_3$ product are described in the following list.

$$\bar{\epsilon}(T_{bb}) = \frac{\int_{\lambda_{start}}^{\lambda_{stop}} \epsilon(\lambda, T_{bb}) \cdot F_k(\lambda) \cdot R(\lambda) \cdot E_{bb}(\lambda, T_{bb}) d\lambda}{\int_{\lambda_{start}}^{\lambda_{stop}} F_k(\lambda) \cdot R(\lambda) \cdot E_{bb}(\lambda, T_{bb}) d\lambda} \quad Eq.23$$

$$\bar{\tau}_3 = \frac{\int_{\lambda_{start}}^{\lambda_{stop}} \tau_3(\lambda) \cdot F_k(\lambda) \cdot R(\lambda) \cdot E_{bb}(\lambda, T_{bb}) d\lambda}{\int_{\lambda_{start}}^{\lambda_{stop}} F_k(\lambda) \cdot R(\lambda) \cdot E_{bb}(\lambda, T_{bb}) d\lambda} \quad Eq.24$$

$$\bar{\epsilon}\bar{\tau}_3 = \frac{\int_{\lambda_{start}}^{\lambda_{stop}} \epsilon(\lambda, T_{bb}) \cdot \tau_3(\lambda) \cdot F_k(\lambda) \cdot R(\lambda) \cdot E_{bb}(\lambda, T_{bb}) d\lambda}{\int_{\lambda_{start}}^{\lambda_{stop}} F_k(\lambda) \cdot R(\lambda) \cdot E_{bb}(\lambda, T_{bb}) d\lambda} \quad Eq.25$$

The resulting signal generated from these equations was used as a reference signal in order to check the model in case of error. For this reason, in this function there is a calibration step, which only purpose is to correlate the two signals. Another feature of this function regarding the calibration process is the error calculation on the temperature shown in the last step, again this is used to validate the simulation obtained.

`function [output] = Signal_Analysis_band(input,data)`

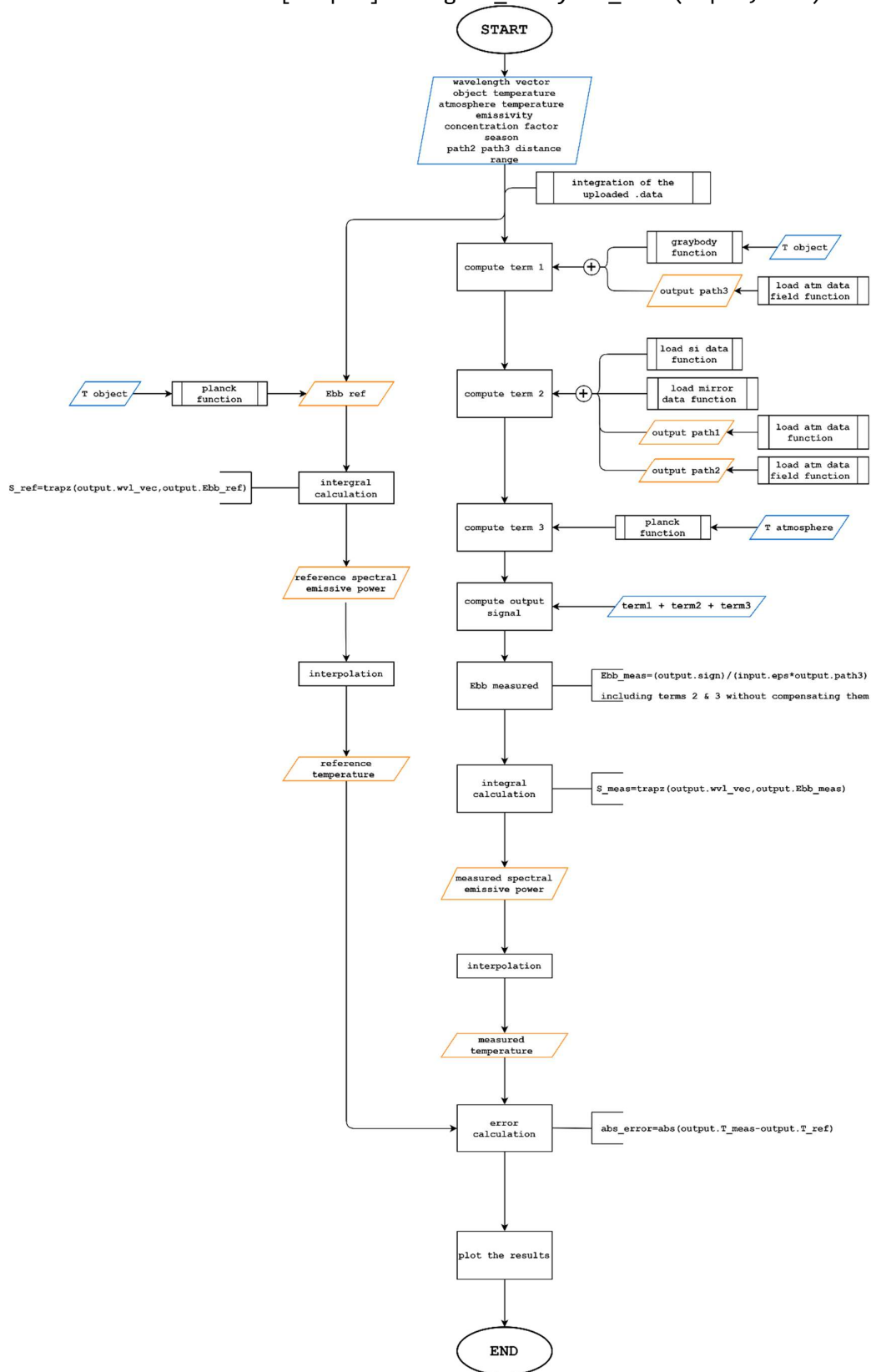


Figure 53 - Signal Analysis band script

```
function [output] = Model_Analysis (input,data)
```

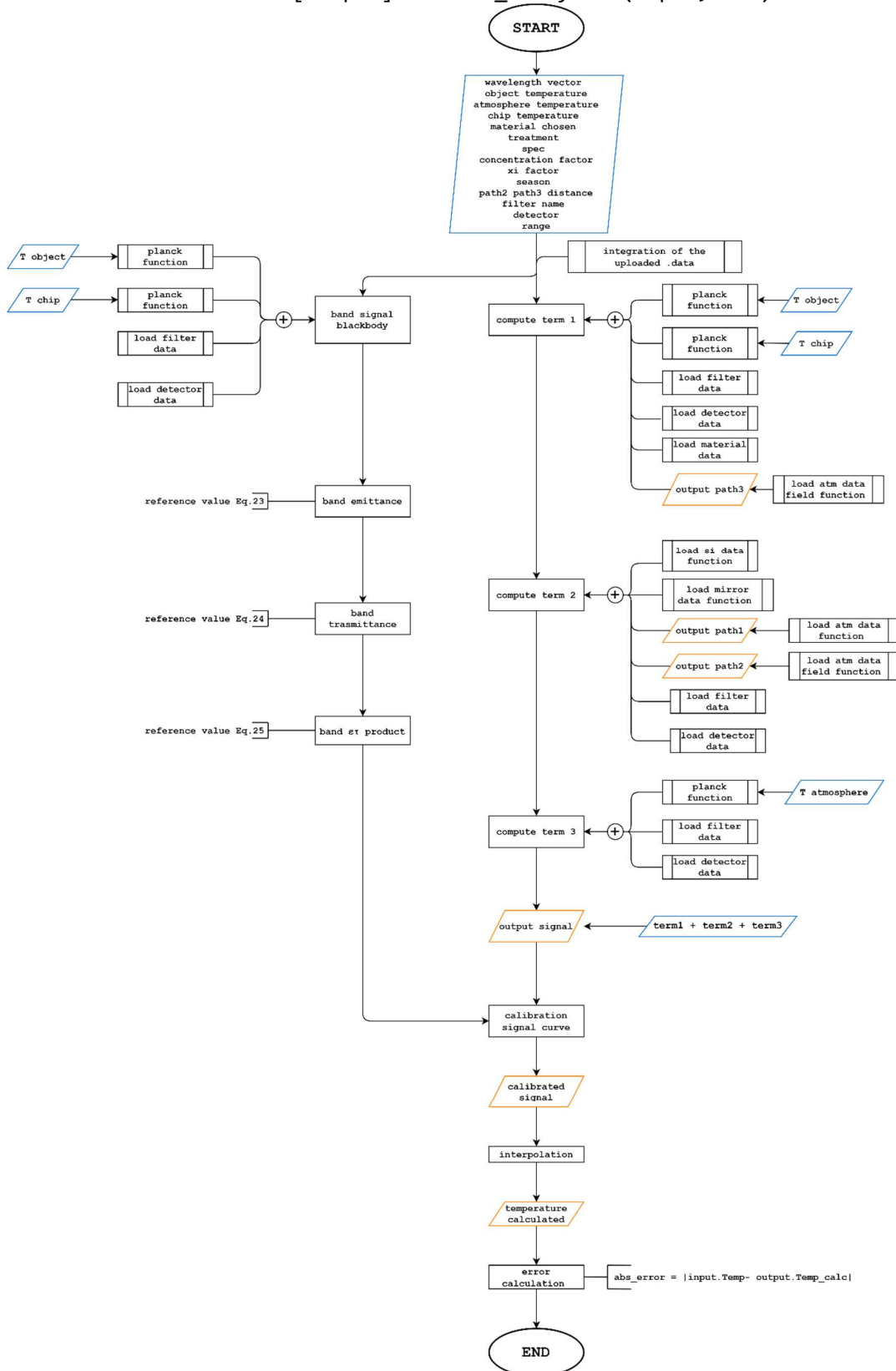


Figure 54 - Model Analysis script

RMSE Function

Before heading in a depth description of the use and the possibilities of the optimizer, there is indeed the require of introducing few other functions, which will be discussed in the following paragraphs. The first one is the RMSE function and as the name directly suggest it calculates the Root Mean Square Error of the input signals using the following equation (Eq.26).

$$RMSE = \sqrt{\sum_{k=1}^n \frac{[\tilde{S}_{filter}(\tilde{T}_{bb}) - S_{filter}(T_{bb})]^2}{n}} \quad Eq. 26$$

Where:

- $\tilde{S}_{filter}(\tilde{T}_{bb})$ is the estimated signal for optimization
- $S_{filter}(T_{bb})$ is the reference signal from the "simulated measurement"

Contour Map Function

The other Implemented function is called Contour Map, shown in the following pictures (Fig.55). The primary objective of this function is a wide error analysis of all the permutations generated, the latter refers to the testing of the Signal Analysis band function (Fig.53) in a variety of different conditions as it will be discussed in the next chapter. The full code can be divided into 3 major parts, the first one has the main purpose of generating the new scenarios by running multiple permutation.

Based on the Signal Analysis band function the second part of the code is used to compute all the scenarios, it uses the for function to analyzed them in loop with possibility of a single scenario analysis check in case of errors. Finally, the third part is collecting the outputs in a single matrix to generate the contour maps.

Calibration Function

Another function that was crucial in the process of creating a complete model was the Calibration function, which is based on the gaussian model (Eq.22). In the previous paragraph we addressed the issue regarding the filter database and the best way of implementing it by specifically choosing the interpolation model over the gaussian curve. For the purpose of calibration however we used the gaussian model to calculate the filter influence on the outcoming simulated signal. This was necessary to understand the dependence of the signal output on the filter specific factors such as CWL and HW. The Calibration function using the specification over CWL and HW calculates the integrated signal related to the temperature of the body (Fig.56). In this process the function calculates term 1, which aforementioned is the radiation from the object (Eq.19), as a combination of two different sub terms: termA and termB shown in Eq.27 and Eq.28 respectively.

$$termA = \tau_3(\lambda) * R(\lambda) * Ebb(\lambda, T_{bb}) \quad Eq.27$$

$$termB = [1 - \tau_3(\lambda)] * R(\lambda) * Ebb(\lambda, T_{chip}) \quad Eq.28$$

While termA is considered as the main radiation detected by the camera, termB is the offset. The overall outcome is then integrated and plotted as signal function of the temperature. For this set of calibrations, the body into question is considered a black body in a vacuum (no atmosphere) as the only interested for this function is the generic influence of the filter on the signal and not in the specific analysis of the material and the atmosphere. The results will be explained in the next chapter.

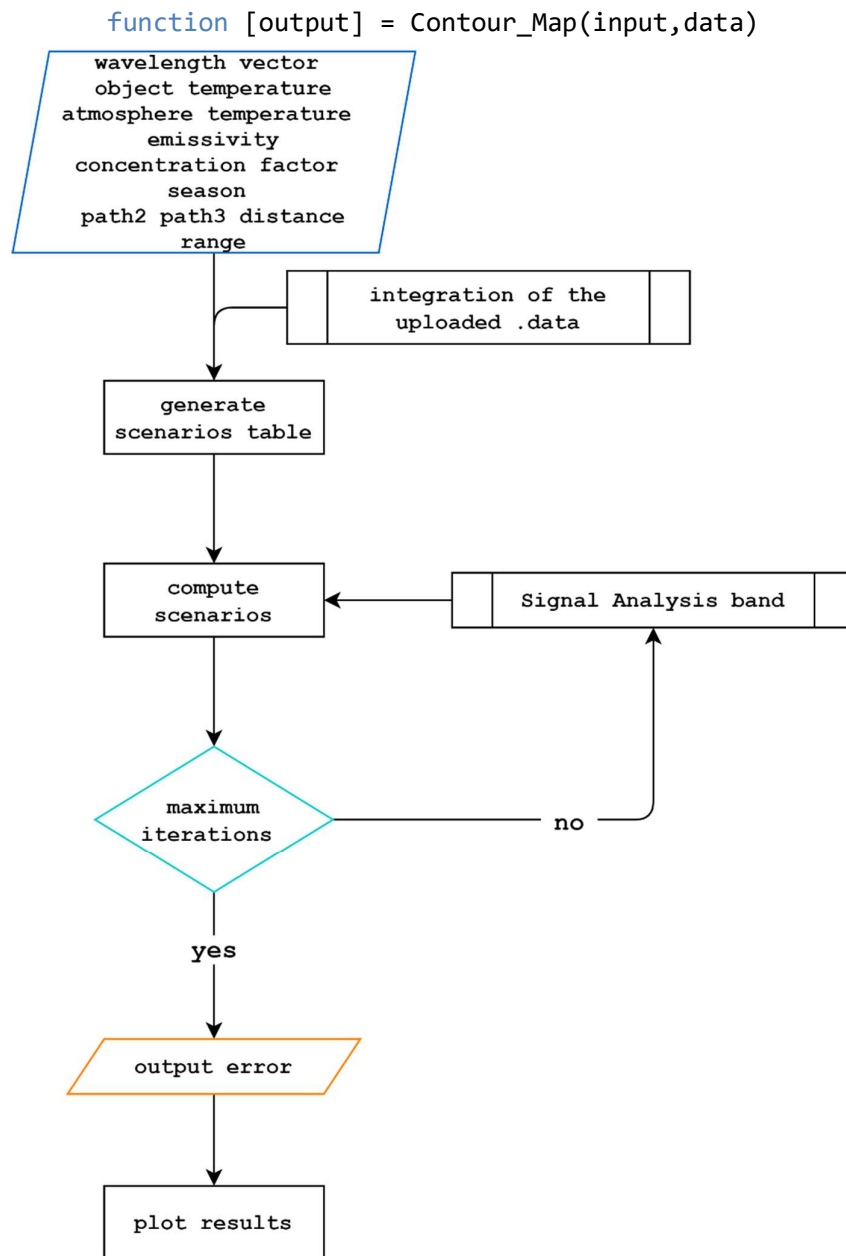


Figure 55 – Contour Map script

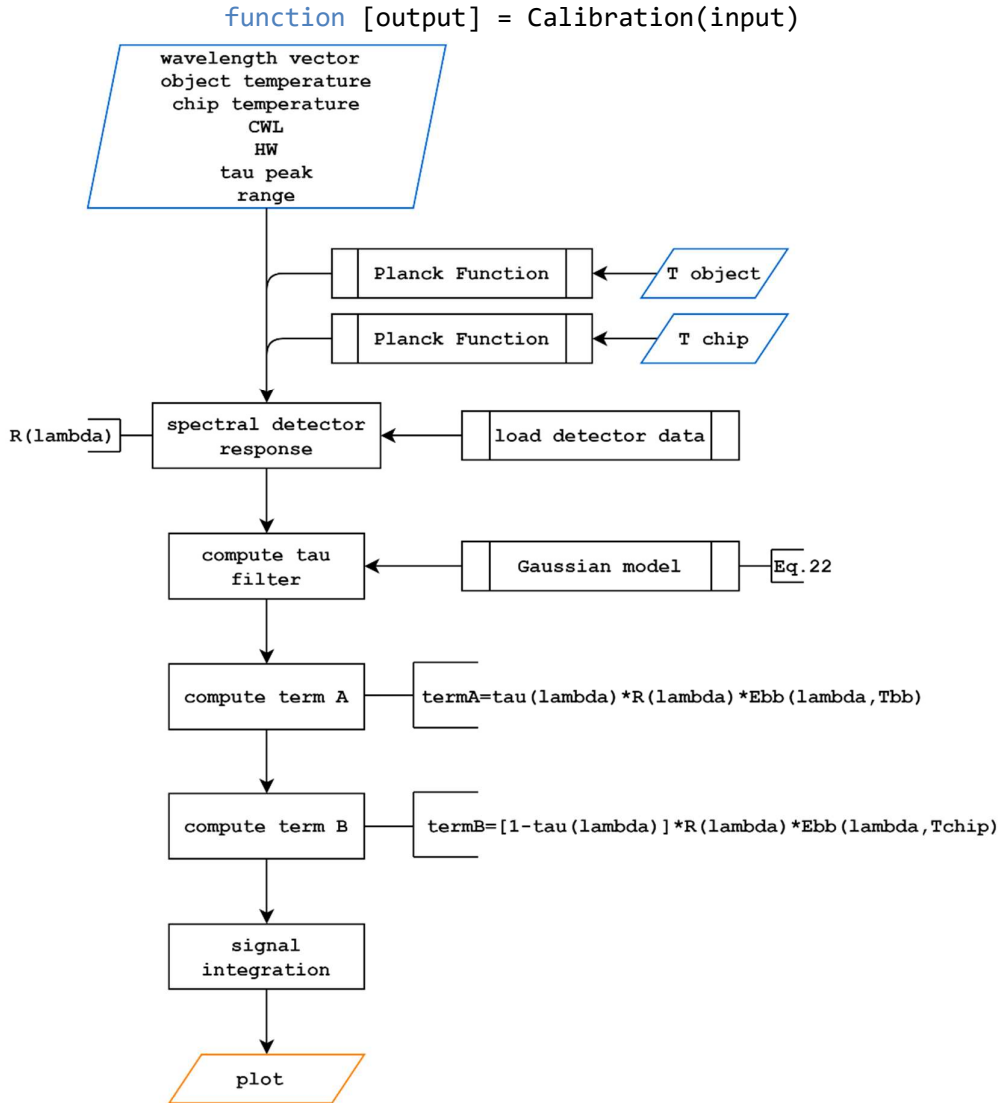


Figure 56 – Calibration script

Cost Function

The last function to be formulated before the creation of the Optimizer was the cost function. It operates using the following equation (Eq.29) in order to calculate the $\varepsilon\tau$ product relative to the signal simulated.

$$\varepsilon.\tilde{\tau}_3(CWL) = \beta_0 + \beta_1.CWL + \beta_2.CWL^2 \quad \text{Eq. 29}$$

This format has allowed us to calculate the $\varepsilon\tau$ product as a function of the filter central wavelength (CWL) from an initial starting point created by a vector with the following characteristics: $[\beta_0 \ \beta_1 \ \beta_2 \ T]$ in which T is the estimated temperature. The possibility of having either one, two or three different beta values depends on the kind of model that is intended to be used. In the following Table 10 there is a recapitulation of the possible model combinations.

Table 10 - Cost function models

	β_0	β_1	β_2	T	filters	$\varepsilon\tau$ condition
graybody assumption	$\neq 0$	0	0	discrete value	no maximum number	error lower than 1%
linear model	$\neq 0$	$\neq 0$	0	discrete value	minimum of two	values lay on a line
quadratic model	$\neq 0$	$\neq 0$	$\neq 0$	discrete value	minimum of three	values lay on a curve

Considering that the inputs for this function are largely different from the one observed above, for the sake of clarity they will need an introduction aside, in the following list they are explained in greater details:

- X as the vector $[\beta_0 \ \beta_1 \ \beta_2 \ T_{guess}]$
- S_ref the Signal used as a reference calculated using the Model Analysis function
- scalar parameters is a parameter vector to initialize filter calculations
 scalar parameters(1)=wavelength start
 scalar parameters(2)=wavelength stop
 scalar parameters(3)=chip temperature
- CWL is a vector of central wavelengths for the filter wheel
- filter vector is a vector listing filter IDs
- filter choice is a vector determined according to how many filters are needed
 for example the possible vector for filter selection could be [1 1 0 1 1] in order to select four filters or [1 0 0 1 1] for selecting three filters
- range is the spectrum of the Detector chosen either MWIR or LWIR

Finally, in the following flowchart the cost function is shown in details (Fig.57), it is important to underline that this function cover a major role as a backbone calculator for the optimizer.

```
function [RMSE_calc,S_calc]=
cost_function(X,S_ref,scalar_parameters,CWL,filter_vector,filter_choice,r
ange)
```

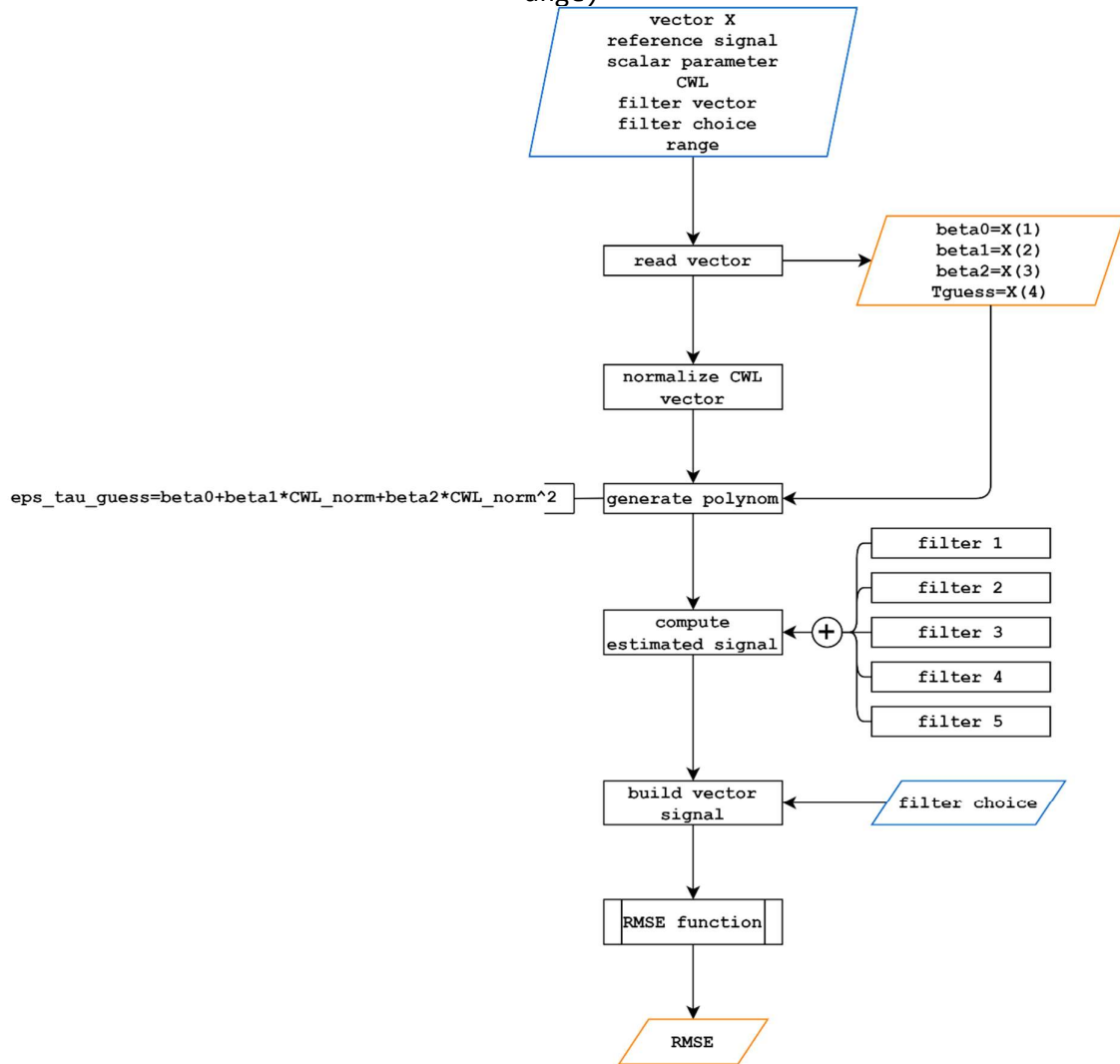


Figure 57 - Cost Function script

Optimizer Function

The Optimizer is characterized by two main streams that merge into the calculation for the RMSE as shown in Fig.58. The first stream as explained in the previous paragraph calculates the reference signal while the second stream is the result of the computation with the cost function. These two calculated signals for each filter combinations are the inputs for the RMSE calculation, which is the input of the inside function of MatLab® “*fminsearch*” defined by simplex algorithm with constraints represented by the input vector [27]. The main goal of this latter function is to find the minimum possible value of a function, in our case in the intrinsic value of RMSE. The function calculates various signals by changing the values of the beta and the temperature present in the vector used as input of the cost function to minimize the RMSE as an output. Once the procedure is over and the “*fminsearch*” can not find a lower values (usually it happens after some minutes of computation in which either it excess the interpolation point or the boundary conditions) the post processing part of the Optimizer code takes

place. In this last part of the code the calculated temperature and $\epsilon\tau$ products are compared to the reference ones to estimate the respectively absolute errors.

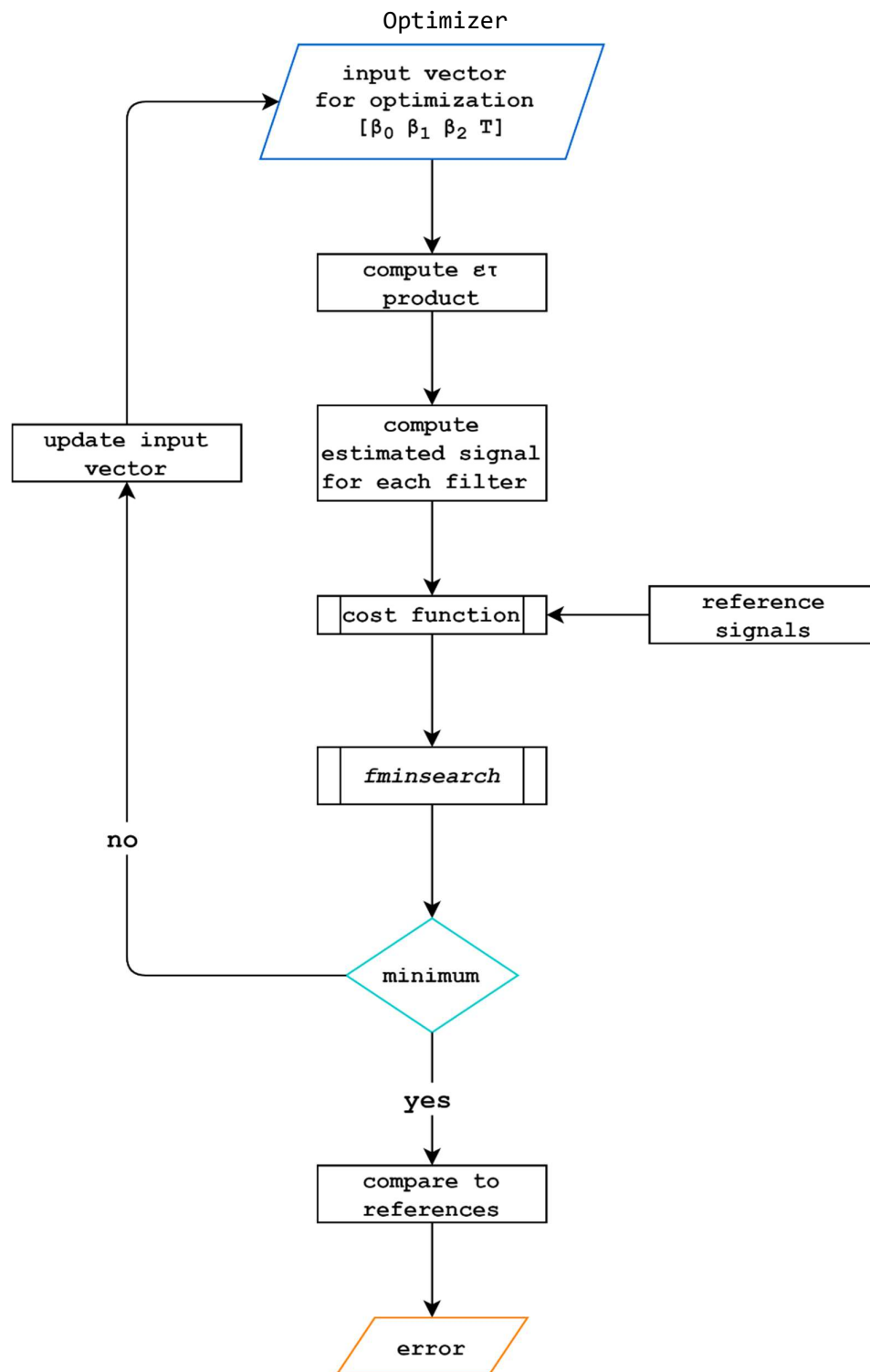


Figure 58 - Optimizer script

The optimizer results will be discussed in dept in the following chapter, however it is worth mentioning the usual procedure for which it was developed. It indeed gave a final big picture on the overall

method and problem solving technique followed to estimate how good a filter combination can perform. This can be recap in the following steps:

1. Simulation of the reference signal within boundary conditions
2. Filters permutations screening according to epsilon tau values
3. Signal calculation as a function of CWL using vector with beta values and temperature
4. Run the optimizer
5. Analyze the results

For a simulation run in order to be convincing it need to match our main target of calculate the separate error of $\epsilon\tau$ product and temperature, the errors criteria are:

- $\epsilon\tau$ product error below 1%
- temperature error below 10K

If these conditions are matched, the filters combinations undergo further analysis to double check their validity.

4. Simulation Results

Optimization Process

4.1 Simulations Target

The main goal for this work as anticipated before in paragraph 2.10 is the effective choice of a possible filter setups for a multispectral IR measurement technique. The latter using a spectral response in the SWIR , MWIR or LWIR range, has to perform in different environmental conditions in order to analyze various material types. The successful set up will be able to obtain information about both emissivity and temperature. For the purpose of choosing the right range and consequently the proper filter setup the simulations of this chapter were conducted to assess the following points:

- Validation of the model used
- Error analysis in multiple conditions
- Range evaluation
- Filter setups choice

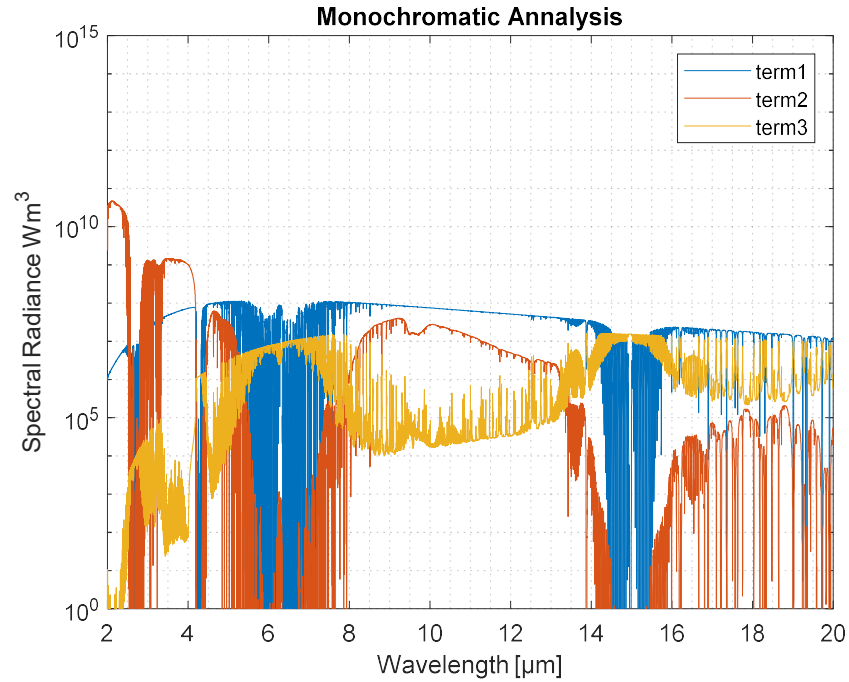
In the paragraphs that will follow the implementation of the various function at different levels and the results extracted will be discussed in greater details.

4.2 Early Test Runs

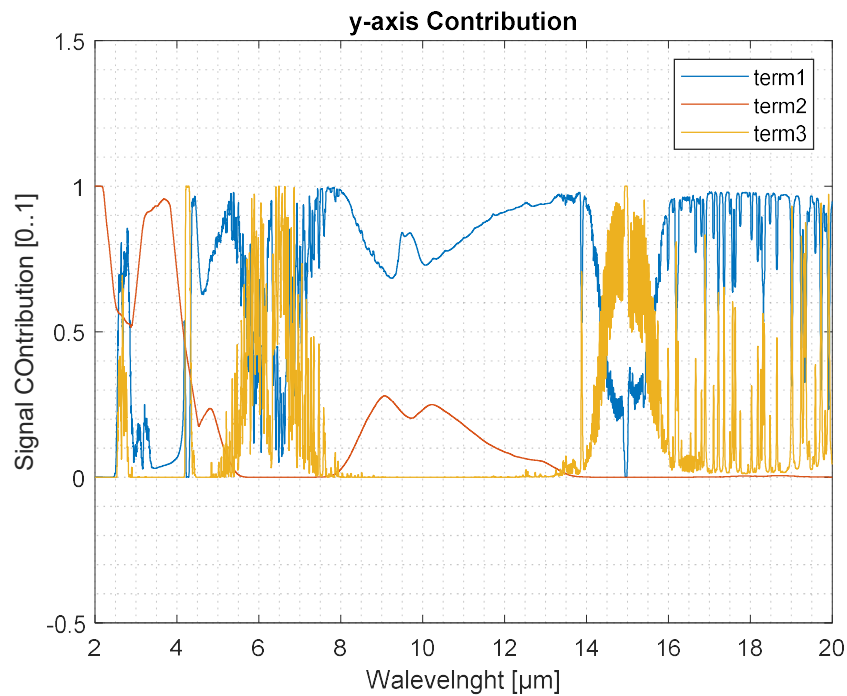
In order to achieve a fully integrated model that can run simulations smoothly without any problem, the first thing to do is the debugging of the code by running a sets of test. In total 8 different scenarios were scheduled to be able to have a first overview of the possible permutation options. It is also important to add that the Signal Analysis monochromatic function (Fig.52) was used, because this sets of simulations were focused only on the signal received by the camera without any camera parameters interference such as filter or detector, neither the range or specific material optical properties. The two different materials were treated as gray bodies. In the following Table 11 all scenarios are summarized, with results of the Scenario 8 shown as an example in the picture that follows (Fig.59).

Table 11 - Test scenarios for early signal tests

Scenario	Season	Material	Emissivity	Cx	T obj [°C]	T atm [°C]
1	summer	Pyromark 2500	0,9	200	800	21,05
2	summer	Pyromark 2500	0,9	1000	200	21,05
3	winter	Pyromark 2500	0,9	200	800	0,95
4	winter	Pyromark 2500	0,9	1000	200	0,95
5	summer	Haynes 230 / Oxidized	0,4	200	800	21,05
6	summer	Haynes 230 / Oxidized	0,4	1000	200	21,05
7	winter	Haynes 230 / Oxidized	0,4	200	800	0,95
8	winter	Haynes 230 / Oxidized	0,4	1000	200	0,95



a)



b)

Figure 59 - Graphs obtained after a simulation runs done with the Signal Analysis monochromatic function on Scenario 8. a) Calculation of the three terms. b) total signal contribution in percentage (0-1) over the total signal.

Even though the resolution of the outcome was low due to the fluctuation in the atmospheric dataset, it was possible to first have an overview of the different term contributions and their magnitude (Eq.19). This case, which results from a simulation run for Scenario 8, shows also which spectral windows could be used for further analysis. In this sense the graph (Fig.59b) highlights the predominant influence of the atmosphere in shaping the outcome in the 6-8 μm and 14-16 μm ranges,

this is due to the absorption bands of its components such as CO, CO₂, O₃ and H₂O, which are illustrated in the following pictures (Fig.60).

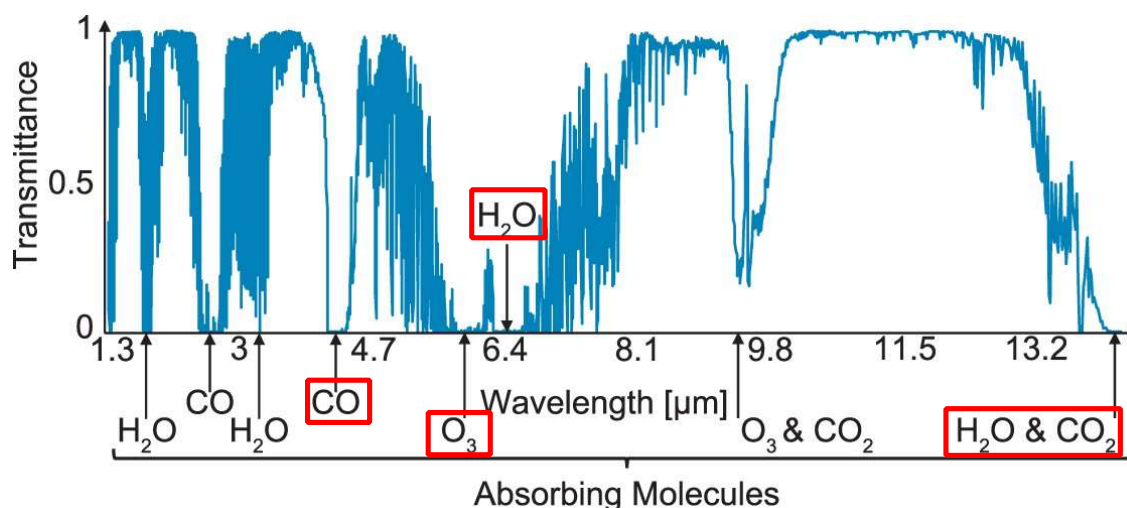


Figure 60 - Atmospheric transmittance with CO, CO₂, O₃ and H₂O absorption bands highlighted. [48]

Another observation from this early analysis is the dominance of term1 in the 8-14 μm range, as discussed in the previous paragraph this trend could be considered nearly as a solar blind condition [47]. This range is particular important because LWIR cameras can be considered as reference instruments for many applications. However there has not been yet a study to understand the performance of the different sub bands, because traditionally the LWIR cameras are focused only on a wider operative window. For this reason, we decide to further analyze the single bands in this spectral region in order to understand the possible temperature errors outcome, this will be discussed in the next paragraph.

4.3 Error Analysis

The main purpose of this analysis was to set the first impression of the possible permutations outcome of the measurement done in different LWIR ranges, for this reason the previous mentioned eight scenarios were tested in different single narrow bands and in wider bands located in the LWIR (8-14 μm) as shown in the following table (Table.12). In order to perform correctly this new set of temperature error analysis we switch from a monochromatic analysis to a band analysis, for doing so it was necessary to use the Signal Analysis band function (Fig.53), in which the temperature is no longer dependent on a single wavelength but instead integrated the spectral band.

Table 12 - Absolute temperature errors expressed in K results for the different scenarios in various wavelength range. The values were obtained by the error calculation feature intrinsic of the function (Fig.53).

Scenario\ Band	8-9 μm	9-10 μm	10-11 μm	11-12 μm	12-13 μm	13-14 μm	9-12 μm	8-14 μm
1	1,03	0,84	1,09	2,02	4,96	17,84	1,19	2,32
2	3,08	3,61	3,79	3,99	7,54	24,34	3,83	5,11
3	0,31	0,43	0,48	0,40	0,79	6,70	0,47	0,75
4	2,01	3,48	3,59	2,09	1,91	9,38	3,44	2,94
5	3,42	4,92	5,69	6,08	11,79	40,17	5,52	6,67
6	18,34	34,89	34,32	20,40	21,21	54,24	31,96	23,80
7	2,43	4,96	5,71	3,54	3,23	15,37	5,30	4,15
8	22,45	42,76	44,69	24,52	14,62	22,92	42,27	27,74

There are few patterns that can be extracted from this set of results. The first one is referred to Pyromark 2500, which was computed as a graybody with a emissivity value of 0.9 (Scenarios 1 to 4), and it is the increasing of the error magnitude with the increasing of the band wavelength. The same is not true however for the Haynes 230, computed as a graybody with a value of 0.4 (Scenarios 5 to 8), which absolute error is higher within the range of 9-11 μm than in the one of 12-14 μm . The second pattern is the influence of the season, as expected the error is lower in summer than in winter due to the higher atmosphere influences (Fig.32), this is particularly true for the Haynes 230 with high oscillations between scenarios for the 8-14 μm band for example. The next step after this first absolute temperature error overview was then to extend this simulation of the various scenarios to a higher number of possible iterations, such as neglecting the two terms and evaluate the consequences. In addition of the multiple combinations the different analysis were conducted on the bias of the +/-1% errors listed in the following Table 13. For the sake of clarity, the following equation (Eq.30) explains in a simpler way the physical interpretation behind this error analysis.

$$\text{signal} = \text{term1} + \text{term2} + \text{term3} \quad \text{Eq.30}$$

Where

- Term1 is the object emission
- Term2 is the reflection of concentrated solar radiation
- Term3 is the atmospheric emission

The three terms have different related dependence, in fact term1 depends on $\varepsilon * \tau$, term2 depends on $(1-\varepsilon)*\tau$ and term3 depends on $1- \tau$. The reference equation Eq.19 used for this error evaluation is explained in the previous chapter 2.12. However considering the function used (Fig.53) the detector, filter and materials influence were neglected. In fact, in this analysis was focused on the collection of data regarding the contribution in magnitude of the single terms and variables of the code. This was done in case an error would have occurred at different level and to understand how it would be translated in the error on the measured temperature.

Table 13 - Set up for error magnitude analysis for the bands listed in Table 12

Analysis	term 2	term 3	ε error	τ error	$\varepsilon * \tau$ error	signal error*
1	negligible	negligible	no	no	no	no
2	negligible	negligible	$\pm 1\%$	no	no	no
3	negligible	negligible	no	$\pm 1\%$	no	no
4	negligible	negligible	no	no	$\pm 1\%$	no
5	negligible	negligible	no	no	no	$\pm 1\%$
6	significant	significant	no	no	no	no
7	significant	significant	$\pm 1\%$	no	no	no
8	significant	significant	no	$\pm 1\%$	no	no
9	significant	significant	no	no	$\pm 1\%$	no
10	significant	significant	no	no	no	$\pm 1\%$

Considering the high volume of data obtained in the digital appendix every single one of the contour maps generated will be available for consulting. However it is important to highlight the most significant outcome such as:

1. Error calculations done by neglecting terms 2 and terms 3 (Eq.30) are affected by systemic temperature error due to the independence of the result on the concentration factor, as illustrated in Fig.61.

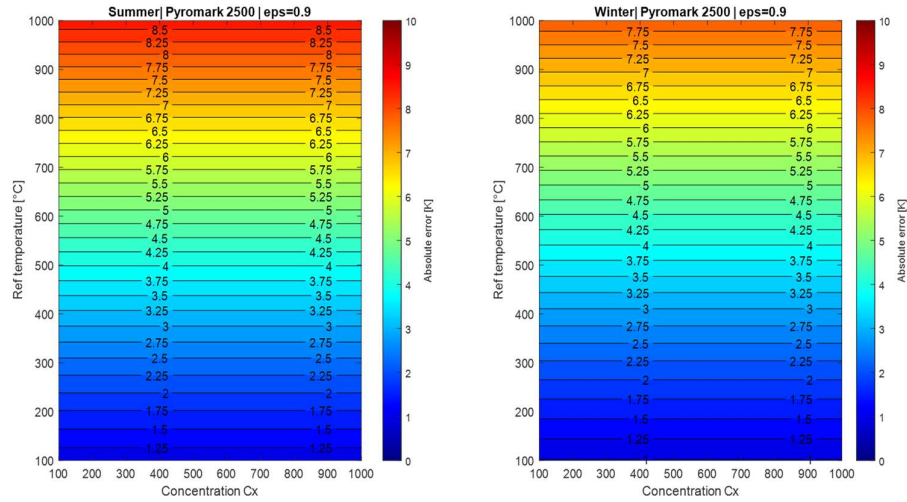


Figure 61 - Contour maps for comparison of the different performances between Pyromark 2500 in summer and winter using a band in the range of 8-14 μ m.

These graphs were obtained after running Analysis 3, the error values are located on parallel lines which values growing according to the reference temperature. As mentioned earlier the error is symmetric, in the sense that -1% and +1% specifications generate the same error outcome. Another feature about the different between the season is that the error dependence shows the same behavior but the magnitude is different. The winter analysis shows a lower error values compared to the one in summer, this is due to the τ error present in this specific case, which unbalance the ordinary seasonal dependence (Fig.32).

- Confirmation of the higher magnitude of temperature error for H230 than for Pyromark 2500, expected considering the different in emissivity, as shown in Fig.62.

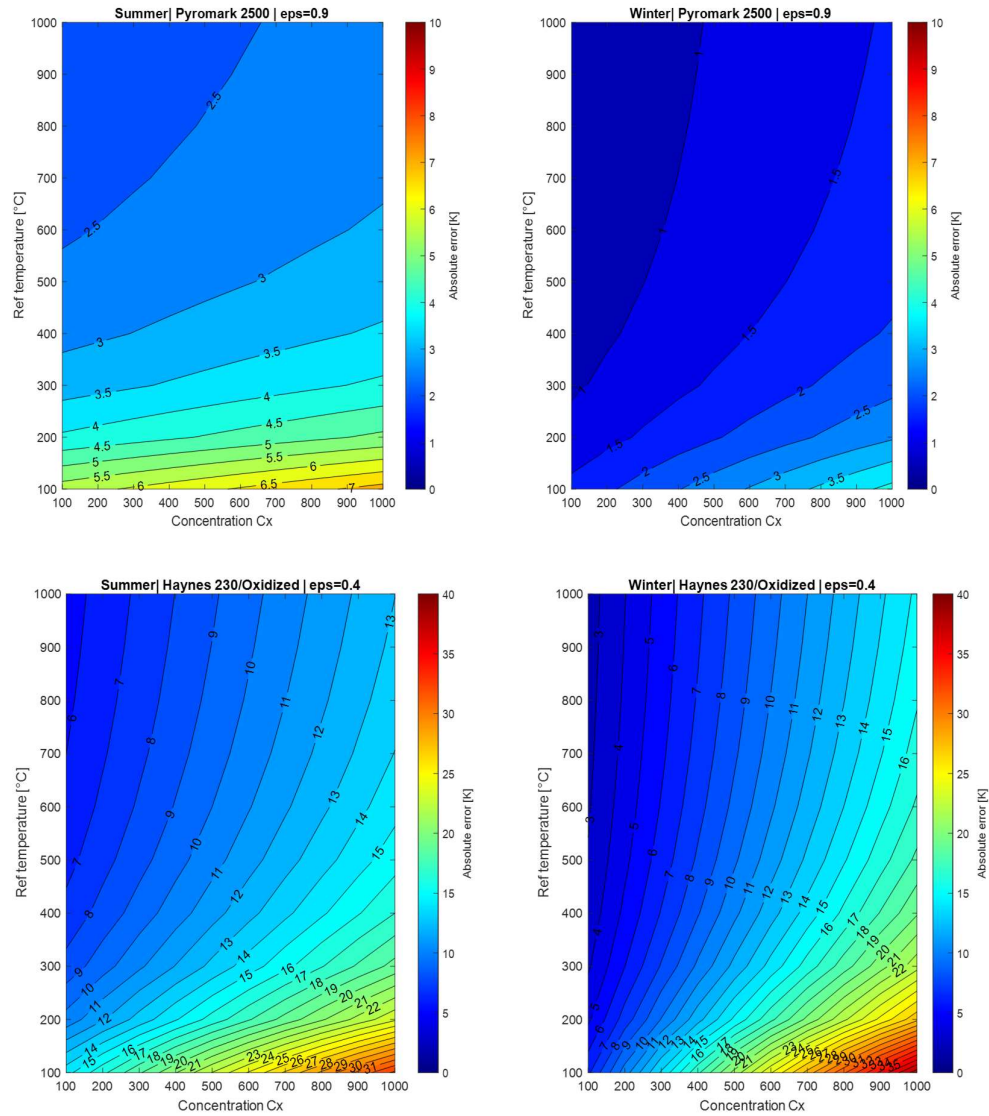


Figure 62 - Contour maps for comparison of the different performances between Pyromark 2500 and Haynes 230 in summer and winter using a narrow band in the range of 8-14 μ m.

This Analysis 6 shows how the temperature error outcome is affected by the implementation into the radiometric equation of term 2 and term 3, while maintaining zero the error on the other variables, ϵ and τ respectively (Eq.30). Two major trends can be identified in these graphs. The first one is referred to the temperature error values which are proportional with the increasing of the concentration factor but at the same time they are decreasing by the incrementation of temperature. This can be explained by the fact that at low temperature and high concentration factor the signal from the black body is highly affected from the noise generated by the sun radiation (term2) (Eq.19). The other trends mentioned also above is regarding the different magnitude of error for the two different materials, this can be explained by the high difference in emissivity which lead to a higher temperature error for lower emissivity values

3. Asymmetrical temperature error while implementing term 2 and 3 (Eq.30), see Fig.63.

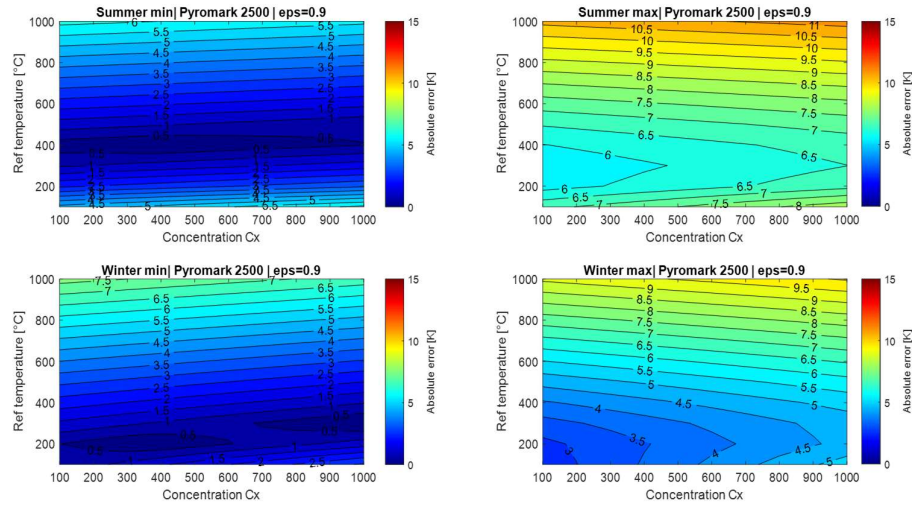


Figure 63 - Contour maps for comparison of the different performances between Pyromark 2500 in summer and winter using a narrow band in the range of 8-14 μ m Analysis 7.

In this case it is shown Analysis 7, the main feature of this graphs is the min and max sub division. It could be explain by the two possibilities as +1% and -1% errors on the ϵ value while implementing term 2 and term 3, indeed this leads to a differentiation of 4 outcomes.

4. “Islands” where the temperature error is close to zero were noticed while running error on the tau and considering also term 2 and term 3 into the equation, this means that the system basically compensate the temperature error, see Fig.64 in which is shown Analysis 10.

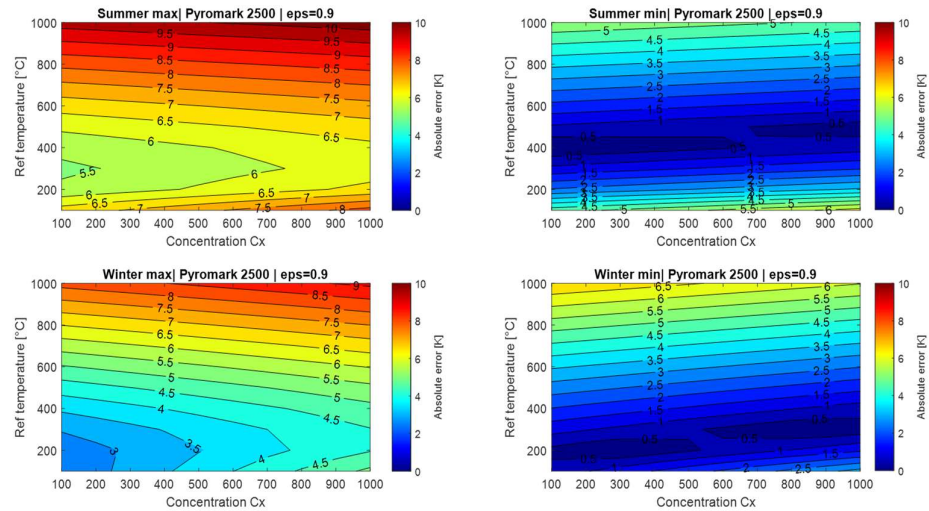


Figure 64 - Contour maps for comparison of the different performances between Pyromark 2500 in summer and winter using a narrow band in the range of 8-14 μ m.

4.4 Filter Calibration

After the results obtained by the error analysis shown before, then next step was the analysis in the same range of the effect of the filter implementation to have a deeper understanding about how they would affect the signal. This step required a specific function called Calibration, which is illustrated in Fig.56. In total, two different sets of simulation were done, in the first simulation setup HW was maintained constant for all filters to show the dependence of the signal on CWL, it was clear after running the code that lower the CWL the higher is value of the slope of the signal curve generated, see Fig.65.

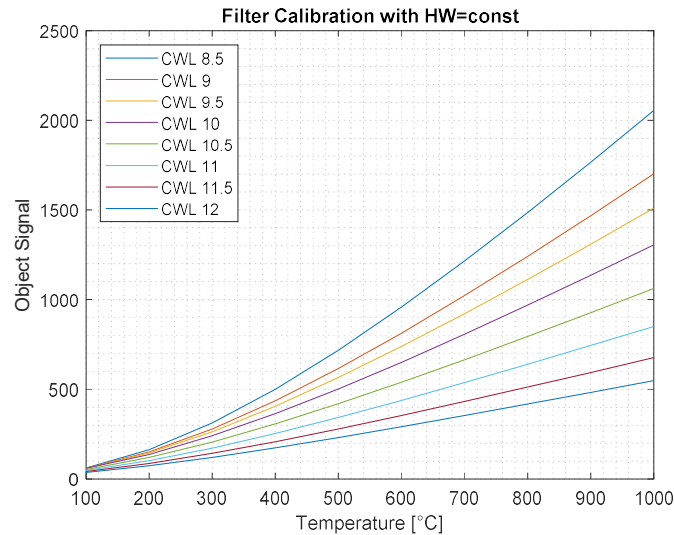


Figure 65 - Filter Calibration results obtained with a constant HW=0.6.

It is possible to estimate that at higher temperature the contribution of the filter with lower CWL is lower because the signal generated is stronger. In the second simulation set, CWL was maintained constant while the signal was studied on the dependence of HW. In this case the higher the HW is the higher is the slope the signal, so there is a direct correlation, making the narrower the band filter the more affected by the temperature change, so with a lower signal outcome (Fig.66).

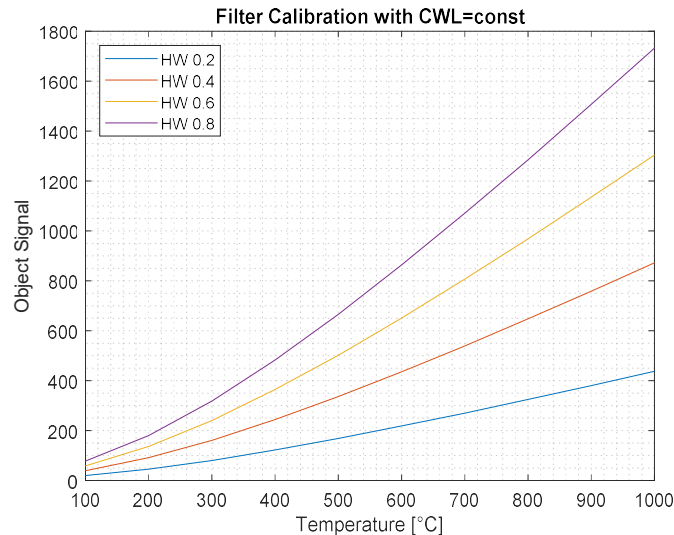


Figure 66 - Filter Calibration results obtained with a constant CWL=10

4.5 Optimizer Strategy

After the results of the filter calibration were proceeded, we extended the analysis to a wider range of combinations to select the most suitable spectral range (SWIR/MWIR/LWIR) and the corresponding filter set. Knowing the computation capability of the Optimizer, as described in the previous chapter, a strategy was needed to analyze properly the amount of data obtained by the possible permutations of filter, materials and environment conditions. In order to achieve this, we decided first to divided the analysis in the three different major groups based on the spectral range: SWIR, MWIR and LWIR. Once the range was fixed, this gave us the possibility of screening the performance of different filter combinations .

This process was divided into two different part for each range. The first was the evaluation of the filters, this means that various filters will be analyzed in fixed boundary conditions such as body temperature, season, material chosen and concentration factor. Afterwards the filters were evaluated and tested according to the criteria related to the $\varepsilon\tau$ condition of Table 10, if these conditions were matched then the filters would be selected for the next step. The latter was the analysis of the filter in the scenarios previously listed in Table 11. However, the difference in comparison to the early test was the use of the Model Analysis function, which allowed us to generate a fully integrated signal dependent on the filter, detector and the real material emissivity. The settings for the various camera was the final adjustment added, in fact using three different detector leads to three different camera setups, all listed in the following Table 14.

Table 14 - Camera setups for the three different ranges

	SWIR	MWIR	LWIR
wavelength vector [μm]	1-2	2-6	6-18
chip temperature [$^{\circ}\text{C}$]	30	-196	45
distance path 3 (d3) [m]	50	200	200

Another note worth mentioning is about the graph and data displayed in the following paragraphs. Considering the amount of computation work done for all the different range analysis only a small part of the data obtained is shown, the most significant results. The rest of all calculations is available for consulting in the digital appendix of this work.

4.6 SWIR Analysis

The cost function model integrated for this case was the gray body assumption, in fact for both materials considered in the analysis, Pyromark 2500 and Haynes 230, the emissivity shows an almost linear behavior in the SWIR range (Fig.34). From Spectrogon [44] we obtain two filters, one centered at $1.4\ \mu\text{m}$ and the other one centered at $1.9\ \mu\text{m}$. The pairs used for this case are sum up in the following list:

- combination 1: {1386; 1912}
- combination 2: {1394; 1912}
- combination 3: {1370; 1850}

The reason why these combinations were chosen instead of pairs with closer wavelength is to maintain the gray body assumption valid. In fact, in order to do so the filters CWL should be chosen as close as possible, however having the two filter too close to each other induce a decrease in sensitivity that leads to an increase of measurement error. Therefore, it can compromise the validity and the results of the model used [19]. Once we simulated the $\varepsilon\tau$ product for each filter, we obtained another confirmation that the gray body assumption model was the only one suitable for this range. In fact, in order to choose the filters correctly their characteristics have to satisfy the $\varepsilon\tau$ condition of Table 10.

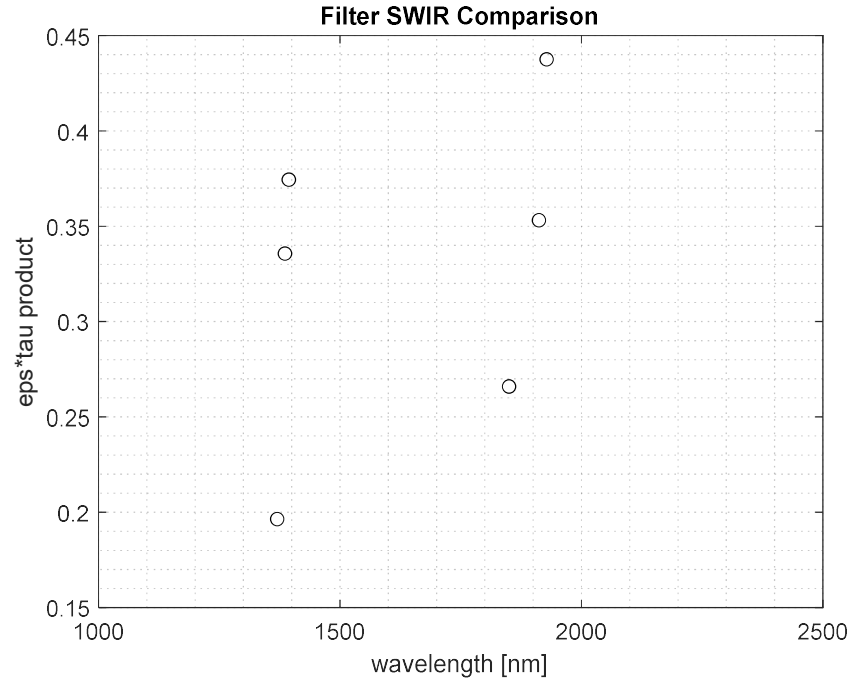


Figure 67 - $\epsilon\tau$ product filter comparison for SWIR range calculated for Pyromark cured at 750°C, for summer condition with a $\alpha_x=200$ and a $T_{bb}=800^\circ\text{C}$.

This number of filter arrangements meant that the previously listed pairs were directly tested in the different scenarios for both materials, the following Tables 15, 16 and 17 show the result obtained.

Table 15 - SWIR combi1 Optimizer Analysis result.

SWIR combi 1 errors overview				
Scenario	Absolute $\epsilon\tau$ product error [0...1]		T ref [K]	T error [K]
1	0,0687	0,0512	800	20,33
2	0,3391	0,3546	200	94,20
3	0,0513	0,0374	800	9,41
4	0,6467	0,6333	200	diverge
5	0,0458	0,0338	800	15,40
6	0,3063	0,3165	200	94,97
7	0,0730	0,0536	800	15,50
8	0,5838	0,5648	200	diverge

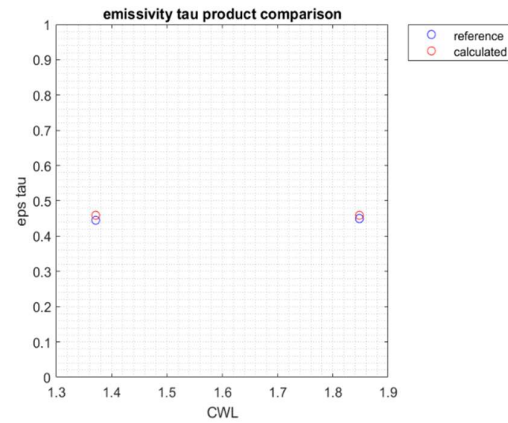
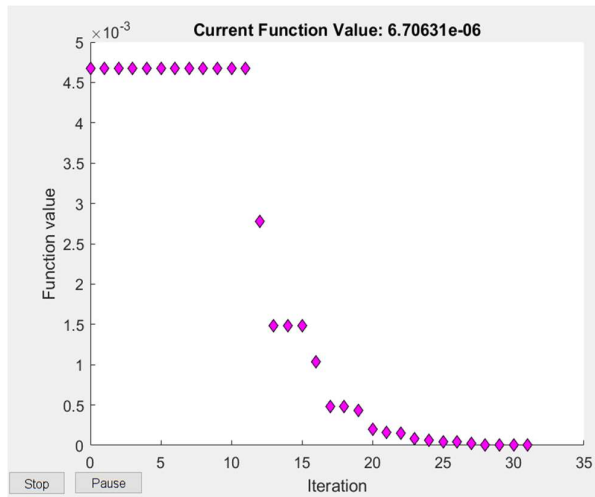
Table 16 - SWIR Combi2 Optimizer Analysis result.

SWIR combi 2 errors overview				
Scenario	Absolute $\epsilon\tau$	product error [0...1]	T ref [K]	T error [K]
1	0,0722	0,0509	800	20,33
2	0,3391	0,3546	200	94,20
3	0,0846	0,0605	800	9,41
4	0,6551	0,6325	200	diverge
5	0,0757	0,0526	800	15,40
6	0,3400	0,3165	200	94,97
7	0,0987	0,0702	800	15,50
8	0,5919	0,5646	200	diverge

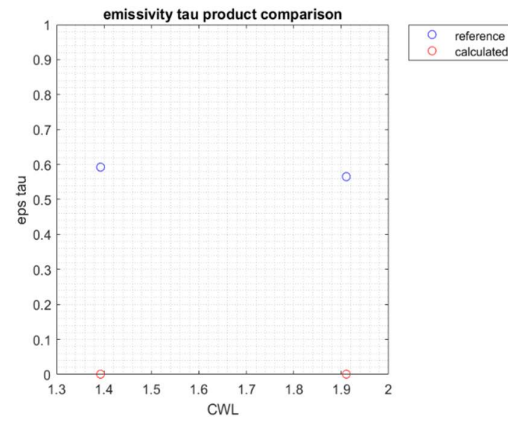
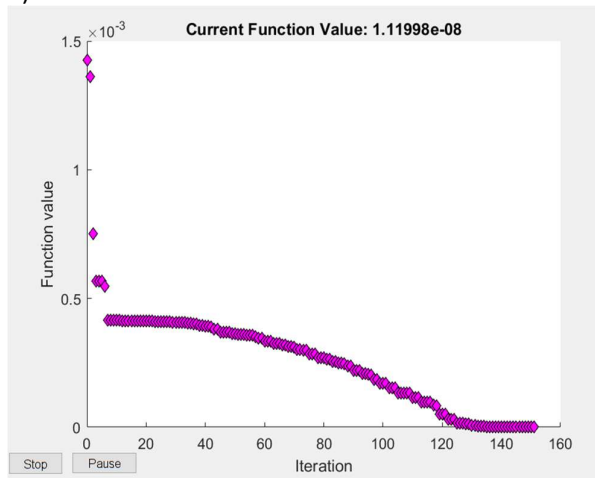
Table 17 - SWIR Combi3 Optimizer Analysis result.

SWIR combi 3 errors overview				
Scenario	Absolute $\epsilon\tau$	product error [0...1]	T ref [K]	T error [K]
1	0,4387	0,3692	800	114,94
2	0,1957	0,2658	200	96,98
3	0,0413	0,0306	800	8,65
4	0,4916	0,5031	200	95,48
5	0,3697	0,3094	800	110,60
6	0,1769	0,2376	200	99,38
7	0,0141	0,0093	800	3,08
8	0,5927	0,5654	200	99,99

In the case of Pyromark 2500 , from the scenario 1 to scenario 4, the behavior is similar for the different combination, the results indeed show that a combination of lower concentration factor and higher temperature leads to a lower measurement error. However, for Haynes 230 the results were contradictory, the lower error was recorded in scenario 7. One of the scenario that should have had a different outcome considering the influence of the atmosphere in a radiation obtained from a material with such emissivity. This is shown in the Fig.68a where both RMSE and $\epsilon\tau$ product are displayed. The carryout points for this set of results is also the limit of this method. In fact if we compared the results of the scenarios in which the optimizer interpolation “diverge” with the one of the RMSE it is possible to notice that in this case even though the value of the temperature error is still higher than the acceptable one the RMSE shows a very low value. This puts the spotlight on the fact that through this analysis we arrived at the very limit capabilities of this process, in fact the optimizer had found the optimal values within the boundary condition and settings but this is not in line with the temperature error wanted. An example of this is illustrated in Fig.68b where even though the RMSE value stop at $11,12 \cdot 10^{-8} \epsilon\tau$ product calculated compare to the reference one is affected by an huge error and this also relates to the divergence in the temperature error.



a)



b)

Figure 68 - RMSE final value and $\epsilon\tau$ product comparison for two different scenarios outcomes with CWL expressed in μm . a) scenario 7 combi 3; RMSE: $6,70\text{e-}06$; Absolute temperature error: $3,08\text{K}$; $\epsilon\tau$ error $0,0141$ and $0,0093$. b) Scenario 8 combi 2; RMSE: $1,11\text{e-}08$; Absolute temperature error: diverge; $\epsilon\tau$ error $0,5919$ and $0,5646$

4.7 MWIR Analysis

The same strategy was followed to evaluate the possible filter for this range, after calculating the $\epsilon\tau$ product for each filter we used the plot to screen for possible combination according to the criteria of Table 10. For the MWIR there are a total of seven filter a disposal, in the following picture Fig.69 illustrates the result of the $\epsilon\tau$ product for every one of them.

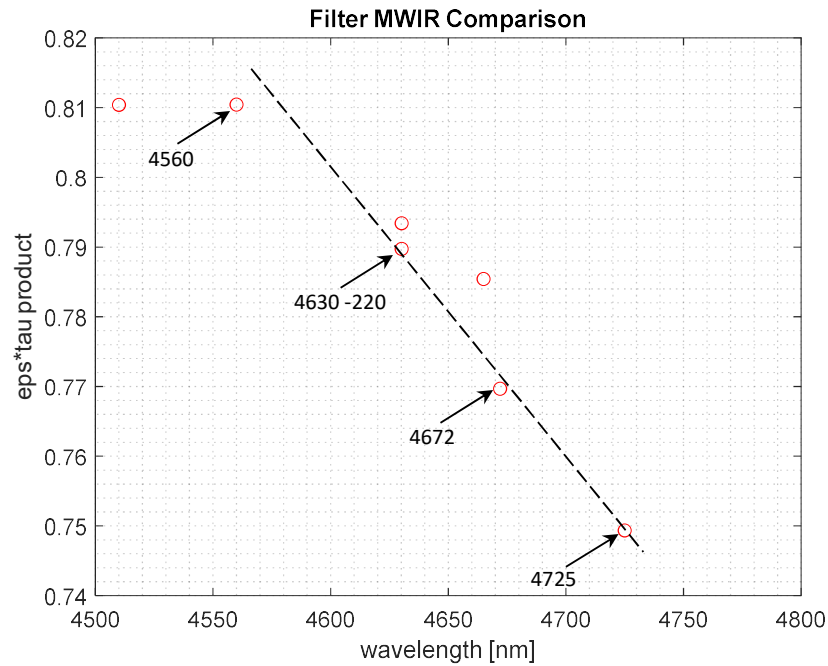


Figure 69 - $\epsilon\tau$ product filter comparison for MWIR range calculated for Pyromark cured at 750°C, for summer condition with a $cx=200$ and $Tbb=800^\circ\text{C}$.

After the initial screening four filters out of the total number of seven were selected for further analysis. The main reason for this choice as highlighted in Fig.69 is the position of their $\epsilon\tau$ product on a line in the plot, for this reason according to the criteria of Table 10 the linear model could be also used, since the values lay on a line. The next step was the creation of the various permutation of filter, these are displayed in the following Table 18.

Table 18 - Filter permutations for the MWIR range with model chosen accordingly.

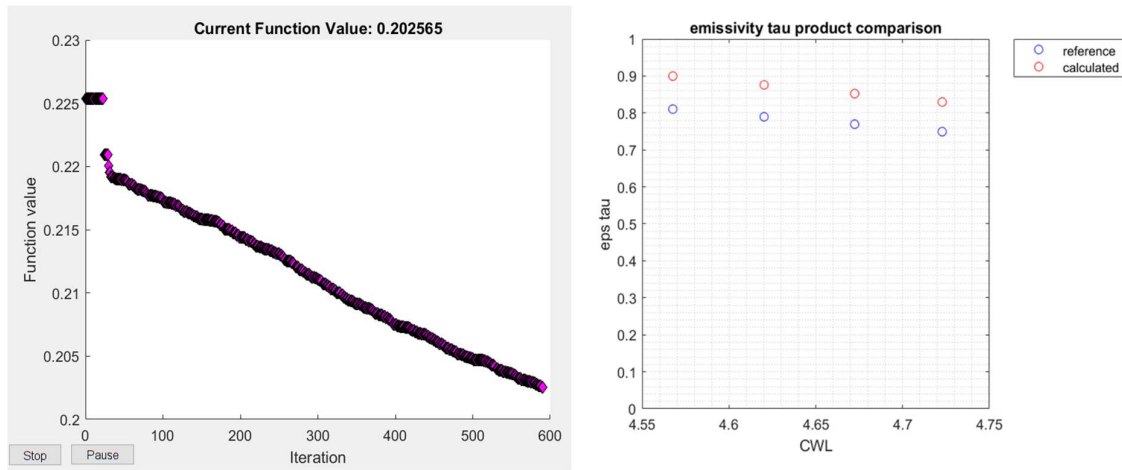
Combination	Filters choice				Model
1	4672	4725	[-]	[-]	gray body
2	4630-220	4725	[-]	[-]	gray body
3	4630-220	4672	[-]	[-]	gray body
4	4630-220	4672	4725	[-]	linear
5	4560	4725	[-]	[-]	gray body
6	4560	4672	[-]	[-]	gray body
7	4560	4672	4725	[-]	linear
8	4560	4630-220	[-]	[-]	gray body
9	4560	4630-220	4725	[-]	linear
10	4560	4630-220	4672	[-]	linear
11a	4560	4630-220	4672	4725	linear
11b	4560	4630-220	4672	4725	quadratic

The different model cases were chosen accordingly to the number of filter available for every specific combination. In this sense the case for the combi11 gave us also the possibility to evaluated the different within two methods (linear and quadratic), since a total of four filter were available for testing. The pilot run for the initial screening of the filter was done considering scenario 1 without the noise factor, that means neglecting term 3 (Eq.19 or Eq.30). The results obtained are shown in the following Table 19.

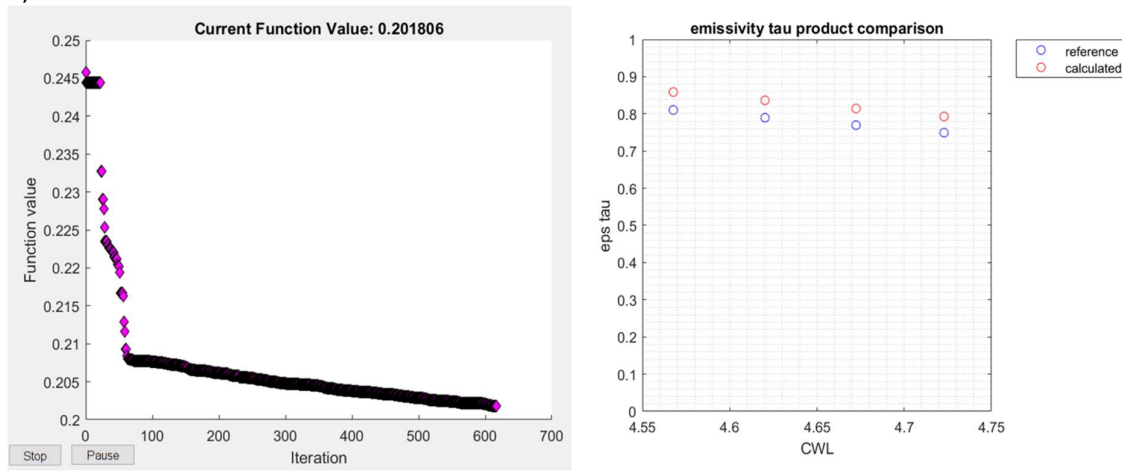
Table 19 - MWIR filters combination screening. Scenario 1 neglecting term 3 (atmospheric emission Eq.19) was the choice of boundary condition for these test runs.

Combination		Absolute $\epsilon\tau$ product error			T error [K]
1	0,3013	0,2809	[-]	[-]	200
2	0,3106	0,2702	[-]	[-]	200
3	0,3084	0,2883	[-]	[-]	200
4	0,0132	0,0008	0,0121	[-]	8,10
5	0,3309	0,2698	[-]	[-]	200
6	0,3262	0,2854	[-]	[-]	200
7	0,1124	0,1043	0,1011	[-]	43,28
8	0,3242	0,3034	[-]	[-]	200
9	0,0026	0,0025	0,0023	[-]	1,11
10	0,5787	0,0015	0,0014	[-]	0,58
11a	0,0893	0,0863	0,0828	0,0804	35,12
11b	0,0482	0,0467	0,0447	0,0435	19,69

There are few main outcomes relevant to this analysis, the first one is of course the choice of possible combination for scenario 1 for further simulations. In this case the most valid candidate were combi4, combi9 and combi10, which have the three lowest absolute temperature errors recorded. This can be explained by two main different reasons. The first one is about the model, indeed the linear model offers a better approximation compare to the graybody model, this leads to a better outcome results. The second one, which also explains why these three combinations performed better compared to other combinations using the same model, can be referred to the slope generated between the three emissivity values. In fact the closer the simulated emissivity profile is to the slope of the real material emissivity curve the better the signal response will be [49]. However the second important outcome from this set of simulations was the test of two different methods within the same condition. The results are compared in the following Fig.70, in which it is noticeable how the quadratic method performed better than the linear one. One thing that is worth underlining is the comparison of both RMSE, in fact even though both methods share the same magnitude of RMSE the results in term of temperature and $\epsilon\tau$ product is much better for the quadratic model. Due to the better approximation of the curve overall these results were expected. Continuing the discuss throughout the various model, the next main trend of this analysis is the failure of the gray body assumption. In fact all combination tested with this method showed a massive error in both temperature and $\epsilon\tau$ product. This can be related to the fluctuation of the emissivity for Pyromark 2500 in this range (Fig.34), especially compared to the SWIR region where the materials showed a much lower deviation.



a)



b)

Figure 70 - RMSE final value and $\epsilon\tau$ product comparison for the same filter combination but with different models used. CWL is expressed in μm . The sub division of graphs is as follow: a) combi 11a results from the linear model. RMSE: 0,2025; Absolute temperature error: 35,12K; $\epsilon\tau$ 0,0893 0,0863 0,0828 and 0,0804. b) combi 11b tested using the quadratic model. RMSE: 0,2018; Absolute temperature error: 19,69K; $\epsilon\tau$ 0,0482 0,0467 0,0447 and 0,0435

The best three filters combinations, which in comparison with the other combinations showed values that satisfied the errors condition formulated in the previous chapter, were then test for the various scenarios. The results are summarized in the following Tables 20, 21 and 22.

Table 20 - MWIR Combi4 Optimizer Analysis result.

MWIR combi 4 errors overview					
Scenario	Absolute	$\epsilon\tau$ product error [0...1]		T ref [K]	T error [K]
1	0,0233	0,0229	0,0233	800	1,05
2	0,0540	0,0527	0,0533	200	0,20
3	0,0920	0,0900	0,0896	800	33,05
4	0,1625	0,1613	0,1620	200	8,17
5	0,0269	0,0259	0,0268	800	3,15
6	0,0540	0,0523	0,0535	200	1,15
7	0,0259	0,0245	0,0258	800	8,85
8	0,1956	0,1941	0,1956	200	9,69

Table 21 - MWIR Combi9 Optimizer Analysis result.

MWIR combi 9 errors overview					
Scenario	Absolute ϵ	product error [0...1]	T ref [K]	T error [K]	
1	$1,8 \cdot 10^{-4}$	$2,1 \cdot 10^{-4}$	$2,3 \cdot 10^{-4}$	800	0,01
2	0,0285	0,0285	0,0279	200	0,52
3	$5,1 \cdot 10^{-4}$	$1,6 \cdot 10^{-4}$	$4,5 \cdot 10^{-4}$	800	0,02
4	0,1060	0,1061	0,1079	200	4,64
5	0,0925	0,0890	0,0831	800	38,08
6	0,0328	0,0324	0,0318	200	1,19
7	0,0663	0,0660	0,0635	800	31,45
8	0,2090	0,2079	0,2083	200	11,12

Table 22 - MWIR Combi10 Optimizer Analysis result.

MWIR combi 10 errors overview					
Scenario	Absolute ϵ	product error [0...1]	T ref [K]	T error [K]	
1	0,0150	0,0147	0,0140	800	6,29
2	0,1057	0,1062	0,1053	200	5,83
3	0,0014	0,0012	0,0013	800	0,61
4	0,0387	0,0443	0,0497	200	0,31
5	0,011	0,0013	0,0011	800	0,46
6	0,0594	0,0531	0,0483	200	9,89
7	0,0691	0,0684	0,0672	800	28,23
8	0,1612	0,1676	0,1737	200	8,11

The results obtained from the MWIR show that all three combinations performed well in all sort of condition, however there are few cases that need to be explicitly pointed out. The first one is about scenario 3 for combi4, scenario 5 for combi9, scenario 7 for combi9 combi10. These four results are affected from an intrinsic problem of the process, in fact the computation stop at this point for exceeding the maximum amount of iteration available, without being able to proceed further and finding the lowest RMSE possible. This is one of the few cases in which we reached the limit of the optimizer. Another feature of this set of results is the error magnitude trough the scenario, a trend that was first noticed during the contour map runs. In fact, the temperature error is lower for the analysis of both materials that took place in summer condition compare to the one in winter, with of course the same concentration factor value. This is due to the higher influence of the atmosphere and in the following Fig.71 the result obtained from Pyromark 2500 are compared.

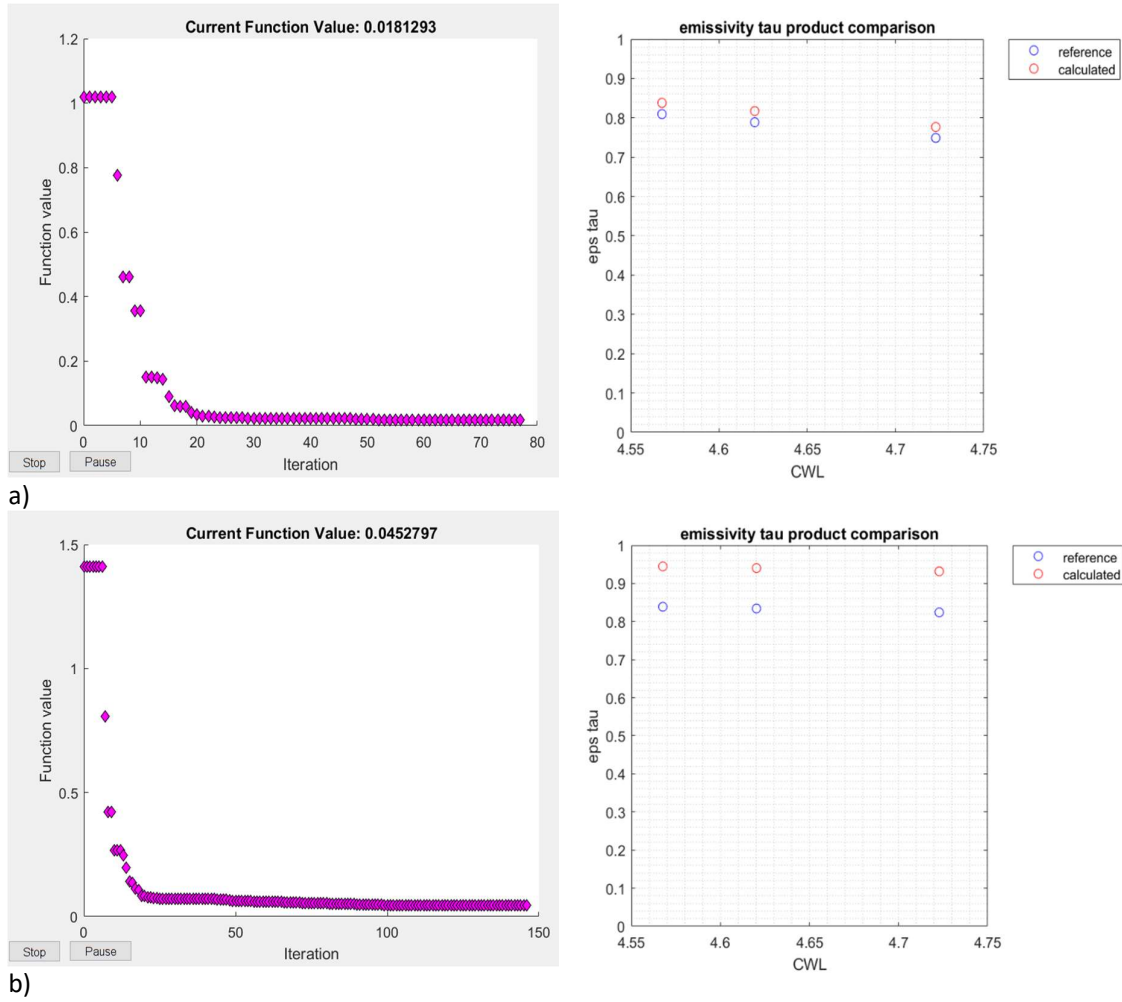


Figure 71 - RMSE final value and $\epsilon\tau$ product comparison for the same filter combination tested for the same materials as Pyromark 2500 in the same condition of concentration factor. However the underline different is the season. CWL is expressed in μm . The sub division of graphs is as follow: a) combi 9 scenario 2; RMSE: 0,018; Absolute temperature error 0,52K; $\epsilon\tau$ error: 0,0285 0,0285 and 0,0279 b) combi9 scenario 4; ;RMSE: 0,045; Absolute temperature error 4,64K; $\epsilon\tau$ error: 0,1060 0,1061 and 0,1079.

4.8 LWIR Analysis

Once again, we adopted the strategy discussed before for the analysis of the next and final range, the LWIR region. In this case however the filter choice possibility was not entirely free, in fact as shown in the following figure (Fig.72) only 8645, 8900, 9127 and 9480 filters were available for the choice, despite the arrangement on almost a perfect line of the other $\epsilon\tau$ product for the filters with $\text{CWL} > 10\mu\text{m}$ and therefore with the possibility of using a linear model. The reason for this is related to the filter calibration, in fact as showed in the previous paragraph (Fig.65) the increase of the CWL is combined with a decrease of the outcome signal. The latter will lead to lower sensitivity and indeed a higher measurement error, this is true especially for normal working condition where the noise generates from the surrounding would deeply affect the body radiation. Another reason that can be added for the unfavorable conditions of the filter with $\text{CWL} > 10\mu\text{m}$ is related to the material emissivity. If we take a closer look at Fig.34 Haynes 230 in particular shows an high fluctuation of the emissivity value in this region, making the gray body assumption non applicable and therefore most of the pairs combinations not possible.

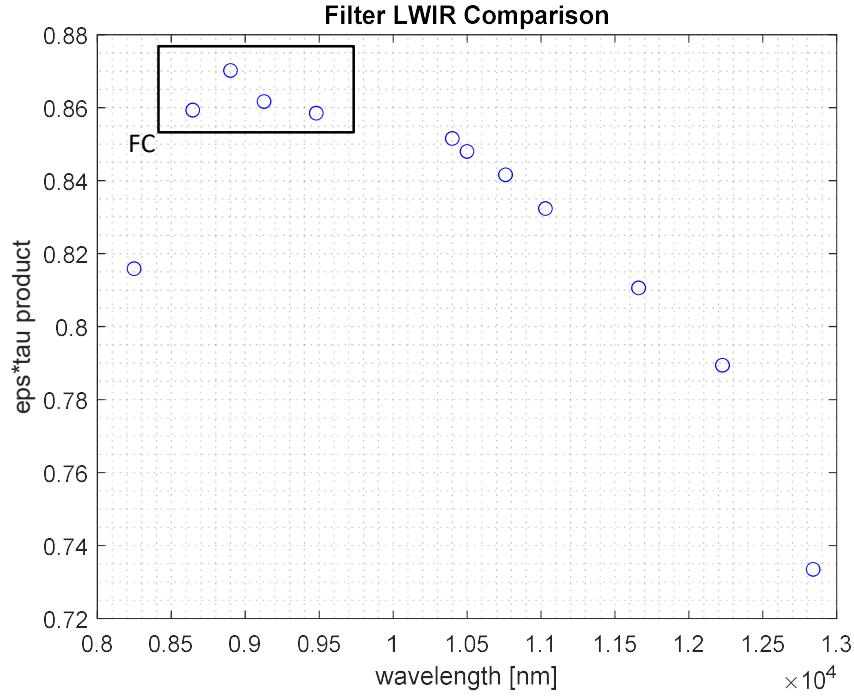


Figure 72 - $\epsilon\tau$ product filter comparison for LWIR range. FC stands for filters chosen and within this box there are the four filters used for further evaluation, in order from the lower to higher CWL: 8645, 8900, 9127 and 9480.

The filters highlighted in the previous Fig.72 undergo as standard procedure to a permutation series in order to obtained all possible combination, which are displayed in the next Table 23.

Table 23 - LWIR filters permutation and model chosen

Combination		Filters choice			Method
1	9127	9480	[-]	[-]	gray body
2	8900	9480	[-]	[-]	gray body
3	8900	9127	[-]	[-]	gray body
4	8900	9127	9480	[-]	linear
5	8645	9480	[-]	[-]	gray body
6	8645	9127	[-]	[-]	gray body
7	8645	9127	9480	[-]	linear
8	8645	8900	[-]	[-]	gray body
9	8645	8900	9480	[-]	linear
10	8645	8900	9127	[-]	linear
11	8645	8900	9127	9480	linear

As mentioned before in this range both materials show an almost gray body behavior in they emissivity value (Fig.34), so for this reason the results it was expected that the result for the gray body model in this case would have been better that the ones of the MWIR, as shown in the following Table 24. However, in comparison to the MWIR only two combination of filters matched our condition for further evaluation, these two were combi5 and combi7.

Table 24 - LWIR filters combination screening. Scenario 1 neglecting term 3 (noise factor) was the choice of boundary condition for these test runs.

Combination	Absolute ϵ product error				T error [K]
1	0,1078	0,1047	[-]	[-]	46,39
2	0,2207	0,2091	[-]	[-]	105,23
3	0,3434	0,3348	[-]	[-]	196,05
4	0,2130	0,2052	0,2021	[-]	100,39
5	0,1405	0,1415	[-]	[-]	5,245
6	0,0558	0,0537	[-]	[-]	19,49
7	0,0076	0,0097	0,0066	[-]	2,99
8	0,8773	0,05880	[-]	[-]	44,46
9	0,0380	0,0487	0,0370	[-]	15,92
10	0,0805	0,0778	0,0863	[-]	29,19
11	0,1405	0,1298	0,1384	0,1415	15,68

The interesting feature of this outcome was that for the first time we obtained the two best performing filter combination with two different models, the gray body assumption for combi5 and the linear model for combi7. Also this combinations pair gave us the possibility of studying the effect of the adding on of one more filter and understanding the effect on the model. In the following Tables 25 and 26 the results are compare for all the scenarios.

Table 25 - LWIR Combi5 Optimizer Analysis result

LWIR combi 5 errors overview				
Scenario	Absolute ϵ product error [0...1]			T error [K]
1	0,0166	0,0158	800	11,58
2	0,0544	0,0555	200	5,46
3	0,2600	0,2557	800	7,39
4	0,2523	0,2180	200	46,94
5	0,2265	0,2120	800	200
6	0,0719	0,0569	200	15,47
7	0,2543	0,2071	800	200
8	0,3315	0,2841	200	72,07

Table 26 - LWIR Combi7 Optimizer Analysis result

LWIR combi 7 errors overview					
Scenario	Absolute ϵ product error [0...1]			T ref [K]	T error [K]
1	0,0072	0,0095	0,0063	800	5,75
2	0,0651	0,0634	0,0663	200	6,71
3	0,2607	0,2390	0,2264	800	200
4	0,2447	0,2225	0,2104	200	45,42
5	0,2254	0,2227	0,2109	800	200
6	0,0552	0,0517	0,0403	200	12,91
7	0,2549	0,2288	0,2076	800	200
8	0,3178	0,2910	0,2704	200	68,47

Considering the better approximation of the linear model to the ϵ product values we expected to observe a better performance of combi7 compared to combi5, indeed this is true for the majority of scenarios. In the following picture (Fig.73) is shown one example. However how highlighted before this

particular range didn't matched our standards, an example of this is the number of scenarios which temperature error is above the 10K criteria. Once again during the test runs we reached the limit of the system considering scenario 5 and scenario 7 for both combinations the high temperature error is due to the lowest possible RMSE value being found outside the acceptable conditions. Even though these results were not as successful as the one from the MWIR, they confirmed some features observed in the other ranges. In fact also in this case we obtained better performance in summer condition compare to winter and the better performance overall for Pyromark 2500 versus Haynes 230.

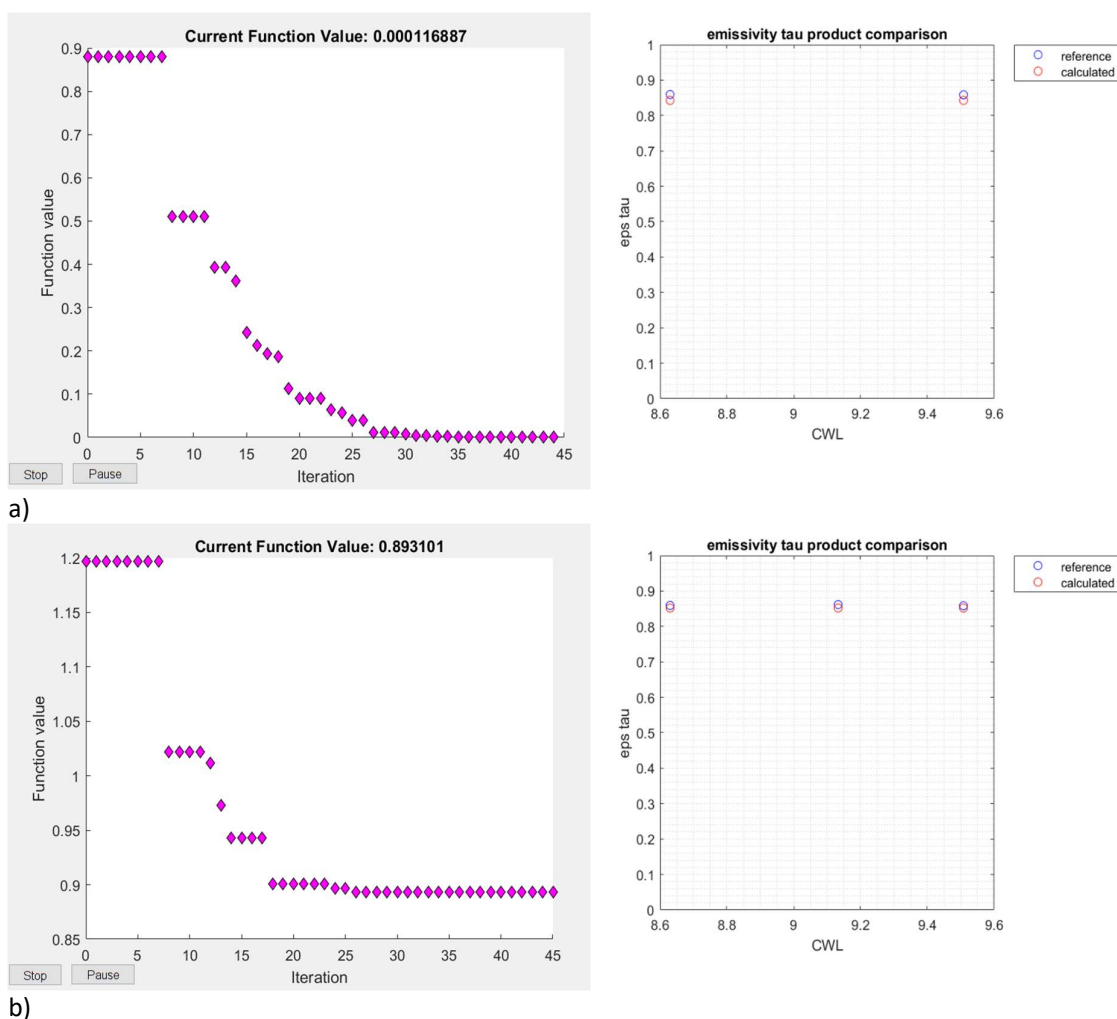


Figure 73 - RMSE final value and $\epsilon\tau$ product comparison for two different filter combinations using two different methods. Both tested for the same materials as Pyromark 2500 in the same scenario1. CWL is expressed in μm . The division of graphs is as follow: a) combi5 ; RMSE: $1,1\text{e-}04$; Absolute temperature error 11,58K; $\epsilon\tau$ error: 0,0166 and 0,0158. b) combi7 , RMSE: 0,893; Absolute temperature error 5,75K; $\epsilon\tau$ error: 0,0072 0,0095 and 0,0063.

The acknowledgement of not ideal results is also a part of long process that science needs to valuated and improving new technologies, however even if in some cases the result were far from ideal we set the first step in this new methodology. That said there will be a discuss in the possible use of this specific method for further applications.

5. Conclusion

Outlook

The main achievement of this work was the successful development of a spectrally resolved radiometric simulation model to test different infrared camera configurations. This model works in any spectral range (SWIR, MWIR, LWIR), covers different cases (atmosphere, coating, filter, etc.) and can be extended to include further detectors, filters, materials and atmospheric conditions.

We were able to test multiple filters combinations and accordingly the range window for a IR measurement system, which will be used to detect both emissivity and temperature of a tube for solar power tower applications. In the last chapter it was discussed in deep the analysis done throughout the three different ranges SWIR, MWIR and LWIR. In the following Table 27 the final conclusions are summarized, the points highlighted are divided into two main sequences with the first one about the response of the model and the second one about the environment aspects.

Table 27 - Final Overview

	SWIR	MWIR	LWIR
<i>Model used</i>	gray body assumption	gray body, linear and quadratic	gray body, linear and quadratic
<i>N° of parameters</i>	2	2,3,4	2,3,4
<i>Calibration</i>	very fast->low filters number	fast->low filters number	slow->high filters number
<i>Optimizer speed</i>	seconds	around a minute	several minutes
<i>Stability</i>	highly stable	mostly stable*	not really stable
ENVIROMENT ASPECTS			
<i>Temperature [°C]</i>	T>300	T>100	T>0
<i>Atmospheric influence</i>	atm. absorption bands critical, especially H2O	atmospheric windows not critical	atmospheric windows, seasonal effects
<i>Solar blindness</i>	under specific atm. conditions	yes	nearly solar blind

There are few major takeaways from this study. The first two are the model stability range and the fast response in the SWIR and MWIR range, this is clear if we take a closer look at the optimizer speed (computational time) in Table 27. Another point is the validation of the analysis of multispectral configurations, confirming literature results [19] [49]. Indeed this was the first attempt present in literature of developing a software of this kind. Thanks to this work it is now possible to amplify the test to an even higher number of different permutations and scenarios. For instance future work will be focused on the development of a prototype ratio imager in the SWIR range, relying on water atmospheric absorption bands (1.4 and 1.9 μm).

References

- [1] British Petroleum BP, «Statistical Review of World Energy,» BP p.l.c., London, 2020.
- [2] M. Cann et al., Environmental Chemistry, W.H.Freeman & Co Ltd, 2006, pp. 153-155.
- [3] H. Shaftel, «climate.nasa.gov/causes/,» April 2021. [Online].
- [4] UN, «unfccc.int/process-and-meetings/the-paris-agreement/,» United Nations Framework Convention on Climate Change, 2021. [Online].
- [5] L. Fæste et al., «bcg.com/publications/2020/how-china-can-achieve-carbon-neutrality-by-2060,» Boston Consulting Group, 12 2020. [Online].
- [6] D. Chandler, «news.mit.edu/2011/energy-scale-part3,» MIT News Office, 26 October 2011. [Online].
- [7] R. Ohl, «Light-Sensitive Electric Device». US Brevetto US2402662A, 27 05 1941.
- [8] Images SI Inc., «imagesco.com/articles/photovoltaic/photovoltaic-pg4.html,» 2007- 2021. [Online].
- [9] IEA, «solarpaces.org/csp-tech-explainers,» 2020. [Online].
- [10] Solargis, «solargis.com,» 2021. [Online].
- [11] P. Breeze, Solar Power Generation, Elsevier, 2016.
- [12] DLR, «dlr.de/sf,» Deutsches Zentrum für Luft- und Raumfahrt e. V., 2021. [Online].
- [13] CSP Services, «cspservices.de,» CSP Services GmbH, 2021. [Online].
- [14] BrightSource Energy Inc, «brightsourceenergy.com,» 2015. [Online].
- [15] M. Vollmer et al., Infrared Thermal Imaging, Weinheim, Germany: WILEY-VCH VerlagGmbH&Co, 2018.
- [16] Lumenistics LLC, «lumenistics.com,» 2020. [Online].
- [17] P. Evans et al., Guidelines for the Management of Naturally Occurring Radioactive Material (NORM) in the Oil and Gas Industry, SPE International Conference and Exhibition on Health, Safety, Security, Environment, and Social Responsibility, 2016.
- [18] J. Crepeau, A Brief History of the T4 Radiation Law, vol. 1, San Francisco: ASME 2009 Heat Transfer Summer Conference, 2009.

- [19] L. Savino, «Free emissivity temperature investigations by dual color applied physics methodology in the mid- and long-infrared ranges,» *International Journal of Thermal Sciences*, vol. 117, pp. 328-341, 2017.
- [20] F. Di Carolot et al., «Standard thermography vs free emissivity dual color novel CIRA physics technique in the near-mid IR ranges: Studies for different emissivity class materials from low to high temperatures typical of aerospace re-entry,» *International Journal of Thermal Sciences*, vol. 147, n. 106123, 2020.
- [21] R.D. Hudson et al., *Infrared Detectors*, John Wiley & Sons, Inc., 1975.
- [22] C. Van Hoof et al., «PolySiGe uncooled microbolometers for thermal IR detection,» in *Handbook of Infra-red Detection Technologies*, Elsevier, 2002, pp. 449-479.
- [23] M. Moreno, «Microbolometers fabricated with surface micro-machining with a-Si-Ge:H thermosensing films,» *International Journal of High Speed Electronics and Systems*, vol. 18, pp. 1045 - 1054, 2008.
- [24] Vision Systems Design,, «vision-systems.com/cameras-accessories/article/16736873/choosing-a-camera-for-infrared-imaging,» 2021 Endeavor Business Media LLC., 2021. [Online].
- [25] D. Maione, «Microbolometer with a multi-aperture polymer thin-film array for neural-network-based target identification,» *Applied Optics*, vol. 58, pp. pp. 7285-7297, 2019.
- [26] The Board of Regents of the University of Wisconsin System, «ssec.wisc.edu,» University of Wisconsin, 2021. [Online].
- [27] MathWorks Inc., «mathworks.com/help/matlab,» 1994-2021. [Online].
- [28] The National Renewable Energy Laboratory, «nrel.gov/,» U.S. Department of Energy, 2021. [Online].
- [29] Spectral Sciences Inc., «spectral.com,» 2020. [Online].
- [30] N. Cox, *Allen's Astrophysical Quantities*, Springer, 2002.
- [31] Rochester Institute of Technology, «rit.edu,» 2021. [Online].
- [32] National Aeronautics and Space Administration, «nasa.gov/mission_pages/sunearth/science/atmosphere-layers,» 2017. [Online].
- [33] GATS, «spectralcalc.com,» 2020. [Online].
- [34] PROMES, «promes.cnrs.fr,» 2020. [Online].
- [35] OMT Solutions BV, «omtsolutions.com,» 2021. [Online].

- [36] S. Caron et al., «Forty shades of black: A benchmark of high temperature sprayable black coatings applied on Haynes 230,» *AIP Conference Proceedings*, vol. 2303, 2020.
- [37] Haynes International, «haynesintl.com,» 2020. [Online].
- [38] LA-CO Industries Inc, «laco.imagerelay.com,» 2020. [Online].
- [39] CIEMAT, «ciemat.es,» 2021. [Online].
- [40] SWIR Vision Systems, «swirvisionsystems.com,» 2021. [Online].
- [41] FLIR® Systems Inc, «flir.com,» 2020. [Online].
- [42] C. Livache et al., «A colloidal quantum dot infrared photodetector and its use for intraband detection,» *Nat Commun*, vol. 10, n. 2125, 2019.
- [43] © Teledyne Judson, «teledynejudson.com/prods/Pages/Photoconductive-Mercury-Cadmium-Telluride-Detectors,» 2020. [Online].
- [44] Spectrogon, «spectrogon.com,» 2020. [Online].
- [45] A. Rohatgi, «automeris.io/WebPlotDigitizer,» WebPlotDigitizer, November 2020. [Online].
- [46] International Organization for Standardization ISO®, «iso.org,» [Online].
- [47] D. Hernandez, «Analysis and Experimental Results of Solar-Blind Temperature Measurements in Solar Furnaces,» *Journal of Solar Energy Engineering*, vol. 126, pp. 645-653, 2004.
- [48] A. Daniels, *Field Guide to Infrared Systems*, SPIE Press Book, 2006.
- [49] J. C. Krapez, «Measurements without contact in heat transfer: multiwavelength radiation thermometry. Principle, implementation and pitfalls,» *Thermal Measurements and Inverse Techniques*, vol. Conference Paper, 2019.